

AD-A265 627



①

**Progress Report:**

**Role of Microstructure on Fatigue  
Durability of Aluminum Aircraft Alloys**

**ONR Contract No. F33615-92-C-5915**

**Project Team:**

**J. R. Brockenbrough, R. J. Bucci, A. J. Hinkle  
J. Liu, P. E. Magnusen, and S. M. Miyasato**

**Alcoa Laboratories  
100 Technical Drive  
Alcoa Center, PA 15069-0001**

**DTIC  
ELECTE  
JUN 09 1993  
S B D**

**1993 April 15**

**DISTRIBUTION STATEMENT A  
Approved for public release  
Distribution Unlimited**

93

002

**93-12790**



Table of Contents	Page
1. Executive Summary.....	1
1.1 The Problem.....	3
1.2 Program Objective.....	5
1.3 Approach.....	5
2. Alloy 7050 Plate.....	9
2.1 Background.....	9
2.2 Materials.....	12
2.3 7050 Fatigue Testing.....	13
2.4 Fractography.....	15
2.5 Effect of Hole Quality.....	19
2.6 Microstructural Characterization.....	20
2.7 Quantitative Optical Metallography.....	22
2.8 Particle Size Distribution.....	24
2.9 Quantitative SEM Metallography.....	24
2.10 Optical vs. SEM Characterization.....	25
2.11 Effect of Volume Fraction.....	26
2.12 Effect of High Deformation.....	27
2.13 Future Characterization.....	28
3. Alloy 8090 Plate.....	29
3.1 Background.....	29
3.2 Materials.....	29
3.3 Microstructural Characterization.....	30
3.4 Mechanical Properties.....	32
3.5 8090 Fatigue Testing.....	34
3.6 Fractography.....	35
3.7 Future Work.....	36
4. Microstructural Based Fatigue Modeling.....	37
4.1 Background.....	37
4.2 Growth Modeling.....	37
4.3 Initiation Modeling.....	40
4.4 Application of Models.....	41
4.5 Summary of Modeling Work.....	42
4.6 Future Work.....	43
5. Summary.....	44
6. Acknowledgements.....	45
7. References.....	46
8. Tables.....	50
9. Figures.....	69

# Role of Microstructure on Fatigue Durability of Aluminum Aircraft Alloys

ONR Contract No. F33615-92-C-5915

## 1. Executive Summary

The goal of this program is to affect change in metallic aircraft life assessment methodology through quantitative understanding of how material microstructure impacts fatigue durability performance. Various studies have shown that most metal cracking problems encountered in service involve fatigue. Further studies have shown that metallurgical discontinuities and/or manufacturing imperfections often tend to exacerbate such problems by causing cracks to occur sooner than expected. This program concentrates on the initiation and early growth stage of fatigue cracks where the majority of structural life is spent. The program has two general objectives: (1) quantifying effect of aluminum alloy microstructure on early stage fatigue damage evolution and growth, and (2) establishing an analytical framework to quantify structural component life benefits attainable through modification of intrinsic material microstructure. The modeling approach taken couples quantitative characterizations of representative material microstructures with concepts of probabilistic fracture mechanics.

Historical fatigue data from Alcoa commercially produced 7050-T7451 plate materials of varying pedigrees is being used to establish a foundation for the subsequent analytical developments. Alloy 7050 is widely used in modern Navy aircraft because of its good balance of strength, toughness and corrosion resisting properties. Additional experimental derivatives of alloy 7050, along with microstructural variants of Al-Li alloy 8090 plate, have also been fabricated and are being examined to broaden the study to include a range of microstructural features which could potentially impact fatigue durability. The technical approach taken in this work is to first quantify the population of crack initiating microstructural features (the extreme value distribution) either analytically or via post test examination, and second to establish fracture mechanics based protocols enabling correlation of these features with coupon fatigue lifetime distributions. The third step will be to establish methods of scaling the distribution of material microstructural features from random plane microstructural characterization to predict the extreme value distribution of microstructural features (the weak links) causing failure. The final and ultimate goal is to develop modeling capabilities that enable probabilistic component life assessments to be made from the distribution statistics obtained by microstructure characterization. This

For	
SAI	<input checked="checked" type="checkbox"/>
ed	<input type="checkbox"/>
tion	<input type="checkbox"/>
per letter	
tion/	
ility Codes	
Dist	Avail and/or Special
A-1	

modeling approach would offer a simpler alternative to expensive fatigue test programs involving large numbers of structural element tests. It would also provide a way to interactively adapt life-cycle analyses into design and problem solving processes.

The current program status is that historical Alcoa fatigue data on alloy 7050 has been assimilated and reviewed. Random cross-sections and specimen fractures have now been obtained and analyzed for the 7050 alloy variants. Models have been synthesized and are being evaluated against the available data. The 8090 modeling work is scheduled to follow that provided by the 7050 experience. To date, two of the three proposed 8090 variants have been fabricated, and the material characterization is underway.

The microstructural variants of alloys 7050 and 8090 in concert with the models in development provide an opportunity to study how changes in microstructure affect lifetimes of structural components. The examination of failed specimens from the variations of the materials employed has identified a hierarchy of microstructural features that are important. In smooth and open hole coupon fatigue tests of the 7050 alloy variants, pores, particles, and grain structure were the features found to exert greatest influence on fatigue performance, generally in that order. However, it was shown that relative magnitude (and even order) of importance within the metallurgical feature hierarchy can shift as conditions of the test (e.g., notch stress concentration and applied loadings) change. Analytical models incorporating microstructural information have been used to explain these effects, and life predictions incorporating these concepts have been shown to correlate well with fatigue results from both smooth and open hole test specimens. The models considered employ fracture mechanics concepts so they can be readily extended to design practice. Existing probabilistic models for the crack growth portion of total life are being used, and an initiation model is being adapted to the predictive scheme. With these models in place a variety of fatigue evaluation scenarios can then be considered.

A vision has been established for exploiting results of this program as a building step towards a material's oriented approach to durability design. Once the microstructural features affecting fatigue have been identified, it follows that life improvement and consistency of performance should be achievable through optimization of material microstructure. A key goal within this program is to illustrate how improved materials should be characterized for use. Potential examples are being developed to show how the analytical concepts and data base being established might be advantageously applied to save weight, extend life, and reduce operator costs. Moreover, though central focus of the work is on intrinsic microstructural inhomogeneities, the quantification of other defect

populations (e.g., corrosion pits, manufacturing nicks and dings) and their effects could also be embraced by the philosophy of the approach under investigation. This combination would be valuable for use in design conceptualizations, setting limits of manufacturing quality inspection, and making risk decisions applicable to the aging fleet.

### 1.1 The Problem

Weight and life cycle costs have always been major considerations in design and operation of aircraft. More recently, because of declining defense budgets, there is strong incentive to keep aging fleets flying well into the next century. For many airplanes within the current inventory, this means an additional 20 to 50 year service extension over that projected at the time of procurement. Unfortunately, these aircraft were not designed for this extended lifetime, and some have been built with materials inferior to those available today. To achieve the new lifetime goals most older airplanes will require some modification to ensure continued safety and economic operation during their extended service. Also, modernization efforts will continue to add weight to existing aircraft systems in the form of more sophisticated weaponry and avionics. Consequently, there is ample incentive for durable, fatigue resistant, materials that can be used to save weight (raise operating stresses) and/or extend life of metallic airframe parts. For reasons of affordability and supportability, a more durable material which can serve as a direct replacement for its incumbent is highly desirable.

Efficient design and operation of metallic airframes requires analytical tools to evaluate conditions leading to formation and growth of fatigue cracks. Damage tolerance procedures employed to analyze growth of large, inspectable cracks are mature, having their foundation in fracture mechanics theory. In contrast, current practices employed in durability-based evaluations (longevity without appreciable cracking) are largely empirical.

Given time and cyclic loadings of sufficient magnitude, all metallic materials develop crack-like flaws. If allowed to grow uncontrolled, these cracks will eventually affect airframe integrity and operating costs. Generally, the evolution of these flaws is accelerated when microscale inhomogeneities, such as porosity or second phase constituent particles are present to facilitate fatigue initiation. It follows, therefore, that life and consistency of performance should be achievable through metallurgical controls that reduce both the number and severity of potentially harmful material discontinuities. This is particularly true

of thick part applications (e.g., bulkheads, lugs, spars, etc.) where the parent metal fabricating constraints (e.g., large ingots, solidification and quenching rates, rolling practices) limit the amount of mechanical work imparted to heal porosity and/or to break-up remnants of the original cast microstructure.

State-of-the-art material selection and procurement practices are not well structured to differentiate product initial fatigue quality (e.g., pores, particles, scratches or other microscale discontinuities that exacerbate cracking problems). This results in lost opportunities for performance and operator cost saving enhancements at affordable costs (e.g., by direct material replacement or tighter manufacturing controls). In most cases the harmful discontinuities in question are too small to be detected reliably by conventional NDE, and standard property tests used in specifications are insensitive to initial fatigue quality. Moreover, quantification of the durability enhancing possibilities through optimization of microstructure is made difficult by the statistical nature of fatigue and the empirical approaches taken by designers.

The USAF has developed a structural durability methodology to deal with effects of initial quality on airframe integrity [1]. The approach characterizes the initial fatigue quality of a material/component and uses probabilistic fracture mechanics to predict the statistics of fatigue cracking originating from inherent defect populations. Despite promise of the methodology, the tools are not widely exploited by industry. This is because little data exists for the inherent material/component fatigue quality, and protocols for generating such information are not well established. Consequently, airframe designers have insufficient confidence to justify the investment of undertaking this new, albeit promising, approach.

In the Air Force protocol, the representation of the material initial fatigue quality combines the effects of both manufacturing and material microstructure. However, microstructure is not directly incorporated into the present day tools. This program is aimed at producing basic understanding and data to incorporate microstructure into the existing framework, and to increase confidence in the methodology, which will eventually lead to broader utilization of the tools. Additionally, exploitation of fatigue improved materials would be facilitated by availability of such a framework capable of connecting microstructure to component performance. Accomplishing these steps would go a long way toward defining the engineering protocols and initial fatigue quality data base needed for technology insertion.

## 1.2 Program Objective

The goal of this program is to provide understanding, representative data and an analytical framework to show that significant fatigue durability improvement is possible through modifications to microstructure. The effort includes establishing data and fracture mechanics based test/evaluation protocols to: (1) link microstructure with fatigue damage evolution and crack growth, and (2) quantify/predict fatigue durability improvements attainable through optimizations of microstructure.

Though the main focus of the work is on developing an analytical capability to study impact of intrinsic microstructural inhomogeneities on fatigue longevity, other extrinsic discontinuity populations (e.g., corrosion pits, scratches, tool marks) and their effects could also be analyzed under the philosophy of the approach.

## 1.3 Approach

The program work scope is built around the following premises:

- Fatigue sensitivity to microstructure is greatest when the damage (cracking) size is on the scale of the governing microstructural features. Early stage cracking (path and propagation rate) is strongly microstructure dependent, but as cracks grow beyond the scale of microstructure, propagation resistance is controlled more so by near-tip plasticity and crack wake (closure) effects. Since the majority of useful fatigue life is spent in propagating to small crack sizes, understanding the mechanisms and statistical nature of microstructure involvement in early stage damage evolution is key to optimization of materials for fatigue durability.
- The durability performance criterion of greatest practical interest to this study is fatigue crack initiation and growth to an inspectable size which may require corrective action. In metallic airframes a 0.05-in flaw represents a typical lower limit for reliable crack detection.
- Quantitative linkages of the following microstructural features to fatigue durability performance are being sought: pores, particles, grain structure, crystallographic texture, slip planarity and precipitate structure. Of these, the first three items have received the greatest attention to date. In addressing the role of these features, a goal is to establish the order of importance relative to fatigue longevity. For example, the classical mechanism for

fatigue crack formation and early stage growth is associated with crystallographic slip [2]. This mechanism, however, can be circumvented by initiation at intrinsic material discontinuities such as pores and particles, and is controlled by their size, frequency, and spatial distribution relative to the specimen configuration and loading details.

- The approach being taken in this investigation considers probabilistic fracture mechanics concepts to quantify fatigue damage accumulation originating from or affected by populations of inherent microstructural features (discontinuities). Under this approach, fatigue durability improvement can be quantified under either of the two performance scenarios depicted in Figures 1a and 2a. The first of these quantifies improvement as life distribution to fixed flaw size, while the second representation quantifies improvement as flaw size exceedance after fixed lifetime. Examples of such quantification are shown in Figures 1b and 2b using data obtained from Air Force fatigue tests on two of the 7050 plate microstructural variants [3].
- The schematic illustration of Figure 3 shows three fatigue durability improvement scenarios that are potentially attainable through modification of material microstructure. The first two scenarios, "reduce initial defects" and "reduce crack growth variability", show improvement achieved through quality controls on metal manufacturing processes. The third approach, "increase crack growth resistance", may require alloy modification. In Figure 3 the economic limit represents a flaw size beyond which remedial action will be necessary. The range of microstructure features to be addressed by this program accommodates examination of all three scenarios, however, the first scenario, "reduce initial defects," will serve as the central focus.
- The program objectives require that materials of varying pedigrees (different inhomogeneity populations) be available. One of these materials represents a lowest common denominator that current specifications allow. Other material variants represent improved fatigue quality products. For this purpose the program is relying on extensive Alcoa 7050-T7451 alloy experience. Alloy 7050 was developed specifically for aircraft thick section applications (e.g., bulkheads, lugs, wing spars) requiring good balance of strength, toughness and corrosion resisting properties. Historical Alcoa fatigue test data and analysis have already shown dramatic S-N fatigue improvements through tightening of manufacturing processes to control distributions of pores and particles [4-11]. Test results and failed specimens from 7050 plate materials of varying pedigrees are being made available (at no cost to the Navy) to benchmark performance improvement potential. The Alcoa 7050 results supplement the present program by serving as a foundation for



development of analytical protocols. Microstructural characterization along random plane sections of the materials allows for statistical correlation with failure causing features (the weak links).

- The aforementioned Alcoa 7050 plate materials are best suited for study of pore/particle effects. Addition of an aluminum-lithium alloy to the program provides opportunity for expanding the range of microstructure feature variants through control of thermal processes. This is advantageous because more conventional 2xxx or 7xxx aluminum alloys would require multiple compositions (greater expense) to cover the range of microstructural variants possible within the single Al-Li alloy composition. An Al-Li alloy composition similar to that of alloy 8090 is being used. The 5-8% density saving afforded by the Al-Li alloy makes it an attractive addition to the program.
- Durability design methodologies which used the concept of an equivalent flaw size (EIFS) population to quantify initial fatigue quality have been developed. This enables evaluation of structural fatigue performance in probabilistic terms (e.g., Figures 1 and 2). Analytical procedures have been developed to obtain the EIFS population from coupon specimen data [6]. These procedures normally involve back extrapolating crack growth to its origin as shown in Figure 4. This investigation provides opportunity to validate results of these calculations with actual flaw population measurements revealed by post-test fractography. The goal is to establish a protocol for defining an intrinsic material characteristic (e.g., EIFS population) from coupon specimens, which in turn can be input into a probabilistic fracture mechanics scenario to predict consequences on structural performance [12]. An envisioned engineering framework for this computational strategy is shown schematically in Figure 5.
- The statistics of fracture data has been studied for many years [13] with much of the effort devoted to study of extreme value distributions. The idea is that materials contain weakening flaws, and though there is a population of these flaws the failure seeks out the dominant flaw as the weakest link. That is, the total population of flaws is not as important as the distribution of harmful (largest?) flaws, the extreme values. A goal of this study is to explore whether the extreme intrinsic material flaw (or equivalent flaw) population can be defined from random metallographic cross sections. The rationale is to attempt to extract information from metallographic images that can be represented in the same functional form as information extracted from coupon specimen tests. A schematic representation of this logic is shown in Figure 6. The connection of the computer and microscope makes this analysis feasible. Input obtained from images can be digitized and subjected to tessellations

and finite element calculations to quantify the localized areas of high strain concentration [14]. If successful this capability will accommodate replacement of large numbers of fatigue tests by representative metallographic characterization. In this way building of the initial fatigue quality data base could be made more cost effective to facilitate broader implementation of the probabilistic fracture mechanics durability design tools.

- The expected outcome of this investigation will be insight into material's fatigue enhancement through microstructural control, coupled with models and procedural guidance for exploitation of improved materials within probabilistic fracture mechanics based durability design rationale.

## 2. Alloy 7050 Plate

### 2.1 Background

In recent years much attention has been devoted by Alcoa to examining the fatigue performance of aluminum alloy 7050 thick plate, and this program relies heavily on that experience. Alloy 7050 was developed specifically for thick aerospace applications which require an excellent combination of strength, damage tolerance, and corrosion resisting properties. The application of 7050 in thick structure (e.g. bulkheads, lugs, wing spars) is often controlled by fatigue requirements, and these requirements can control the size of the part and thus affect airframe weight and performance. As a result, improvements in the fatigue performance of the material may transition to weight savings potential in applications which are limited by the fatigue performance.

It is generally recognized that thick plate is inferior to thin plate in resistance to fatigue damage initiation during service. In thick plate, remnants of the original cast structure persist through to the final product where deformation during rolling is insufficient to effectively break-up the cast structure and heal microporosity which is present in the ingot. An increase in fatigue performance with increased rolling reduction has been observed for 7050 of varying thickness, and that data are shown in Figure 7 [4]. The improved fatigue performance with increasing rolling is attributed to reduction in the size and volume fraction of microporosity remaining from the original cast ingot. This observed behavior prompted much effort aimed at increasing the fatigue performance of thick product to levels observed for thinner material.

Quality improvement efforts at Alcoa on 7050 resulted in reductions in the population of microporosity in plate between 4 and 6 inches thick [4]. While these improvements led to modest increases in short transverse strength, toughness and ductility, rather dramatic increases in smooth axial stress fatigue lifetimes were realized. Fractographic analysis of the smooth specimen failures showed that the lifetime improvement in fatigue was due to a reduction in the size of microporosity which initiated the failure. A good correlation of fatigue lifetime with the size of crack-initiating micropores was observed. Subsequent efforts focused on evaluating how the material improvements which resulted in increases in smooth fatigue coupon lifetimes affected structural performance and how the performance benefit may be captured in design.

An analytical study was performed using probabilistic fracture mechanics analysis developed by the Air Force to investigate the effect that the material quality improvement had on durability performance of aircraft structures [5]. This analysis makes probabilistic projections of component cracks reaching a particular size after a specified length of service. The measured micropore distributions which initiated failure in the smooth coupon tests were input into the analysis. A probabilistic crack growth analysis was performed for the loading condition of a fighter aircraft lower wing. The calculations showed that improved material quality results in substantial increase in structural performance as measured by reduction in the incidences of cracking. As a means of simplifying the process of measuring the sizes of microporosity on fatigue failure surfaces by labor intensive post-test fractography, a fracture mechanics analysis was used to convert the smooth specimen lifetimes to an equivalent initial flaw size (EIFS) distribution [6]. Using fracture mechanics, the EIFS which was back-extrapolated from smooth specimen lifetime data agreed well with the distribution of microporosity measured on the failure surfaces. The back-extrapolated EIFS distribution was used as input into the probabilistic crack growth analysis to assess structural performance. The results obtained using the EIFS distribution as input agreed well with the analysis based on the actual measured micropore size distribution which showed structural performance improvement with metal quality improvement. This methodology now enables data from a simple smooth coupon fatigue test to be analytically converted into structural performance data to quantify advantages of improved metal quality for long term fatigue durability.

Despite the analytical verification of the benefit of improved material quality on structural durability, it remained to be demonstrated whether the lifetime improvement would be realized in actual structure which possess geometric stress concentrations and possibly machining defects which may limit structural lifetime. An experimental investigation was conducted which examined the notched fatigue performance of low and high porosity material using specimens containing open holes subjected to constant amplitude loading [7]. Longer lifetimes were observed for the low porosity material. Post mortem failure analysis showed that the fatigue failures initiated from the microporosity and not from machining flaws, even though no special precautions were taken during specimen machining. This demonstrated that improved material quality should lead to improved structural performance in the presence of engineering detail. Subsequent open hole fatigue testing has been performed on two pedigrees of 7050 thick plate containing different microporosity levels, and two pedigrees of thinner plate of an experimental 7XXX alloy containing different constituent particle levels [8]. In both cases it was seen that

improvements in material quality through reductions in the intrinsic microdefect populations resulted in increases in the open hole specimen fatigue lifetime. Procedures have since been developed to establish improved fatigue strength allowables resulting from the increase in lifetime due to metal quality improvement [11]. Thus, improvement in metal quality could lead to improved structural durability, or if captured at the design stage could lead to weight reductions in fatigue limited components.

Despite the previous efforts, it remained to be demonstrated that material quality improvements would yield performance benefit in more complex structural detail under loading conditions representative of actual aircraft service. A cooperative test program was initiated between the Air Force and Alcoa aimed at investigating the effect of material quality increase on the fatigue performance of increasingly complex structural detail under flight spectrum loading conditions [9]. Spectrum fatigue testing was performed on two pedigrees of 7050 alloy thick plate which contain different levels of microporosity, using specimens containing open holes, specimens with filled fastener holes, multi-holed panels and assembled double lap joint specimens. The results clearly showed performance advantage of the new quality plate under flight simulated loading and in more complex structure.

The previous work has clearly demonstrated advantage of metal quality improvement on fatigue performance and it's potential benefit in structural airframe applications. Despite the apparent advantage that improvement in intrinsic metal quality offers to airframe longevity and/or performance, the tools to exploit this advantage remain under utilized. As stated previously, the objectives of this program are to: (1) link microstructure with fatigue damage evolution and crack growth, and (2) quantify/predict fatigue durability improvements attainable through optimizations of microstructure. The considerable historical fatigue test data and analysis that have been generated for alloy 7050 provide an excellent opportunity to pursue these objectives. Material with varying intrinsic inhomogeneity populations are made available to this program to quantify their effect on fatigue performance and to provide benchmark data to establish predictive protocols which incorporate microstructure.

## 2.2 Materials

Five variants of 7050 plate were selected to provide a range of microstructures to quantify the effects of intrinsic microstructural features on fatigue durability. The first material, designated "old" quality material, was produced using Alcoa production practices typical of those used in 1984. The material is characterized by extensive amounts of centerline microporosity. Despite the centerline microporosity, this material still meets all existing mechanical property specifications for thick 7050 plate. Current quality production material, designated "new" quality material, is also used which is characterized by reduced levels of centerline microporosity compared to the old quality material. The new quality material represents the current benchmark for commercially available material. The processing methods used in the production of the new quality material are a result of a statistical quality control effort to improve 7050 alloy thick plate [4]. Material taken from two plant scale production lots of each quality level provide the material for this program. Both materials are 5.7 in. thick 7050-T7451 plate. Static mechanical property characterization of the two 7050 plate pedigrees showed no significant differences in properties other than an increase in short transverse elongation for the new quality material [6], and both materials meet the AMS material specification minimums. The fact that both materials met the property requirements of the AMS specification underscores the limitation of existing specifications in that they do not differentiate intrinsic metal quality.

The next material variant of alloy 7050 plate was specially processed to further reduce the amount of centerline microporosity. The process used to produce the material is currently not used for commercial production and involves process steps which add to current production costs. The production methods were developed separately under Alcoa funding and are considered Alcoa proprietary. For this contract, material that was produced using these processing methods was obtained at no charge to the ONR for the purpose of providing a microstructure with microporosity levels lower than the current benchmark new quality plate. This material is 6 in. thick and is denoted "low porosity" plate.

The fourth material variant was selected to have minimal microporosity and a significantly smaller constituent particle distribution than either of the previous materials, yet maintain a thick product grain structure. For this purpose, material was selected from the quarter thickness plane (T/4) of 6 in. thick plate which was produced from ingot that had controlled composition which limited the formation of coarse constituent particles. Constituent particles in 7050 plate are typically of the types  $Al_7Cu_2Fe$  and  $Mg_2Si$ . These form during ingot solidification and are insoluble, so they remain in the material through processing to

the final product. The mechanical work of processing may break up the particles which produces stringers of smaller particles. This material is denoted as "low particle" plate.

The final microstructural variant of 7050 plate used in this program was selected to have no microporosity and have a refined constituent particle size distribution and refined grain size compared to standard production thick plate. For these characteristics, thinner plate 1 in. thick was selected. The increased amount of deformation required to produce the thinner plate acts to heal microporosity and break-up coarse constituent particles which are present in the cast ingot.

A summary of the material pedigrees selected for this program and their intrinsic microstructural feature which may affect early stage fatigue damage are listed in Table 1. This range of material microstructures provides a hierarchy of fatigue initiation mechanisms which affect the fatigue durability. The study of these materials will provide a mechanistic understanding of fatigue damage and will lead to predictive strategies incorporating microstructure.

### 2.3 7050 Fatigue Testing

Fatigue testing has been conducted on the five 7050 alloy microstructural variants used in this study. The fatigue tests have been performed for both smooth-round axial stress specimens and flat bar specimens containing open holes. Since some of the data were developed separately under Alcoa funding and tests were performed at different times, some differences exist in the testing that are considered when comparing data for the different microstructures. Additional testing will be performed as deemed necessary to provide compatible data sets for comparison and analysis.

Smooth axial stress fatigue tests were performed for both the old and the new quality plate materials. The tests were done on round bars with a gauge diameter of 0.5 in. Gauge sections were sanded longitudinally to remove circumferential machining marks. Testing was done at a maximum stress of 35 ksi, a stress ratio  $R=0.1$ , cyclic frequency of 10 Hz, in laboratory air. The specimen orientation was long transverse (LT) relative to the parent plate. The specimens were removed from the mid-thickness ( $T/2$ ) plane of the plate where microporosity concentration is the greatest [6]. The lifetimes of the specimens are given in Table 2 and the data are plotted in Figure 8 as a cumulative failure plot where the data are sorted in order of ascending lifetime and ordinate is the percentile ranking of the specimens

relative to the total number of tests. Thus the lifetime corresponding to the 50% point on the ordinate represents the median lifetime where half of the specimens failed prior to that lifetime and half failed at longer lifetimes. The data show that the cumulative distribution of fatigue lifetimes for the new quality material is longer than for the old quality material.

Fatigue tests were also performed for the old and new quality materials using flat specimens containing open holes. Tests were performed at four stress levels for each material pedigree at a stress ratio of  $R=0.1$ , cyclic frequency of 25 Hz, in laboratory air. As with the round specimens the specimen orientation was LT and the specimens were removed from the T/2 plane of the plate. Initial tests were performed on specimens in the as-machined condition and it was found for the new quality plate that the hole edge burrs affected the fatigue lifetime by prematurely initiating fatigue cracks. To eliminate this problem, the holes were de-burred by polishing with diamond compound prior to testing. The polishing was only done on the corners and not in the bore of the hole, and resulted in slight rounding of the corners. The fatigue lifetime data are given in Table 3 and are plotted in Figure 9 as a stress vs. lifetime (S/N) plot. Also plotted for both materials are the 95% confidence limits for the S/N curves. The confidence limits were obtained from a Box-Cox analysis of the data, which enables statistical determination of the mean S/N response and the 95% confidence limits [11]. The data clearly show that at equivalent stresses the new quality material exhibited longer lifetimes than the old quality material. Alternately the improvement in material performance may be expressed as an increase in the stress for a given cyclic lifetime. Data represented in this manner are shown in Table 4, where the stress at a given lifetime is determined from the calculated mean and lower 95% confidence limits. This improvement in stress at a given cyclic lifetime may correspond to an increase in operating stress for a specific part design, and when design is controlled by fatigue, the improvements could enable downsizing to obtain a weight savings. Fatigue strength improvements of the magnitude shown in Table 4 also provides opportunity for lower cost manufacture. For example, typical wing and fuselage structure is sized by strength and rigidity requirements with padded (waffle constructed) areas to handle fatigue loads at connections. The higher fatigue strength capability affords the opportunity to simplify the waffle construction to save cost.

Cumulative smooth fatigue lifetime distributions were obtained for the new quality plate and the low porosity plate tested at a maximum cyclic stress of 40 ksi (The data in Figure 8 are for 35 ksi maximum stress). The stress was increased over the previous tests because the lifetimes of the low porosity plate would be too long to practically test at the lower



stress level. All other testing conditions were the same as the previous tests. The fatigue lifetime data are given in Table 5 and are shown in Figure 10. It can be seen that the low porosity plate shows considerably longer smooth fatigue lifetimes than the new quality plate.

Open hole specimen S/N fatigue results were also obtained for the low porosity plate for comparison to the new and old quality plate open hole S/N curves. The fatigue data are given in Table 6 and the results are plotted in Figure 11 along with the bounds for the old and new quality plate determined from the Box-Cox analysis. The open hole data for the low porosity plate lies within the bounds for the new quality plate. This occurs despite the significant improvement in the smooth specimen fatigue lifetime for the low porosity plate. An investigation into the mechanisms for the observed behavior will be presented later in the fractography section.

A limited amount of fatigue testing has been completed to date on the low particle thick plate. Five open hole specimen fatigue tests have been performed at a maximum net stress of 30 ksi. The data are listed in Table 7 and plotted in Figure 12 along with the confidence limits for the new quality plate. The data reveal that the low particle plate has longer lifetimes than the new quality plate. Additional open hole specimen fatigue tests and smooth specimen fatigue tests will be completed shortly.

The final microstructural variant of 7050, the thin plate, was tested using the same open hole S/N fatigue test conditions as for the other materials. The data given in Table 6 along with the low porosity plate data, and are shown in Figure 13 with the confidence limits for the new quality plate for comparison. The open hole data for the thin plate are considerably longer than the new quality plate. The improvement is so dramatic that additional testing is being performed to verify that the improvement is real and not an anomaly in the test procedures. An analysis of the mechanisms for the improvement are presented in the following section.

## 2.4 Fractography

Fractography of the failed fatigue specimens was performed to identify the microstructural features which affect the fatigue damage process for each of the material microstructural conditions. The fractography was performed using a scanning electron microscope. The smooth fatigue failures for both the old and the new quality thick plate were seen to initiate

at surface or near surface micropores. Typical microporosity at the initiation sites is shown in Figure 14. The difference in the lifetimes of the two materials was found to be due to a difference in the size of the crack initiating micropores. The correlation of fatigue specimen lifetime to size of fatigue initiating micropores, represented by the maximum pore dimension measured from the SEM photographs is shown in Figure 15. The data show that for increasing size of crack initiating micropores there is a decrease in fatigue lifetime. In addition, the new quality plate had smaller fatigue initiating micropores than the old quality plate and hence longer fatigue lifetimes. It is important to point out that the micropores in the new quality plate are smaller than can be reliably inspected for (0.05 in.) but larger than a typically assumed starting flaw size (0.01 in.) for durability analysis.

Fractography of the failed open hole specimens for the old quality plate showed for all cases microporosity at the initiation site for the fatigue failures, which typically were located within the bore of the hole. In some of the failures there were multiple initiation sites where microporosity was observed at the origin of each of the fatigue cracks that were present. The location of the multiple initiation sites varied; they were sometimes observed on opposite sides of the hole, sometimes more than one initiation site was observed on one side of the hole, and occasionally a combination of the two cases was observed. An example of the microporosity observed at the initiation sites in the old quality material is shown in Figure 16.

Observation of the open hole fractures from the new quality thick plate showed that failures originated at microporosity. An initiation site for the new quality plate is shown in Figure 17 which shows a micropore initiated fatigue crack. It is worth pointing out here that prior to establishing the practice of de-burring holes, open hole fatigue tests were performed for both materials without de-burring the holes. The old quality material failed at micropores while all of the new quality material failures started at burrs at the hole corners. The lifetimes of the new quality specimens were longer than the old quality material, but shorter than when the holes were de-burred. This will be discussed in more detail later in the section on hole quality effects.

Fractography of smooth specimen fatigue failures of low porosity plate revealed that failures initiated predominantly at microporosity which was smaller than the crack initiating micropores in either the old or the new quality plate. In several cases there were constituent particles near the microporosity, and in some of specimens only constituent particles were observed at the fractures. Typical smooth fatigue failure origins in the low porosity plate are shown in Figure 18. The fractography of the open hole specimen failures for the low

porosity plate showed that the failures originated from constituent particles, and in most cases the particles were located at the corner of the hole. Figure 19 shows a fatigue crack initiation site to be a constituent particle located at the hole corner. Detailed SEM observation of the initiation site on opposite specimen halves was performed to determine the mechanism of crack initiation from particles. Figure 20 shows the opposite halves revealing that particles are located on each half and that they appear fragmented, indicating either a particle cluster as the initiation point or fracturing of a single particle at the origin.

The transition of failure modes from micropore fatigue origins in smooth specimen fatigue tests to particle origins in open hole specimens for the low porosity plate affects the fatigue performance relative to the benchmark new quality plate. In the smooth specimen tests the low porosity plate showed significantly longer lifetimes than the new quality plate, whereas in the open hole tests the lifetimes of the two materials are similar. The transition to the particle initiated open hole failures in the low porosity plate is most likely related to the size and distribution of pores and particles and the volume of material subjected to the high stress. Since there are many more constituent particles than there are micropores within the material there is a greater probability of having a particle or cluster of particles located at a localized region of high stress. For the open hole specimen geometry, the most detrimental position for crack initiation is the hole corner stress concentration, where  $k_t$  is about 20% higher than in the bore of the hole [15]. The corner effect will be shown later in the modeling portion of this report which will also examine the relative driving force for crack growth from micropores and constituent particles.

To observe the nature of the constituent particle distribution in the bore of the hole of an open hole specimen, low magnification (25X) scanning electron microscopy using the backscattered electron detector was performed. In backscattered mode the Fe-bearing constituent particles appear lighter than the matrix since more electrons are reflected from the higher atomic number elements (Fe vs. Al). Figure 21 shows the constituent particles which are present in the bore of the hole for both the new quality and the low porosity plate materials. In both materials there are significant numbers of Fe-bearing constituent particles present and it is easily seen that there is a high probability of having a particle located in a region of high stress concentration near the corner of the hole which would favor fatigue crack initiation. Figure 22 shows the constituent particles in the bore of the hole at higher magnification. It can be seen that the particles exist as clusters of smaller particles. The fatigue crack initiation site shown previously in Figure 20, where the particle

appeared fragmented, is likely a result of crack initiation from a cluster of finer particles as shown in Figure 22.

There is considerably more microporosity in the new quality material compared to the low porosity material. Thus, for the new quality material there is a higher probability of having a micropore located in the bore of the hole which could act as a site for fatigue crack initiation. The reduced microporosity distribution in the low porosity plate is such that the probability of having a micropore located at the bore of the hole is low, and thus fatigue crack initiate at constituent particles at the hole corner. The observance of micropore initiated failures in both materials in the smooth specimen tests is due to the greater volume of material sampled in the smooth test compared to the open hole test. Because the volume of material which sees the highest stress in the smooth specimen is so much larger than in the open hole test then there is a much higher probability of finding a micropore favorably located for fatigue crack initiation, even for the low porosity plate.

Open hole specimen fatigue failures from the thin plate were examined under the SEM. Some of the fatigue failures were observed to initiate at constituent particles. Figure 23 shows two examples of constituent particles at the origin of the fatigue failures. The size of the constituents is considerably smaller than the constituent particles seen to initiate failure in the low porosity plate. Additionally, the thin plate lifetimes were much longer. It is not yet clear whether the increased lifetime is due merely to the reduction in particle size or a combination of that and the refinement in grain size with larger reductions during rolling.

In addition to the particle initiated failures in the thin plate, cleavage-like fatigue initiation sites were observed with no identifiable microstructural feature at the origin. This was also observed for the low particle plate. Figure 24 shows this type of initiation site observed in both the thin plate and the low particle plate. This appearance is typical of the classic stage I fatigue crack initiation characterized by repeated slip along crystallographic planes leading to the formation of a crack along the persistent slip bands. One feature of this type of fatigue initiation mechanism is the faceted appearance of the initiation site with the crack propagating initially at an angle to the stress axis along planes of high shear stress. This characteristic is evident in the micrographs shown in Figure 24.

Despite the similarity in the failure initiation mechanisms, the thin plate exhibited considerably longer lifetimes than the low particle thick plate. The reason for the difference in the lifetimes is not clear. It is likely that the refined grain structure in the thin plate due to the increased deformation during rolling is a key factor. It is generally known that reduced

grain size results in improvements in resistance to fatigue crack initiation, and the current work seems to indicate an effect of grain size for the crack initiation mechanisms observed. Additional fracture analysis, detailed metallography and modeling will be used to elucidate the reasons for the dramatic fatigue life improvement in the thin plate.

## 2.5 Effect of Hole Quality

In addition to intrinsic microstructural features which affect airframe fatigue durability, an important consideration for structures is initiation from extrinsic sources such as manufacturing imperfections. If severe enough, the influence of manufacturing imperfections on fatigue damage initiation can override increases in durability due to improvements in metal quality. Thus, it is important to understand the relative effects of manufacturing imperfections on durability in order to capitalize on the improvement in metal quality.

Previous open hole fatigue tests on the new quality thick plate were performed using specimens in the as-machined conditions without the hole edge burrs being removed. All of the open hole test data presented here had the holes de-burred with the exception of the old quality plate. The effect of the coarse microporosity in the old quality plate was more severe than hole edge burrs so the specimens did not need to be de-burred. Figure 25 shows the stress versus lifetime plot for the open hole fatigue tests of new quality plate for both the as-machined and the de-burred specimens. At high stresses the lifetimes for the two are similar, but at lower stresses the de-burred specimens exhibit longer lifetimes than the as-machined specimens. Fractography of the as-machined specimens revealed that hole edge burrs initiated the fatigue cracks, and a micrograph showing a hole edge burr is shown in Figure 26.

These data underscore the importance of attention to manufacturing quality as well as material quality to improve structural fatigue durability. The data also indicate that the use of simple procedures to ensure good manufacturing quality provides opportunity to exploit improved metal quality by reducing extrinsic sources of damage initiation. For the five microstructural variants of alloy 7050 plate the key microstructural features affecting fatigue crack initiation have been identified. The features observed for each of the materials are summarized in Table 8. Hole quality can essentially be included in the hierarchy of features which control damage initiation in open hole specimens. Table 8 includes hole quality as a

fatigue damage initiating feature for open hole specimens in the as-machined condition and compares it to the case where the holes are de-burred. The lifetime improvement associated with reductions in microstructural inhomogeneities can be realized for structural applications when manufacturing quality is controlled through simple procedures such as de-burring.

The identification of the key features in each of the microstructural conditions is a key to understanding the process of fatigue crack initiation. The next section deals with characterization of the key variables for each of the materials which will serve as inputs to models to predict material performance.

## 2.6 Microstructural Characterization

As observed previously for some of the 7050 plate microstructures, the constituent particle population controls the fatigue crack initiation behavior. Constituent particle distributions were quantified on four of the five microstructural variants of 7050 using automated image analysis. Constituent particle distributions were not quantified for the old quality plate since the effect of the particles on fatigue is negligible compared to the effect of microporosity which is present in this material.

The constituent particles, typically  $\text{Al}_7\text{Cu}_2\text{Fe}$  and  $\text{Mg}_2\text{Si}$ , form during ingot fabrication. Once these particles form they are stable and cannot be dissolved by thermal practices, and thus persist through to the final product. However, mechanical work does break up the constituent particles: rolling into plate produces long stringers of particles running parallel to the rolling direction, and the larger amounts of deformation to produce thinner plate can result in a smaller constituent particle distribution. Particle sizes may be up to  $100\text{ }\mu\text{m}$  (0.004 in.) in length, and as seen previously the particles are microstructural inhomogeneities from which fatigue cracks may initiate. The characterization of large particles is emphasized since these control the fatigue initiation in the absence of microporosity.

Automated image analysis provides a way of obtaining a statistically meaningful characterization of constituent particles. The distribution of particle sizes and the extreme value distribution is more important than the mean value alone since fatigue damage initiation is controlled by the larger particles. In addition to size distribution, spatial distribution can also be an important parameter. Two materials may have the same particle

size distribution, but the particles may be more clustered in one material. The degree of clustering is also likely to have an effect on the fatigue initiation behavior of 7050 thick plate. The distance between particles is easily obtainable using automated image analysis systems.

Samples of the new quality and the low porosity material were sectioned to examine the longitudinal plane (normal to the LT direction) at the one tenth, quarter and half thickness (T/10, T/4, and T/2) locations. In addition to these materials, the two other variants of 7050 examined were the low particle plate and the thin plate. The low particle plate used compositional control to reduce the volume fraction of constituent particles below that of standard material. Contrasted to the mid-thickness plane of thick plate, thin plate receives higher amounts of deformation during rolling which acts to break up particles. Thus, the comparison of thick and thin plate performance provides an opportunity to examine the effect of mechanical work on particle size distribution and its effect on fatigue.

Automated quantitative optical metallography was performed on as-polished cross sections from the longitudinal plane, normal to the LT direction, for the new quality and low porosity thick plate to characterize the size and spatial distributions of constituent particles. A low magnification was used which maximized the area characterized, and thus improved the chances of encountering the largest particles. However, the lower magnification degraded the spatial resolution so that closely spaced particles were measured as one particle, and the small particles below the resolution limit were not measured. Forty fields, each  $0.77 \text{ mm}^2$ , were analyzed at 100X magnification for a total area of  $31 \text{ mm}^2$  ( $0.048 \text{ in}^2$ ). An average of 6600 particles was characterized per location in the thickness. Particles smaller than  $1.6 \mu\text{m}$  ( $0.062 \times 10^{-3} \text{ in}$ ) in projected length could not be resolved, and thus were not analyzed.

For irregularly shaped particles, the particle size was defined to be the maximum projected particle dimension ('D<sub>MAX</sub>') since this is believed to be the most influential particle dimension relative to material properties. Particle spacing ('FERET X') was measured as the distance between particles parallel to the rolling direction only. While this is not sufficient to uniquely define the spatial distribution of particles in the material, this distance does indicate the relative amount of particle clustering in similar samples. Distances larger than a single view field could not be measured which truncated the upper particle spacings at the length of the view field. This is not considered significant since fatigue initiation will not be affected by large particle spacings but rather by clustering of particles. For simplicity and to save time, this characterization method was selected over more complex

characterization methods. An alternative method that would provide more information would use randomly oriented test lines. The tessellation procedure has also been shown to usefully characterize the degree of particle clustering in low particle volume fraction materials [16] and may be used later to characterize particle clusters if required in the modeling of fatigue initiation.

Quantitative metallography was also done on a similarly designed SEM-based image analysis system. The differentiation of particle types by chemistry on the SEM system was used to separate Fe- and Si-containing constituent particles. This may be necessary if particle type affects fatigue initiation mechanisms. For these analyses, 20 fields were analyzed at 250X magnification, for a total area of 1.2 mm<sup>2</sup> (0.002 in<sup>2</sup>). Particle dimensions as small as 0.4 μm (0.016 x 10<sup>-3</sup> in) were detected.

## 2.7 Quantitative Optical Metallography

Table 9 contains the results of the quantitative optical metallography at various thickness locations in new quality and low porosity plate. The effect of depth within the plate can be seen by comparing particle distributions at the T/10, T/4 and T/2 locations. The particle distribution is expected to vary with plate depth for two reasons. First, solute segregate during casting will result in differences in particle volume fraction, and second, the amount of deformation during rolling varies inversely with plate depth, which can affect the particle size, shape and number density.

In both the new quality and low porosity plate, the area fraction of constituent particles larger than 1.6 μm varied only slightly between T/10, T/4 and T/2 locations, as shown in the bar graphs in Figure 27a. The T/10 location had the largest area fraction of particles while the T/2 location had the smallest. Since the area fraction was calculated by computing the area fraction for each of the forty fields, then averaging those values, another important value is the standard deviation (indicated by arrows in Figure 27a), which indicates the field-to-field microstructural variability. The large standard deviations suggest a non-uniform distribution of particles through the material, even when examining only one location in the thickness; this emphasizes the importance of characterizing sufficient area to overcome the inherent variability in constituent particle population.

The number of particles observed in both materials decreased monotonically with depth in the plate (Figure 27b). Since the number of particles decreased by almost 50% from the



T/10 to T/2 location while the area fraction varied only slightly, the mean particle size increased with plate depth. This is consistent with the slower cooling rate during solidification, as well as the decreased amount of work absorbed during rolling, with increasing depth in the thick plate.

Figure 28 shows particle size distributions for the two materials at the different plate locations on a logarithmic scale; this same information is also included in Table 10. The T/10 location is seen to have almost twice as many small ( $<10\text{ }\mu\text{m}$ ) particles as the T/4 and T/2 locations. However, all three locations showed about the same number of large particles. The histograms in Figure 28 demonstrate the truncation of the particle size distribution due to the resolution limit at this magnification. Since the particle size distribution is cut off at the resolution limit of the image digitizer, the results cannot be fit to a normal distribution in a valid way. Thus, the mean and standard deviation values reported in Table 9 are representative of the particles  $1.6\text{ }\mu\text{m}$  or larger, and are not representative of the actual particle population in the material. This calculated mean particle size is therefore an underestimate of the actual value, since the mean value would decrease with the addition of smaller particles to the distribution. These calculated values can be used to compare materials characterized in this study, but comparisons with data reported elsewhere should be made cautiously.

There was a trend towards decreasing mean particle spacing (feret x distance) in the rolling direction with plate depth (Table 9). 'Particle spacing' encompassed two lengths: an inter-particle spacing of relatively short lengths, and an inter-stringer spacing of relatively large lengths. Histograms of particle spacing (Figure 29 and Table 11) show that the plate location has a strong effect on the high end, inter-stringer spacings. At the T/10 location, a larger number of long spacings were observed compared to the T/2 location which corresponds to the greater deformation near the plate surface during hot rolling. At the smaller particle spacings, there seemed to be less of an effect of plate depth on the inter-particle spacings.

Comparison between the new quality and low porosity plate particle distributions are shown in Figure 29 for the various thickness locations. The particle distributions in the two materials are nearly the same at all thickness locations. Thus, the processing path used to reduce the porosity in the low porosity plate had no significant effect on the constituent particle distribution. Both the new quality and low porosity plate had particle area fractions that were lowest at the T/2 location, number densities that were lowest at the T/2 location, and inter-stringer spacings that were largest at the T/10 location. The effect of low porosity

processing was much less than the effect of plate depth on constituent particle distribution characteristics.

## 2.8 Particle Size Distribution

Microstructural based models for fatigue crack initiation require quantification of the particle size distribution. One way to represent the data is a cumulative probability plot of particle sizes where the number of particles below a given size is normalized by the total number of particles measured. Figure 30 shows the resulting cumulative probability plots of particle sizes in both new quality and low porosity materials at the three different plate depths. At small particle sizes the distributions were not affected by either the thickness location or the type of material. The distributions show divergence at the larger particle sizes with the T/2 locations have a higher percentage of larger particles than the T/10 locations. The lower tail portion of the distributions are not well represented due to the truncation of small particles at the resolution limit of the image analysis system.

The constituent particles were irregular in shape, and thus it was of interest to check whether the actual area of the particles followed the same behavior as the longest projected dimension. Because the image analyzer captured the real cross-sectional area of the particles, it was not necessary to make assumptions about the particle shape. Figure 31 displays the probability plots for the particle area, which follow the same characteristic curve as the longest projected dimension plots in Figure 30. As was found for particle length, the smaller particles showed no effect of either thickness location or the type of material, and the divergence increased with increasing particle size. The distributions for both standard and low porosity material were slightly narrower at the T/10 plate depth than the T/2. Although particle length and area are equally easy to obtain in automated image analysis, length will continue to be used to characterize particles.

## 2.9 Quantitative SEM Metallography

Quantification of the constituent particle distributions using a SEM-based automated image analysis system was used to separate particle types by chemistry. A comparison of the SEM results to the optical microscopy characterization will be provided later. The

characterization of constituent particle distributions using SEM was performed for the new quality plate, low porosity plate, low particle plate, and thin plate materials.

Since the primary insoluble constituents in alloy 7050 are  $\text{Al}_7\text{Cu}_2\text{Fe}$  and  $\text{Mg}_2\text{Si}$ , particles were characterized as either Fe-containing or Si-containing. Table 12 contains the image analysis data from new quality and low porosity plate, at the T/2 location, obtained from SEM images at 250X over a sample area of  $1.2 \text{ mm}^2$ . A relatively small number of particles (around 300) were analyzed in both materials, with more than half of the particles being Si-containing in both plate products.

The histograms in Figure 32 indicate the size distributions for Fe-containing and Si-containing particles. The Si-containing particle distributions are skewed left to the smaller end on the logarithmic plots, while the Fe-containing particles are more more normally distributed. The trends for the Si- and Fe-particle sizes are particularly dramatic for the low porosity plate. Because the Si containing particle distribution is truncated, the mean value reported in Table 12 is an overestimate of the mean of the actual particle distribution. In contrast, the Fe-containing particle distribution does not appear to be significantly truncated since the Fe particles are generally larger in size.

The cumulative probability plots for new quality and low porosity plates (Figure 33) also show the difference in size between types of particles. The thick solid line represents the total constituent particle population. For both materials the distribution of Fe-containing particles lie to the right, indicating larger sizes, and the Si-containing particles lie to the left, indicating smaller sizes. Although Si particles are more numerous, they are smaller and may not play as significant a role as Fe containing particles on fatigue crack initiation.

## 2.10 Optical vs. SEM Characterization

A comparison between the particle measurements made using optical metallography and those performed using SEM is necessary to provide input of the particle distribution characteristics into models of fatigue initiation. Differences in magnification and number of fields measured may account for differences in the quantitative results. The SEM analysis increased magnification from 100X to 250X and reduced the number of fields from 40 to 20, which reduced the area of material characterized by over 12 times. Since both the magnification and the number of fields changed, the effect of optical versus SEM methods

alone could not be deconvoluted. With this caveat, the following are some comments that can be made.

The quantitative metallographic data from both the optical and SEM based characterizations are given in Tables 13. The particle area fraction when measured optically is significantly higher for both standard and low porosity materials, despite the fact that a large number of particles were below the resolution limit when using the lower magnification (over 50% of the particles measured at 250X were below the detection limit at 100X). For example, the area fraction of constituent particles in low porosity material was 0.98% optically and 0.55% using SEM. The resolution limit at the lower magnification may have partially contributed to the higher area fraction, since the matrix area between closely spaced particles may be measured as particle area. Another possible factor is that the limited sampling at 250X was not representative of the total population. Since constituent particles are not uniformly distributed through the material, a large area must be sampled to experimentally characterize the high-end tail of the particle size distribution.

Figure 34 compares the particle size distributions measured using the different techniques. For both new quality and low porosity plate, the SEM gave in lower median particle size. This also stems at least partially from the fact that particles separated by very small distances may be measured separately at the higher magnification but measured together as one large particle at the lower magnification. One consequence is that the particle number density be greater for the higher magnification analysis, which is indeed the case: standard material had 166 particles/mm<sup>2</sup> at 100X and 259 particles/mm<sup>2</sup> at 250X.

### 2.11 Effect of Volume Fraction

Comparisons between new quality and low particle plate provide an understanding of the effect of the constituent particle volume fraction on the particle distribution characteristics. A large reduction in both particle area fraction and particle number density are observed (Table 12). The area fraction in the new quality plate was 0.304%, and that for low particle plate was 0.071%. The number density of particles decreased from 252 particles/mm<sup>2</sup> in the new quality plate to 160 particles/mm<sup>2</sup> in the low particle plate.

Comparison of the particle size histograms for new quality and low particle plate reveals a difference in the particle size distributions (Figures 29(a) and 35(a)). The number of particles in low particle plate drops off dramatically with particle size; very few particles are

larger than  $5.5\text{ }\mu\text{m}$ . This contrasts with the more uniform distribution of particle sizes in new quality plate. It is important to note that there is not only in a smaller area fraction of particles, but also in a smaller mean particle size and a narrower particle size distribution. The narrower distribution should produce an improvement in fatigue crack initiation, which depends on the probability of a large flaw being in a certain area.

In addition to having a higher mean particle size, Fe-containing particles also have a higher standard deviation than Si-containing particles. Because of the higher number density of Si-containing particles, the total particle population closely resembles the population of Si-containing particles.

## 2.12 Effect of High Deformation

Quantification of the particles at T/2 in 1 inch thick plate provided an opportunity to study the effect of higher amounts of deformation on particle distributions. These results complement the study of different plate depths presented earlier. The T/10 location in 6 inch thick plate received more deformation than the T/2 location; however, the 1 inch thick plate has absorbed even larger amounts of deformation and has a different particle size distribution. In the thin plate the area fraction of particles was roughly the same as for both the new quality and low porosity thick plate materials. This similarity in particle area fraction is reasonable since no control was used to limit particle volume fraction as in the low particle plate. However, the number of particles was three times as large for the thin plate as for the thicker materials due to the larger amount of deformation during rolling down to 1 inch thick plate compared to rolling down to 6 inch thick plate. Figure 35(b) graphically shows the high constituent particle number density in the 1 inch thick plate. The increased deformation breaks up the larger particles thus refining the particle size distribution. The mean area of individual particles dropped from  $11\text{ }\mu\text{m}^2$  in new quality plate to  $5.3\text{ }\mu\text{m}^2$  in the thin plate. The particle number density increased from 259 particles/ $\text{mm}^2$  in the new quality plate to 768 particles/ $\text{mm}^2$  in the thin plate.

Figure 12 (b) shows the cumulative distribution of Fe- and Si-containing particles in the thin plate. The Fe-containing particles are larger than the Si-containing particles even after high amounts of deformation. Thus, the Fe-containing particles are either larger than the Si-containing particles in the cast condition and persist that way through processing, or the

Si-containing particles are broken-up early in the processing and are smaller at the plate thicknesses examined here.

The mean particle size was also smaller in the thin plate compared to new quality and low porosity plate. Nonetheless, the variant with the finest particles was the low particle plate. The compositional control appears to be most effective in reducing constituent particle sizes in 7050 plate materials. This should translate to improvements in fatigue durability.

In the thin plate the particles lay in stringers, and it is possible that these clusters of particles affect fatigue crack initiation more dramatically than individual particles. Unfortunately, no measure of the spatial distribution was obtained during the SEM-based image analyses. It is postulated that both the inter-particle and inter-stringer distances increased with the increased amount of deformation, which may also improve fatigue crack initiation resistance. Future work should include measuring the degree of clustering in thin plate.

Curiously, the aspect ratio of the particles did not change with amount of deformation. The mean aspect ratio (minimum particle diameter divided by maximum particle diameter) of all particles in the new quality plate was 0.52, and the mean aspect ratio in the thin plate was 0.53.

### 2.13 Future Characterization

The objective of the metallographic characterization work is to provide input into microstructural based models for fatigue initiation. The models require that the quantification of the microstructure on 2-D random sections be scaled to represent the extreme value distribution of microstructural features controlling fatigue crack initiation. It may be necessary to incorporate the effects of clustering of particles which is currently ignored for simplicity. The differences in the characterization results using optical metallography versus SEM based characterization need to be more fully understood. Finally, the combined effects of microstructural features such as constituent particles and grain structure will need to be sorted out and work done to characterize grain structure differences in materials.

### 3. Alloy 8090 Plate

#### 3.1 Background

Wrought Al-Li alloy 8090 thick plate is a complementary material to 7050, providing an opportunity to evaluate the effects of grain structure, crystallographic texture and slip planarity on fatigue life. Current commercial product has reduced micropore and constituent particle levels, and hence other microstructural features become increasingly important. Features such as grain structure, crystallographic textures and precipitation are easily manipulated through thermomechanical processing in Al-Li alloys. The grain structure can range from fully recrystallized to fully unrecrystallized, and correspondingly, the crystallographic texture can range from high in cube component to high in brass component. Variations in the artificial aging treatments can produce different distributions of precipitates, which control the slip localization in these alloys.

Fatigue crack initiation is known to be sensitive to microstructural features. Typically, cracks initiate at surface flaws such as constituent particles and micropores [17,18]; if the flaws are large enough, then cracks can also initiate in the interior of the part or sample. In most commercial material, there is usually feature that is sufficiently large and high in number density to act as a stress rise. Fatigue crack initiation can also occur by dislocation damage. Persistent slip bands form at the specimen surface, and these act as crack initiation sites. The ability to systematically control the microstructure of Al-Li alloys provide an opportunity to further the understanding of the role of microstructure on fatigue and to enhance microstructure based models for fatigue durability for aluminum based alloys.

#### 3.2 Materials

Three different microstructural variants of 8090 were to be used in this study on fatigue durability. The first was 3.2 inch thick plate, with a coarse unrecrystallized grain structure and weak deformation texture. The second was a 0.75 inch thick plate with thinner, more elongated unrecrystallized grains and a strong deformation texture. Finally, a recrystallized structure was to be produced to compare with the two unrecrystallized variants. It was also planned to initially artificially age these materials to the same temper so that the effects of

grain structure and texture may be analyzed, then later in the program, other conditions, such as underaged, overaged, or two-step reversion-aged, were to be produced as needed.

However, plans have been modified. The recrystallized 8090 variant has been deleted, and thus the opportunity to study grain structure and crystallographic texture will be severely restricted. The second material variant was successfully produced; however, evaluation of this material has been suspended. Since only the baseline, commercially produced 3.2 inch thick plate was completely characterized (microstructure and mechanical properties), this report primarily summarizes the results obtained on the 3.2 inch thick baseline 8090 material.

### 3.3 Microstructural Characterization

Samples for microstructural analysis were cut at the T/4 plate location, mounted, and prepared for optical microscopic examination. Micrographs of constituent particles were taken on the planes normal to L and LT at 50X of as-polished specimens and are shown in Figure 37. The equiaxed particles (in dark contrast) appear uniformly distributed throughout the area and weakly aligned in the rolling direction, as is typically observed in thicker plate product. The grain structure was revealed by anodizing the specimens, and micrographs were taken at 50X magnification. The very coarse grain structure in this 8090 plate is exhibited in Figure 38. The elongated, pancake shaped grains are often seen to be a few hundred microns in thickness. The unrecrystallized grain structure is usually attributed to the presence of  $Al_3Zr$  dispersoid particles.

Quantitative metallography was performed on both longitudinal (normal to the LT direction) and transverse (normal to L) sections at the T/4 plate location. A total area of  $31 \text{ mm}^2$  was characterized on each section using an automated optical image analysis system. The resolution limit at 100X magnification was  $1.55 \mu\text{m}$ . The quantitative metallography results are given in Table 14. The mean area fraction of particles is higher in the longitudinal section compared to the transverse section; however, the numbers are essentially the same ( $\sim 0.8 \%$ ) due to the large standard deviation. The large standard deviation also indicates that the particles are inhomogeneously distributed through the plate. A greater number of particles were captured on the transverse section ( $269 \text{ particles/mm}^2$ ) than on the longitudinal section ( $200 \text{ particles/mm}^2$ ). The largest particle encountered was



75  $\mu\text{m}$  in maximum projected length. Since the imaging magnification was low, individual particles separated by less than 1.55  $\mu\text{m}$  were analyzed as one particle.

Figure 39a shows a histograms of number of particles is plotted against the logarithm of particle size. The degree of clustering is also important, since a cluster of particles has a more deleterious effect on crack initiation than an isolated particle. Randomly oriented test lines were laid down on each field, and the surface to surface distance between particles was measured. A histogram of particle spacings is shown in Figure 39b. Shorter distances correspond to interparticle spacings.

In summary, the microstructural features span several orders of magnitude in size. The length of the unrecrystallized grains can be as much as a few millimeters, and the thickness up to hundreds of microns. On the other end of the scale, intermetallic constituent particles were measured to be as small as 1  $\mu\text{m}$  long. The critical size that defines a microstructurally small fatigue crack depends on the feature that controls fatigue.

Differential scanning calorimetry (DSC) was performed to identify any soluble constituent particles present in the as-received material. A disk weighing 45.40 mg, cut from the T/4 location, was heated at a rate of 20°C/minute from room temperature to 610°C (1130°F). Exothermic and endothermic peaks were identified on the resulting thermograms. The curve in Figure 40 shows a dissolution reaction that peaks at ~240°C (465°F), followed closely by a precipitation reaction at ~340°C (645°F). Other work done on 8090 has shown that the 230°C peak can be attributed to discrete  $\delta'$  ( $\text{Al}_3\text{Li}$ ) particle dissolution [19]. Although the material studied was artificially aged, S phase formation was not complete due to slow nucleation and growth kinetics. Thus, further precipitation of S phase during the DSC ramp is shown by the reaction at ~340°C.[19]

What is more important, no high temperature melting reactions were observed, which indicates that there were little or no soluble constituent particles present in the -T7 material. Therefore, the particles characterized by optical microscopy were insoluble precipitates, such as  $\text{Al}_7\text{Cu}_2\text{Fe}$  or  $\text{Mg}_2\text{Si}$ . Since these particles form during ingot casting, the only way to reduce their number and area fraction is to reduce the amount of impurity elements Fe and Si.

Guinier X-ray diffraction analysis can give qualitative measures of the crystallographic phases present in the material. A small piece of material from the T/4 plate location was thinned down to 0.040 inches thick, and prepared for Guinier x-ray analysis. Guinier

analysis identified only three phases. The metastable  $\delta'$  ( $\text{Al}_3\text{Li}$ ) phase was found to be present in 'medium' amounts. This agrees with the DSC results, which indicated that  $\delta'$  was present in the material. There was also a 'small-' amount of equilibrium  $\delta$  phase (small-) and a 'trace' of equilibrium  $\text{T}_2$  ( $\text{Al}_6\text{CuLi}_3$ ) phase. Guinier analysis did not detect any S ( $\text{Al}_2\text{CuMg}$ ) precipitation. Constituent particles such as  $\text{Al}_7\text{Cu}_2\text{Fe}$  were not detected, which means that they are present in very small volume fractions.

Pole figures were obtained from the T/4 location. Thin specimens (2 in. x 2 in. by 0.040 in.) were prepared parallel to the rolling plane, then analyzed by a combination of reflection and transmission diffraction. The 200 and 111 pole figures are shown in Figure 41. Although Al-Li is typically reported as having a very strong brass texture ( $\{110\}\langle 112\rangle$ ), this was not observed.

Table 15 contains the maximum and interpolated intensities for various texture components. While recrystallization components (cube and goss) are weak, the rolling components are also relatively weak. In particular, the brass texture was found to be only 1.55 times random. This weak rolling texture is consistent with the thick product form of the material. The hot deformation absorbed during processing to 3.2 inch thick plate only feebly affects the crystallographic texture at the T/4 location.

### 3.4 Mechanical Properties

Tensile testing was performed on the material to determine the standard tensile properties and the stress-strain response of the material. Duplicates of cylindrical specimens with gauge diameter 0.500 in., and length 2.00 in., were prepared in both the L and LT orientations for tensile testing. For these tests, fit-back elongation was measured. Tests for the determination of stress-strain behavior were performed on duplicate samples with rectangular cross-section (0.500 in. x 0.500 in.) and a 2.00 inch gauge length. Using the data from this test, the uniform elongation was separated from the total elongation.

Strain hardening exponents were obtained by fitting the true stress and true strain values to the Holloman equation,  $\epsilon = k\sigma^n$ , beyond  $\epsilon = 0.01$ . By ignoring the very low strain data, a better curve fit was obtained; however, the n-values were decreased. The k- and n-values reported in Table 16 are not strictly valid according to ASTM E646 specifications, since the specimen thickness exceeded 0.25 inches.

The results of the tensile tests are shown in Table 16. The yield strength in the L orientation was 60 ksi, about 6 ksi higher than in the LT orientation. The yield strength anisotropy is due at least in part to the crystallographic texture present in wrought product [20]. Note that the difference in the yield strength obtained between the two types of tests is small, i.e., less than the scatter between samples within a type of test.

Interestingly, the total elongation values depended on the type of test. The standard tensile test resulted in higher total elongation values compared to the stress-strain data, probably because of the extreme amount of crack deflection that occurred during fracture. Because the specimen halves fit together poorly, the values are higher than the actual values.

The strain hardening exponent was low in both orientations (0.07-0.09), as expected for this age-hardened aluminum alloy. The strain hardening exponent was consistently higher in the LT orientation compared to the L. The anisotropy is due to both crystallographic texture and the mechanical stretch given before artificial aging. In material with stronger crystallographic texture, the strain hardening exponents would probably show an even stronger dependence on test orientation. A high strain hardening exponent signals diffuse strain, whereas a low strain hardening exponent indicates localized strain.

One specimen each in the L and LT orientations had uniform elongation values that equaled the total elongation values, suggesting premature failure. However, the other specimens failed by plastic instability at modestly higher strengths and elongation values. Thus, the failure in two of the specimens was only slightly premature.

Fracture toughness was evaluated using C(T) toughness specimens centered at the T/4 plate location with thickness  $B=1.25$  inch. Specimens were precracked by fatigue cycling prior to testing. The results of the fracture toughness tests are shown in Table 16. Three of the four specimens failed the validity criteria; hence,  $K_Q$  values are quoted rather than  $K_{Ic}$ . The average toughness in the L-T orientation was  $37.2 \text{ ksi}\sqrt{\text{in}}$ , and in the T-L orientation was  $29.2 \text{ ksi}\sqrt{\text{in}}$ .

In the L-T specimens, deep, intergranular splitting parallel to the loading direction were observed. High fracture toughness values have been attributed to the crack dividing splitting mechanism [21-23]. Delamination along grain boundaries reduces the stress triaxiality, and the material fails locally in a more plane stress state. This extrinsic toughening mechanism results in higher apparent plane strain toughness values. Since high angle grain boundaries lie parallel to the rolling plane, crack dividing splitting can occur in

both the L-T and T-L test orientations. However, the L-T orientation displays more splitting than the T-L orientation, and this difference may be due to the anisotropy in yield strength. The L-T orientation had a higher yield strength; thus higher stresses built up at the high angle grain boundaries, and the grain boundaries then separated. In the T-L orientation, the matrix strength and the grain boundary strength were probably much closer in the material condition under study. Another reason cited in the literature is the difference in grain boundary length [24]. Specimens tested in the L-T orientation can develop long splits that grow parallel to the rolling direction. Because the grains were elongated rather than equiaxed, the splits were shorter in the T-L orientation. The difference in intergranular split length may also contribute to the orientational dependence of toughness.

Strain hardening is a material property that, along with elastic modulus and yield strength, intrinsically affects fracture toughness. Several models have been developed that directly relate the strain hardening exponent to toughness. Although the LT tensile test orientation showed a 20% higher  $n$ -value than the L orientation, this strain hardening advantage did not translate into a superior toughness due to the lower yield strength and difference in intergranular splitting behavior.

### 3.5 8090 Fatigue Testing

Smooth S/N fatigue testing has been performed for the first microstructural variant of 8090 using cylindrical specimens with 0.300 inch gauge diameter and 1.2 inch gauge length. Five specimens were tested at four stress levels for a total of 20 specimens. Both longitudinal (L) and long transverse (LT) specimen orientations were tested. The highest maximum stress level, 45 ksi, corresponded to 75% of the yield strength in the L orientation and 85% of the yield strength in the LT orientation. Tests using 30 Hz frequency were performed in ambient air at  $R=0.1$ . The results of the smooth axial fatigue tests are tabulated in Table 17, and also plotted in Figure 42a. The L orientation seems to have stronger fatigue resistance than the T orientation, since at all stress levels, the L orientation specimens exhibit longer lifetimes to failure. Because the yield strengths in the two orientations differed by 10%, the S/N data was replotted with the maximum stress normalized by the yield stress (Figure 42b). In this representation, there is little difference in fatigue resistance between the L and T orientations. Thus, the difference in L and T orientation fatigue behavior may be attributed to the anisotropy in yield strength. Another

example of the effect of yield strength on fatigue behavior was provided by Xu et al. [25] who found that the fatigue strength of 8090 increased when the test temperature decreased from 25°C to -200°C. The drop in test temperature produced an increase in the yield strength of the material, as thermally activated deformation processes diminished.

To evaluate the effect of a stress concentrator on fatigue performance, flat, two open hole specimens were used, similar to the fatigue characterization of 7050. Specimens from the T/4 location were 0.125 inches thick, with two holes 0.187 inches in diameter separated by 1.000 inches. These specimens were also tested in ambient air, with a load ratio of  $R=0.1$  and a frequency of 30 Hz. Some of the specimens failed in the grip area, and were reloaded and tested to either failure or  $10^7$  total cycles. Figure 43 shows the S/N fatigue behavior for the open hole specimens and the data are tabulated in Table 18. Specimens that first broke in the grip and were subsequently reloaded are plotted as single points according to the total number of cycles. In these open hole specimens, the L orientation did not exhibit longer lifetimes than the LT orientation; data at all four stress levels seems to overlap. Thus, the presence of the stress concentrator outweighs other factors in the crack initiation behavior.

The lifetimes measured include both crack initiation and propagation regimes. In high cycle, low stress fatigue tests most of the total lifetime is consumed by the crack initiation process. In contrast, initiation takes an insignificant amount of time in low cycle fatigue tests. Shielding mechanisms, such as crack deflection and bifurcation, are known to strongly affect the fatigue crack growth behavior, but have little effect on the initiation behavior.

### 3.6 Fractography

Fractographs in Figures 44-47 show the fracture profile for specimens tested in the L and LT orientations at high (45 ksi) and low (30 ksi) stress levels. It is immediately seen that the fatigue cracks propagated at a high angle, especially in the L orientation. While such crack angles are frequently observed in the crystallographic Stage I crack initiation, cracks usually begin to propagate along the plane of maximum tensile stress immediately thereafter. The large amount of crack deflection throughout the fatigue crack initiation and growth regimes reduces the driving force at the crack tip, and probably contributes to the long lifetimes.

The area of the specimen that failed in fatigue was easily distinguished from the area that failed by tensile overload. The overall fracture surface was imaged normal to the loading axis (Figure 48). As seen, the fatigue region was thumbnail-shaped, and very small in area. Figure 49 shows higher magnification images of typical regions of tensile overload in L and LT specimens.

Although the overall fatigue region was recognizable, it was difficult to detect the crack initiation site(s). In this material, obvious initiation by large Fe-containing particles at the specimen free surface was not observed in any condition. Areas with cleavage-like river lines were noted, which suggests Stage I initiation mechanism.

### 3.7 Future Work

All further efforts on the effects of microstructure on fatigue durability using 8090 as the model material have been suspended. Characterization of the microstructure and mechanical properties of the baseline, unrecrystallized variant is complete. However, all scaling law efforts that depended on results of Al-Li research have been abandoned, and no further work is planned in this area.

## 4. Microstructural Based Fatigue Modeling

### 4.1 Background

The objective of the modeling work is to provide probabilistic component life assessments using quantitative descriptions of representative material microstructures. The approach first requires a mechanistic understanding of fatigue initiation in the materials of study and a quantification of the controlling microstructural features. The next step is to establish a method of scaling the distributions of material microstructural features from random plane microstructural characterization to predict the extreme value distribution of microstructural features causing failure. The final step is the development of probabilistic models which enable prediction of component life based on the characterizations of the controlling microstructural features.

### 4.2 Growth Modeling

Modeling the influence of microstructure on the fatigue life of a component requires an understanding of fatigue damage mechanisms. Several tests need to be conducted to identify and quantify the controlling microstructural features. Examination of fracture surfaces from both smooth axial and open hole fatigue tests enable qualification of the extreme value distribution of features affecting fatigue initiation. For the 7050 thick plate materials used in this study, the major microstructural features are microporosity and constituent particles.

The basis of the modeling is a fracture mechanics program on crack coalescence developed by Grandt et. al.[26]. The original program calculated the fatigue life of a notch specimen with a fatigue crack growing from an equivalent elliptical crack. It considered crack coalescence for multiple cracks and interaction of cracks at opposite sides of a hole. To incorporate different microstructural features as initiation sites for crack growth (in particular microporosity and constituent particles), a modification of the Trantina and Barishpolsky [27] stress intensity factor solutions was used. The problem Trantina and Barishpolsky examined consisted of an ellipsoidal void or inclusion which contains an equatorial crack of length  $b$  as shown in Figure 50. The void height is  $h$ , its width is  $2R$ , the crack extends a uniform length  $b$  around the void equator ( $x$ - $y$  plane), and a remote

stress  $\sigma$  is applied in the  $z$  direction perpendicular to the plane of crack growth. An effective stress intensity factor  $K$  for this flaw geometry is

$$K = \beta \sigma (\pi b)^{1/2} \quad (1)$$

where the dimensionless geometric term  $\beta$  is given by

$$\beta = 2/\pi + B(1.12K_t - 2/\pi - 1)(R/(b+R))^{1.0} + (R/(b+R))^{1.8} \quad (2)$$

Here  $K_t$  is the elastic stress concentration factor for the ellipsoidal void or inclusion (without the crack), and depends on the aspect ratio  $h/2R$ . The constant  $B$  is 1.0 for a void, 2.0 for a bonded cracked inclusion, and 0.3 for an unbonded inclusion. Note in Figure 50 that the total length of the initial cracked inhomogeneity is  $2R + 2b$ . Since  $b$  is the physical crack length, the ratio  $R/(b+R)$  in Equation (2) represents the portion of the initial inhomogeneity which is assumed to be cracked. When  $b \gg R$ , this ratio = 0, and Equations (1) and (2) reduce to the stress intensity factor solution for an "ideal" embedded elliptical crack (i.e., the void or inclusion no longer has an influence on  $K$ ). At the other extreme, when  $b = 0$ ,  $R/(b + R) = 1$ , so that the stress intensity factor is zero from Equation (1) and (2) (i.e. the inhomogeneity is no longer cracked). Since it is not known a priori what portion of the initial inhomogeneity should be treated as a crack, the ratio  $R/(b+R)$  in Equation (2) is treated as an experimental parameter [28].

The Trantina-Barishpolsky stress intensity factor solution must be modified to account for the location of the microstructural feature near the bore of the hole and the noncircularity of the feature. This was accomplished by defining the following stress intensity factor:

$$K = (K_{T-B}/K_{penny})^* K_{N-R} \quad (3)$$

Here  $K_{T-B}$  is the Trantina-Barishpolsky stress intensity solution for an infinite plate,  $K_{penny}$  is the stress intensity solution for a circular penny shaped crack in an infinite body, and  $K_{N-R}$  is the Newman and Raju [29] stress intensity factor solution for a surface or corner crack. To account for noncircular cracks, crack growth in the major and minor directions were analyzed by defining  $K_{penny}$  with respect to the major and minor axes.

When a test specimen is examined, the dimensions and location of the microstructural feature can be measured on the fracture surface. These values can be used to calibrate the model or test the model. Figure 51 shows the calculations for a pore at the center of a bore hole and an inclusion at a corner. The model accurately calculated both fatigue lives.



However, before fracture the exact location and size of the feature are unknown and should be considered as random variables. Distributions for feature size, shape, location, and type can be determined from examination of the fracture surfaces from failed test specimens. These distributions can then be used to calculate the distribution of fatigue life. This is shown schematically in Figure 52.

The model can now be used to examine the effects of changing the distributional characteristics of the material. Table 19 compares the fatigue improvements based on four different distributional assumptions. The first material is old quality 7050 thick plate. The microstructural feature is microporosity with a Weibull ( $\mu = 0.204$ ,  $\sigma = 0.044$ , 0) size distribution located randomly along the bore of the hole. The fatigue stress at 100000 cycles is 110 MPa. The second material is a new quality 7050 thick plate that has a measured microporosity distribution of Weibull ( $\mu = 0.112$ ,  $\sigma = 0.036$ , 0). The fatigue stress at 100000 cycles is 125 MPa. For the low porosity material, the size of microporosity is significantly reduced but the failures now occur at particles located near the hole corners and the resulting fatigue lifetimes are not improved over the new quality plate. Thus to improve the open hole fatigue performance, a concurrent reduction in both the microporosity and the constituent particle levels is required. It is predicted that this could give a fatigue stress at 100000 cycles of 150 MPa. This should represent the fatigue performance of the low particle plate where specimens were taken from the T/4 location and thus had reduced microporosity levels along with the reduction in particle sizes.

When comparing material and performing trade studies it would be useful if the size distribution of features controlling fatigue initiation measured on a fracture surface could be determined without conducting a large number of fatigue tests. Quantitative metallography, performed on polished (random) cross sections, characterizes the average micropore or particle size (or distributional information). However, fatigue cracks initiate at the largest flaws and are thus controlled by the extreme values of the distribution. Therefore, it is important to understand the relationship between polished random surfaces and fracture surfaces. Extreme value statistics using the surface area at the high stressed location for scaling could be used to convert random surface distributions to fracture surface distributions.

As an example of the above method 40 fields were measured on random surfaces of a 7050 thick plate using an optical microscope. Each field measuring  $773332.3 \mu\text{m}^2$  for a total of  $30.9333 \text{ mm}^2$ . The total number of particles measured were 4256. The maximum

dimension followed a lognormal distribution with  $\lambda = 2.364$  and  $\zeta = 0.5639$ . The extreme value distribution when the original distribution is lognormal can be shown to be

$$FX_n(y) = \exp(- (v_n/y)^\kappa) \quad (4)$$

where  $v_n$  and  $\kappa$  are parameters based on the number of samples and  $y$  is the maximum size. For the standard 0.5 in. round specimen the parameters are  $v_n = 134.7$  and  $\kappa = 8.88$ . Measurements using a scanning electron microscope were also made on the plate. This resulted in a smaller total area (1.2385 mm<sup>2</sup>) measured and fewer particles (137 Fe particles). The maximum dimension distribution was also lognormal with  $\lambda = 1.995$  and  $\zeta = 0.6403$ . The extreme distribution for the 0.5" dia specimen has the following parameters,  $v_n = 127.5$  and  $\kappa = 7.753$ . A comparison of these two distributions is shown in Figure 53. Fatigue life predictions based on this assumption have not yet been made, however, distributions have been derived from the random plan which are similar to fracture distributions. This indicates that a feature's size distribution will be conditioned on the area from that it was measured.

Finally, the above model does a good job of predicting fatigue life at relatively high stresses. As the fatigue stress is lowered and the material is improved, the model under predicts the fatigue life. A possible reason for this is that at low stresses and for very small microstructural features, the initiation stage of fatigue is contributing a larger fraction of the total lifetime of the specimen. Thus it is necessary to have some way of predicting the time to initiate a crack.

#### 4.3 Initiation modeling

Using probabilistic estimates of the initiation life and the above growth model will provide more accurate fatigue predictions. This model will enable detailed trade studies involving materials with different microstructures. However, first an initiation model which is linked to the microstructure must be developed. Two differing methods are currently being investigated under this project and concurrently on other projects.

The first procedure starts with a detailed characterization of microstructural features from which fatigue cracks initiate. The effects of inhomogeneity type (micropore or constituent particle), size, shape, location, and clustering are being incorporated into a deterministic model based on metallographic images of the microstructure. Once this model has been

demonstrated probabilistic information will then be included. Fatigue cracks in 7050 thick plate develop at porosity and clusters of constituent particles. Figure 54 shows a cluster of particles of the type that could initiate a fatigue crack. The simplest characterization of the cluster is an ellipsoidal region with an effective elastic modulus,  $E_p$ , related to the local volume fraction. The stress concentration in the matrix as a function of the ratio of  $E_p/E_m$  and ellipsoid shape can then be determined. The plot in Figure 55 shows that for hard particles,  $E_p/E_m > 1$ , the stress concentration in the matrix is insensitive to shape while for "soft" particles and voids the stress concentration is highly sensitive to shape.

Treating the ellipsoidal region as an effective medium assumes that the only information required is the local volume fraction. A finite element model can be used to account for the structure within the ellipsoidal region, Figure 56. Detailed stress and strain fields around the cluster of particles can provide information on that to base a measure of initiation life. It is expected that residual stress effects will be important for near surface particles and particle clusters. Once the FE based model is developed important distributional information can be included.

An alternate method of modeling crack initiation is with the Stochastic Theory of Fatigue, Emptage and Shaw [30]. This theory is based on a combination of the theory of diffusion in the presence of a stress field with activated state theory. While it would not give a quantitative link between microstructural features and fatigue initiation, it is likely that the distribution of initiation life could be modeled. This could easily be the starting point for a growth model.

#### 4.4 Application of models

One application of the model is comparing the initial size distributions of microstructural features that have equivalent fatigue lives. For example, as the microporosity is reduced in 7050 thick plate, constituent particles will become the next feature to initiate cracks. Thus, the size distribution of particles located at a corner of a hole that has the same distribution of fatigue lives as the new quality plate was calculated, Figure 57. When a low porosity 7050 variant thick plate material was tested, the size distribution of particles on the fracture surface causing initiation compared well to the calculated distribution, Figure 58. The next logical improvement is reducing the size and number of particles in the material. A sufficient change in particle distribution would drive the failure mode back to porosity.

Table 19 compares the fatigue stress at  $10^5$  cycles for old quality, new quality, low porosity, and low particle plates. The models predict a 36 % increase in stress level for the low particle - low porosity plate.

The models under development are material generic in the sense that given the proper material microstructural distributions, the fatigue life could be determined. This enables the models to be used to compare not only differing qualities of the same material but different alloys. A material with better crack growth characteristics versus one with a smaller initial size distribution could be compared at a given low probability of crack exceedence.

The probabilistic nature of the models allows the engineer to set an acceptable part reliability and design (or evaluate) the part to this level of reliability. This is demonstrated by comparing inspection intervals for the two qualities of 7050 thick plate [31]. Using the initial size distributions given above and reliability index of 3.71 (probability of failure of 0.0001) the inspection intervals were 3450 flight hours and 4350 flight hours. The degradation of reliability with flight hours is shown in Figure 59. Similar types of comparisons can be made for design examples also.

#### 4.5 Summary of Modeling Work

Examination of the fracture surfaces from fatigue tests of 7050 alloy plate indicate that constituent particles and microporosity are the major sites of fatigue crack initiation and growth. The probabilistic characterization of these sites has been completed for two qualities of materials. Work on developing the failure distributions from distributions determined on a random plan has begun.

Models for predicting fatigue initiation and growth are under development. The growth model is completed for an open hole specimen configuration. The probabilistic description of the model parameters has been included in the growth model. This enables comparison of component reliability based on changes in material quality.

#### 4.6 Future Work

An area of future work is to complete the initiation modeling and incorporate it into the growth model. Work on the finite element and the stochastic fatigue approaches are continuing and should be completed in 1993. After the models are completed they will be incorporated into the growth model.

Another area of future work is the modeling of the "short crack " growth characteristics of the material. Short crack growth exhibits more scatter and different distributional characteristics from long crack growth. Thus in a probabilistic model it is important to understand the short crack growth regime.

## 5. Summary

- Five microstructural variants of alloy 7050 plate have been evaluated. The hierarchy of microstructural features which affect the fatigue initiation process have been identified. The controlling microstructural features are, in order of their influence on fatigue initiation, microporosity, constituent particles, grain structure.
- Extrinsic sources of damage initiation may affect fatigue durability. The quality of holes in open hole fatigue specimens was seen to override influences of microstructure in controlling fatigue lifetimes. However, when simple procedures were used to ensure good quality holes (de-burring), damage initiation was shifted back to intrinsic microstructural sources. Thus, the lifetime improvement associated with reductions in microstructural inhomogenities can be realized for structural applications when manufacturing quality is controlled.
- The quantification of microstructural features metallographically on random cross sections is key to developing predictive strategies for fatigue durability based on microstructure. Constituent particle distributions in 7050 plate have been quantified and are provided as input for models to predict fatigue initiation.
- Two of the three proposed microstructural variants of Al-Li alloy 8090 plate have been obtained, and testing and evaluation is in progress. However, due to changes in program emphasis all work on the Al-Li has been suspended. Formal notification from the ONR of the desire to stop this work will be sought.
- A microstructure based modeling approach has been demonstrated for alloy 7050 plate. The approach uses a growth model to predict fatigue lifetimes from extreme value distributions of microstructural features. The incorporation of models to predict initiation from microstructural features is being sought.

## **6. Acknowledgements**

This work was supported by the Office of Naval Research under ONR Contract No. F33615-92-C-5914. The guidance of Dr. A. K. Vasudevan of the ONR is gratefully acknowledged. The authors also wish to thank Dr. M. A. Przystupa of UCLA for insightful discussions. The technical assistance and support of Messrs. R. L. Rolf, T. N. Rouns, T. C. Conner, and D. K. White of Alcoa is greatly appreciated.

## 7. References

1. "USAF Durability Design Handbook: Guidelines for the Analysis and Design of Durable Aircraft Structures," S. D. Manning and J. N. Yang, AFWAL-TR-83-3027, Air Force Wright Aeronautical Laboratories, Aug. 1988.
2. "Exudation of Material from Slip Bands at the Surface of Fatigued Crystals of an Aluminum-Copper Alloy," P. J. E. Forsythe, *Nature*, Vol. 171, 1953, pp. 172-173.
3. "Effect of Microporosity on Fatigue Durability of Thick 7050 Aluminum Plate," P. E. Magnusen, R. J. Bucci, A. J. Hinkle, J. G. Burns, and J. L. Rudd, presented at 1992 USAF Structural Integrity Program Conference, San Antonio, TX, Dec. 1-3, 1992, to appear in conference proceedings.
4. "Aluminum Quality Breakthrough for Aircraft Structural Reliability," C. R. Owen, R. J. Bucci and R. J. Kegarise, *Journal of Aircraft*, Vol. 26, No. 2, Feb. 1989, pp. 178-184.
5. "The Influence of Material Quality on Airframe Structural Durability," P. E. Magnusen, R. J. Bucci, A. J. Hinkle, M. E. Artley and R. L. Rolf, published in *Advances in Fracture Research*, Eds. K. Salama, K. Ravi-Chandar, D. M. R. Taplin and P. Rama Rao, Pergamon Press, 1989, pp. 999-1006.
6. "Durability Assessment Based on Initial Material Quality," P. E. Magnusen, A. J. Hinkle, W. T. Kaiser, R. J. Bucci and R. L. Rolf, *Journal of Testing and Evaluation*, Vol. 18, No. 6, Nov. 1990, pp. 439-445.
7. "Effect of Microporosity on Notched Specimen Fatigue Life," A. J. Hinkle, P. E. Magnusen, R. L. Rolf, and R. J. Bucci, published in *Structural Safety and Reliability*, Eds., A. H-S. Ang, M. Shinozuka and G. I. Schueller, American Society of Civil Engineers, 1989, pp. 1467-1474.
8. "Methodology for the Assessment of Material Quality Effects on Airframe Structural Durability," P. E. Magnusen, A. J. Hinkle, R. J. Bucci, R. L. Rolf and D. A. Lukasak, published in *Fatigue '90, Vol. IV*, Eds. H. Kitagawa and T. Tanaka, MCE Publications Ltd., 1990, pp. 2239-2244..



9. "Probabilistic Durability Evaluation of Alcoa 7050 Aluminum," J. G. Burns, J. L. Rudd, J. A. Harter, P. E. Magnusen, A. J. Hinkle, and R. J. Bucci, Proceedings of the 1991 USAF Structural Integrity Program Conference, Eds., T. W. Cooper, J. W. Lincoln, R. M. Bader, WL-TR-92-4045, Wright Patterson AFB, Ohio, July 1992, pp. 305-322.
10. "Modeling the Influence of Initial Material Inhomogeneities on the Fatigue Life of Notched Components," A. F. Grandt, A. J. Hinkle, T. D. Scheumann, and R. E. Todd, submitted for publication to *Fatigue and Fracture of Engineering Materials and Structures*, presented at USAF Structural Integrity Program Conference, San Antonio, TX, Dec. 2-5, 1991.
11. "Analysis of Fatigue Life Data Using the Box-Cox Transformation," A. J. Hinkle, and M. R. Emptage, *Fatigue and Fracture of Engineering Materials and Structures*, Vol. 14, No. 5, 1991, pp. 591-600.
12. "Probabilistic Methods for Durability and Damage Tolerance Analysis," A. J. Hinkle, R. Skjong, and G. Sigurdsson, presented at 1992 USAF Structural Integrity Program Conference, San Antonio, TX, Dec. 1-3, 1992, to appear in conference proceedings.
13. "The Statistical Aspects of Fatigue of Materials," A. M. Freudenthal, *Proc. Roy. Soc.*, Vol. A187, 1946, p. 416.
14. "A Reinforced Material Model Using Actual Microstructural Geometry," J. R. Brockenbrough, W. H. Hunt, Jr., O. Richmond, *Scripta Metallurgica et Materialia*, Vol. 27, 1992, pp. 385-390.
15. "Cracks Emanating from Holes in Plate Stress," D. Broek and H. Vlieger, *International Journal of Fracture Mechanics*, Vol. 8, 1972, pp. 353-356.
16. T. N. Rouns, J. M. Fridy, K. B. Lippert, O. Richmond, "Quantitative Characterization and Modeling of Second Phase Populations Through the Use of Tessellations," *Simulation and Theory of Evolving Microstructures*, ed. M. P. Anderson and A. D. Rollet, TMS 1990, pp. 269-275.
17. Morris, W. L., "Microcrack Closure Phenomena for Al 2219-T851," *Metall. Trans. A*, 10A, 7 (1979) 5-11.

18. "Fatigue Crack Initiation and Microcrack Growth in 2024-T4 and 2124-T4 Aluminum Alloys", C. Y. Kung and M. E. Fine, Metallurgical Transactions A, Vol. 10A, May 1979, pp. 603-610.
19. A. K. Mukhopadhyay, C. N. J. Tite, H. M. Flower, P. J. Gregson and F. Sale, "Thermal Analysis Study of the Precipitation Reactions in Al-Li-Cu-Mg-Zr Alloys," Aluminum-Lithium IV, Proc. of the 4th International Aluminium Lithium Conference, 10-12 June 1987, Paris France, ed. G. Champier, B. Dubost, D. Mannay, L. Sabetay, J. de Physique, Col. 20, pp. 439-446.
20. A. K. Vasudevan, W. G. Fricke, Jr., R. C. Malcolm, R. J. Bucci, M. A. Przystupa and F. Barlat, "On Through Thickness Crystallographic Texture Gradient in Al-Li-Cu-Zr Alloy," *Metall. Trans. A*, 19A, 3 (1988) 731-732.
21. K. T. Venkateswara Rao, H. F. Hayashigatani, W. Yu and R. O. Ritchie, "On the Fracture Toughness of Aluminum-Lithium Alloy 2090-T8E41 at Ambient and Cryogenic Temperatures," *Scr. Metall.*, 22 (1988) 93-98.
22. K. S. Chan, "Evidence of a Thin Sheet Toughening Mechanism in Al-Fe-X Alloys," *Metall. Trans. A*, 20A (1989) 155-164.
23. K. T. Venkateswara Rao and R. O. Ritchie, "Influence of Extrinsic Crack Deflection and Delamination Mechanisms on the Cryogenic Fracture-Toughness of Commercial Al-Li Alloys," *Al-Li V*, *ibid* (1989).
24. J. Glazer, "The Strength-Toughness Combination of the Aluminum-Lithium Alloys 2090 and 2091 at Cryogenic Temperatures," PhD Dissertation, University of California at Berkeley, July 1989.
25. Xu, Y. B., L. Wang, Y. Zhang, Z. G. Wang and Q. Z. Hu, "Fatigue and Fracture Behavior of an Aluminum-Lithium Alloy 8090-T6 at Ambient and Cryogenic Temperature," *Metall. Trans. A*, 22A, 3 (1991) 723-729.
26. "An Experimental and Numerical Investigation of the Growth and Coalescence of Multiple Fatigue Cracks at Notches", A. F. Grandt, A. B. Thakker, and D. E. Tritzsch, *Fracture Mechanics: Seventeenth Volume*, ASTM STP 905, 1986, pp. 239-252.

27. "Elastic-Plastic Analysis of Small Defects - Voids and Inclusions", G. G. Trantina, and M. Barishpolsky, *Engineering Fracture Mechanics*, Vol. 20, No. 1, 1984, pp. 1-10.
28. "Modeling the Influence of Initial Material Inhomogenities on the Fatigue Life of Notched Components," A. F. Grandt, Jr., A. J. Hinkle, T. D. Scheumann, and R. E. Todd, Submitted for publication in *Fatigue and Fracture of Engineering Structures*. Presented at USAF Structural Integrity Program Conference, Dec. 2-5, 1992.
29. Newman, J. C. and Raju, I. S., "Stress intensity Factor Equations for Cracks in Three-Dimensional Finite Bodies", NASA Technical Memorandum 83200, Langley Research Center, Hampton, VA, August, 1981.
30. Emptage, M. R., Shaw, B. J., "A Stochastic Model for Crack Initiation and Fatigue Life", Probabilistic Mechanics and Structural and Geotechnical Reliability, 6th Specialty Conference, Denver, July 8-10, 1992, pp. 308-311.
31. Sigurdsson, G., Cramer, E. H., Hinkle, A. J., Skjong, R., "Probabilistic Methods for Durability and Damage Tolerance Analysis", Presented at the 1992 USAF Structural Integrity Program Conference, San Antonio, TX, 1-3 Dec 1992.

Table 1. Summary of the 7050 materials used in this study and the key microstructural features which may affect fatigue damage initiation.

Material	Product Thickness (in.)	Key Microstructural Features
Old Quality Plate	5.7	Large porosity
New Quality Plate	5.7	Porosity
Low Porosity Plate	6.0	Small porosity, constituent particles
Low Particle plate	6.0 (T/4)	Small constituents, thick plate grain structure
Thin Plate	1.0	Refined grain size and constituent particles

Table 2. Smooth axial stress fatigue lifetimes of the old and new quality thick plate materials tested at 35 ksi maximum stress,  $R=0.1$ , frequency = 10 Hz, in laboratory air.

Old Quality Plate Fatigue Lifetime (cycles)	New Quality Plate Fatigue Lifetime (cycles)
49449	75288
55090	103836
57456	107027
58014	107171
58896	107810
58943	108906
62270	112400
62379	112761
63122	114758
64419	116371
64512	118400
66885	119033
67576	120531
68266	120887
68768	128412
70044	128882
70511	133345
71263	135235
71508	135330
72521	135682
73524	138373
73549	140414
74019	141312
76094	149256
77218	150733
77251	150869
78366	153272
78557	167284
78566	183048
79290	183864
84529	197529
86811	197811
90017	203406
100708	207258
101013	207904
105447	243624
121650	256610
149486	271941
151046	281576
230417	382160
	395136
	432631
	472097

Table 3. Open hole specimen fatigue lifetimes of the old and new quality thick plate materials tested at , R=0.1, frequency = 30 Hz, in laboratory air.

Old Quality Plate		New Quality Plate	
Max. Net Stress (ksi)	Fatigue Lifetime (cycles)	Max. Net Stress (ksi)	Fatigue Lifetime (cycles)
14.8	222798	20.0	1140859
14.8	323600	20.0	5439135
14.8	2951624	20.0	9559168
14.8	356549	20.0	10000000*
14.8	313328	20.0	10000000*
14.8	309256	22.5	84802
14.8	738525	22.5	266450
14.8	384130	22.5	2556780
14.8	4990222	22.5	3682500
14.8	214355	22.5	4103734
18.5	119328	25.0	55848
18.5	164739	25.0	141250
18.5	109775	25.0	180413
18.5	119278	25.0	195180
18.5	180611	25.0	198871
18.5	181971	30.0	32871
18.5	171245	30.0	39402
18.5	969579	30.0	39978
18.5	172288	30.0	46207
24.6	35785	30.0	49267
24.6	33910		
24.6	47812		
24.6	45406		
24.6	46641		
24.6	49285		
24.6	42889		
24.6	45836		
24.6	49292		
24.6	55290		
30.8	27500		
30.8	28323		
30.8	20590		
30.8	17806		
30.8	19967		
30.8	17888		
30.8	22011		
30.8	23754		
30.8	25557		
30.8	15949		

\* Specimen did not fail.

Table 4. Calculated stress corresponding to specified lifetime for open hole fatigue tests of new and old quality plate based on Box-Cox transformation analysis of the data.

Metal Quality	Maximum Net Stress (ksi)			
	10 <sup>5</sup> Cyclic Lifetime		Infinite Lifetime	
	Mean	95% Lower Conf. Limit	Mean	95% Lower Conf. Limit
Old Quality	20.1	16.9	10.8	7.7
New Quality	26.5	22.6	17.7	13.9
% Change	32%	34%	64%	81%

Table 5. Smooth axial stress fatigue lifetimes of the new quality and low porosity thick plate materials tested at 40 ksi maximum stress, R=0.1, frequency = 10 Hz, in laboratory air.

New Quality Plate Fatigue Lifetime (cycles)	Low Porosity Plate Fatigue Lifetime (cycles)
35904	167376
53997	201840
56700	237544
56758	250480
61998	298211
64127	380594
67833	422354
68977	461445
68977	483758
72568	497462
76699	513329
82611	612652
87348	702581
88248	960660
93830	997175
98076	1000000*
104098	1000000*
121259	1000000*
123271	1000000*
123710	
127258	
149077	
149745	
356202	

\*Specimen did not fail.



Table 6. Open hole specimen fatigue lifetimes of the low porosity thick plate and the thin plate materials tested at , R=0.1, frequency = 30 Hz, in laboratory air.

Low Porosity Plate		Thin Plate	
Max. Net Stress (ksi)	Fatigue Lifetime (cycles)	Max. Net Stress (ksi)	Fatigue Lifetime (cycles)
20.0	428453	28.0	1220516
20.0	5877762	28.0	2889780
20.0	7428034	28.0	3560315
20.0	10000000*	28.0	1258308
20.0	10000000*	28.0	3155274
22.5	230350	30.0	64367
22.5	782052	30.0	932041
22.5	1188050	30.0	661553
22.5	94081	30.0	145498
25.0	58740	30.0	237611
25.0	106857	30.0	1421982
25.0	136467	30.0	212123
25.0	111781	32.5	56390
25.0	852700	32.5	177300
30.0	43998	32.5	52476
30.0	52939	32.5	49150
30.0	51641	32.5	49470
30.0	49750	35.0	71850
30.0	58535	35.0	52287
		35.0	44815
		35.0	65332
		35.0	50498

\*Specimen did not fail.

Table 7. Open hole specimen fatigue lifetimes of the low particle thick plate material tested at , R=0.1, frequency = 30 Hz, in laboratory air.

Low Particle Plate	
Max. Net Stress (ksi)	Fatigue Lifetime (cycles)
25.0	2889780
25.0	3560315
25.0	1258308
25.0	3155274
25.0	64367

Table 8. Hierarchy of fatigue initiating features in 7050-T7451 plate.

Material	Dominant Microstructural Feature		
	Smooth Fatigue (round bars)	Open Hole Fatigue	
		as-machined holes	de-burred holes
Old Quality Plate	Coarse Microporosity	Coarse Microporosity	Coarse Microporosity
New Quality Plate	Microporosity	Hole Quality/ Microporosity	Microporosity
Low Porosity Plate	Fine Microporosity	Hole Quality	Constituent Particles
Low Particle Plate	–	–	Grain Structure
Thin Plate	Grain Structure/ Constituent Particles	–	Grain Structure/ Constituent Particles

Table 9. Select parameters for constituent particles in two 7050 materials, showing the effect of plate location and processing. Analysis was performed at 100X magnification.

feature	New Quality			Low Porosity		
	T/10	T/4	T/2	T/10	T/4	T/2
<b>area fraction</b>						
mean, %	1.31	1.17	0.99	1.17	1.21	0.98
std dev, %	0.17	0.16	0.18	0.12	0.21	0.18
<b>no. of particles</b>	9376	6495	5136	7977	6330	4256
<b>particle density, mm<sup>-2</sup></b>	303.1	210.0	166.0	257.9	204.6	137.6
<b>longest dimension</b>						
maximum, $\mu\text{m}$	80.2	95.8	90.4	53.4	86.0	108.3
mean, $\mu\text{m}$	10.3	12.0	12.0	10.2	11.9	12.7
std dev, $\mu\text{m}$	$\pm 5.5$	$\pm 7.4$	$\pm 7.7$	$\pm 5.3$	$\pm 7.2$	$\pm 9.3$
<b>aspect ratio</b>						
mean	0.587	0.565	0.587	0.616	0.587	0.596
std dev	0.167	0.178	0.171	0.164	0.175	0.170
<b>area</b>						
mean, $\mu\text{m}^2$	42.0	54.2	57.6	44.2	57.5	67.2
std dev, $\mu\text{m}^2$	34.4	55.9	60.3	36.6	59.8	82.8
<b>perim</b>						
mean, $\mu\text{m}$	28.8	33.2	33.9	29.1	33.7	36.1
std dev, $\mu\text{m}$	14.7	20.8	22.2	14.5	20.9	26.7
<b>feret x distance</b>						
mean, $\mu\text{m}$	198	191	172	195	173	164
std dev, $\mu\text{m}$	198	204	211	200	208	214

Table 10. Number of particles counted in new quality and low porosity materials in the specimen area of 31 mm<sup>2</sup>.

particle size		New Quality			Low Porosity		
$\mu\text{m}$	$\log(\mu\text{m})$	T/10	T/4	T/2	T/10	T/4	T/2
4.8978	0.69	1401	775	643	1215	767	645
6.0256	0.78	2047	1135	936	1664	1108	711
7.4131	0.87	1420	867	688	1304	832	518
9.1201	0.96	1607	1066	829	1377	1038	606
11.220	1.05	1125	809	554	865	783	457
13.804	1.14	808	697	562	698	670	405
16.982	1.23	494	467	374	449	470	351
20.893	1.32	259	329	249	242	336	209
25.704	1.41	132	184	156	112	189	170
31.623	1.50	56	92	83	40	79	93
38.905	1.59	19	49	33	8	39	40
47.863	1.68	5	17	19	3	12	34
58.884	1.77	1	5	6	0	4	7
72.444	1.86	2	1	3	0	3	6
89.125	1.95	0	2	1	0	0	4

Table 11. Number of particle spacing counted in new quality and low porosity materials in the specimen area of 31 mm<sup>2</sup>.

particle size		New Quality			Low Porosity		
μm	log (μm)	T/10	T/4	T/2	T/10	T/4	T/2
1.26	0.100	110	84	78	82	111	67
1.96	0.293	83	57	80	69	90	63
3.07	0.487	68	76	58	60	75	64
4.79	0.680	48	60	46	49	58	36
7.47	0.873	112	110	87	102	111	81
11.66	1.07	73	75	72	83	94	75
18.20	1.26	100	71	71	108	112	86
28.40	1.45	146	90	62	96	99	64
44.33	1.65	138	91	71	100	94	75
69.18	1.84	196	113	71	171	124	59
108.0	2.03	268	194	95	250	140	100
168.5	2.23	323	205	132	286	168	92
263.0	2.42	376	238	143	281	207	126
410.5	2.61	292	223	123	242	179	101
640.8	2.81	85	69	60	84	84	58

Table 12. SEM image analysis data obtained on four 7050 materials, separating  $\text{Al}_7\text{Cu}_2\text{Fe}$  and  $\text{Mg}_2\text{Si}$  particle distributions.

	New Quality			Low Porosity		
	all	Fe	Si	all	Fe	Si
<b>area fraction</b>						
mean, %	0.304	0.187	0.090	0.551	0.379	0.118
std dev, %	0.153	0.099	0.079	0.449	0.425	0.077
no. of particles	312	138	170	339	137	199
particle density, $\text{mm}^{-2}$	259	111	137	281	111	161
<b>longest dimension</b>						
maximum, $\mu\text{m}$	31.1	25.0	31.1	44.8	44.8	28.1
mean (normal), $\mu\text{m}$	5.3	6.9	4.1	5.8	9.0	3.7
std dev (normal), $\mu\text{m}$	$\pm 4.7$	$\pm 5.0$	$\pm 4.0$	$\pm 5.6$	$\pm 6.4$	$\pm 3.6$
<b>aspect ratio</b>						
mean	0.52	0.51	0.51	0.56	0.52	0.59
std dev	$\pm 0.20$	$\pm 0.20$	$\pm 0.20$	$\pm 0.17$	$\pm 0.17$	$\pm 0.17$
<b>area</b>						
mean, $\mu\text{m}^2$	11.0	16.8	6.5	18.2	34.3	7.3
std dev, $\mu\text{m}^2$	$\pm 16.5$	$\pm 19.7$	$\pm 11.7$	$\pm 38.0$	$\pm 52.6$	$\pm 16.2$
<b>perim</b>						
mean, $\mu\text{m}$	14.6	19.3	11.0	16.4	25.5	10.3
std dev, $\mu\text{m}$	$\pm 13.1$	$\pm 14.8$	$\pm 10.2$	$\pm 17.3$	$\pm 21.5$	$\pm 9.7$

	Low Particle			Thin Plate		
	all	Fe	Si	all	Fe	Si
<b>area fraction</b>						
mean, %	0.071	0.021	0.047	0.427	0.184	0.210
std dev, %	0.057	0.016	0.050	0.111	0.085	0.054
no. of particles	198	48	150	926	206	714
particle density, $\text{mm}^{-2}$	164	38	121	768	166	577
<b>longest dimension</b>						
maximum, $\mu\text{m}$	11.8	7.4	11.8	24.5	24.5	14.0
mean (normal), $\mu\text{m}$	3.0	3.7	2.8	3.6	5.8	3.0
std dev (normal), $\mu\text{m}$	$\pm 1.8$	$\pm 1.8$	$\pm 1.8$	$\pm 2.6$	$\pm 3.5$	$\pm 1.9$
<b>aspect ratio</b>						
mean	0.60	0.55	0.61	0.53	0.45	0.55
std dev	$\pm 0.17$	$\pm 0.15$	$\pm 0.17$	$\pm 0.19$	$\pm 0.17$	$\pm 0.18$
<b>area</b>						
mean, $\mu\text{m}^2$	4.2	5.4	3.9	5.3	11.1	3.6
std dev, $\mu\text{m}^2$	$\pm 5.3$	$\pm 3.8$	$\pm 5.6$	$\pm 8.4$	$\pm 14.6$	$\pm 4.1$
<b>perim</b>						
mean, $\mu\text{m}$	8.5	10.1	7.9	9.6	15.2	8.0
std dev, $\mu\text{m}$	$\pm 4.9$	$\pm 4.7$	$\pm 4.9$	$\pm 7.0$	$\pm 10.1$	$\pm 4.6$

Table 13. Comparison of particle distributions obtained at 100X (sample area 30.9 mm<sup>2</sup>) on optical images and 250X (sample area 1.24 mm<sup>2</sup>) on SEM images.

	New Quality		Low Porosity	
	100X	250X	100X	250X
<b>area fraction</b>				
mean, %	0.99	0.30	0.98	0.55
std dev, %	0.18	0.15	0.18	0.45
<b>no. of particles</b>	5136	312	4256	339
<b>particle density, mm<sup>-2</sup></b>	166.0	258.7	137.6	281.1
<b>longest dimension</b>				
maximum, $\mu\text{m}$	90.4	31.1	108.3	44.8
mean (normal), $\mu\text{m}$	12.0	5.3	12.7	5.8
std dev (normal), $\mu\text{m}$	$\pm 7.7$	$\pm 4.7$	$\pm 9.3$	$\pm 5.6$
<b>aspect ratio</b>				
mean	0.59	0.52	0.60	0.56
std dev	$\pm 0.17$	$\pm 0.20$	$\pm 0.17$	$\pm 0.17$
<b>area</b>				
mean, $\mu\text{m}^2$	57.6	11.0	67.2	18.2
std dev, $\mu\text{m}^2$	$\pm 60.3$	$\pm 16.5$	$\pm 82.8$	$\pm 38.0$
<b>perim</b>				
mean, $\mu\text{m}$	33.9	14.6	36.1	16.4
std dev, $\mu\text{m}$	$\pm 22.2$	$\pm 13.1$	$\pm 26.7$	$\pm 17.3$



Table 14. Comparison of particle distributions obtained at 100X on transverse and longitudinal sections at the T/4 plate location in alloy 8090 variant 1 plate.

	transverse	longitudinal
<b>area fraction</b>		
mean, %	0.830	0.754
std dev, %	$\pm 0.084$	$\pm 0.094$
<b>no. of particles</b>	8336	6226
<b>number density, mm<sup>-2</sup></b>	268.5	199.8
<b>longest dimension</b>		
maximum, $\mu\text{m}$	39.70	74.81
mean (normal), $\mu\text{m}$	7.37	8.59
std dev (normal), $\mu\text{m}$	$\pm 3.55$	$\pm 5.35$
<b>aspect ratio</b>		
mean	0.706	0.646
std dev	$\pm 0.131$	$\pm 0.158$
<b>area</b>		
mean, $\mu\text{m}^2$	30.37	36.86
std dev, $\mu\text{m}^2$	$\pm 25.97$	$\pm 37.30$
<b>perim</b>		
mean, $\mu\text{m}$	21.92	24.68
std dev, $\mu\text{m}$	$\pm 9.82$	$\pm 13.99$

Table 15. Intensities for components of texture in alloy 8090 variant 1 plate.

comp.		euler angles [deg]			intensity	
		$\psi$	$\theta$	$\phi$	max	interpolated
cube	{001}<001>	10.0	0.0	0.0	1.67	1.67
goss	{011}<112>	90.0	45.0	0.0	1.49	1.59
brass	{110}<112>	64.9	45.0	0.0	1.55	1.71
2		54.9	24.4	10.0	2.11	2.38
3		40.1	24.7	20.0	2.38	2.50
4		15.0	25.2	30.0	3.22	3.16
5		7.5	25.4	40.0	4.16	3.97
copper	{112}<111>	0.0	29.6	45.0	4.29	4.20

Table 16. Results of tensile tests in L and LT orientations for alloy 8090 variant 1 plate.

	TYE			R&N					
	YS ksi	UTS ksi	e <sub>t</sub> %	YS ksi	UTS ksi	e <sub>u</sub> %	e <sub>t</sub> %	k	n
L	59.2	68.6	3.2	59.8	68.7	2.63	2.63	88.3	0.067
	60.3	70.2	3.2	60.4	69.6	2.68	2.76	89.1	0.068
ave	<b>59.8</b>	<b>69.4</b>	<b>3.2</b>	<b>60.1</b>	<b>69.2</b>	<b>2.65</b>	<b>2.69</b>	<b>88.7</b>	<b>0.068</b>
LT	53.4	67.8	4.7	54.3	66.7	1.99	2.09	92.4	0.086
	53.4	66.3	3.6	53.7	65.7	1.76	1.76	92.2	0.087
ave	<b>53.4</b>	<b>67.0</b>	<b>4.2</b>	<b>54.0</b>	<b>66.2</b>	<b>1.87</b>	<b>1.93</b>	<b>92.3</b>	<b>0.087</b>

Table 17. Smooth axial stress fatigue lifetimes for alloy 8090 variant 1 plate tested at R=0.1, frequency = 30 Hz, in laboratory air.

Longitudinal Orientation		Transverse Orientation	
Maximum Stress (ksi)	Lifetime (cycles)	Maximum Stress (ksi)	Lifetime (cycles)
45	108,883	45	44,539
45	87,854	45	35,079
45	83,116	45	67,313
45	76,740	45	41,018
45	96,481	45	15,866
40	200,282	40	116,049
40	215,341	40	79,656
40	217,255	40	138,073
40	236,836	40	77,588
40	196,054	40	62,333
35	479,473	35	342,705
35	365,679	35	358,575
35	381,585	35	103,618
35	331,307	35	976,533
35	456,746	35	956,127
30	2,587,541	30	736,300
30	10,035,853*	30	10,000,000*
30	10,640,822*	30	1,464,968
30	2,273,812	30	16,907,596*
30	11,582,124*	30	10,316,368*

\*Specimen did not fail.

Table 18. Open hole fatigue lifetimes for alloy 8090 variant 1 plate tested at R=0.1, frequency = 30 Hz, in laboratory air.

Longitudinal Orientation		Transverse Orientation	
Maximum Stress (ksi)	Lifetime (cycles)	Maximum Stress (ksi)	Lifetime (cycles)
30	38,150	30	35,080
30	47,050	30	35,830
30	37,110	30	44,690
30	49,790	30	31,340
30	49,860	30	787,930
		30	30,780
25	141,340	25	529,620
25	256,740	25	675,890
25	272,060	25	524,630
25	185,600	25	118,430
25	324,060	25	106,920
		25	601,590
		25	6,469,560
22.5	358,120	22.5	310,170
22.5	984,310	22.5	1,857,520
22.5	1,219,890	22.5	1,228,630
22.5	1,053,300	22.5	10,358,580
22.5	756,160	22.5	5,433,430
20	5,697,990	20	3,421,200
20	1,286,790	20	14,887,840*
20	1,078,970	20	14,481,250*
20	4,528,340	20	5,545,310
20	14,492,110*	20	6,935,400
		20	13,466,970*

\*Specimen did not fail.

Table 19. Comparison of the calculated material fatigue strengths and improvements in open hole fatigue for 7050 plate materials.

Material	Fatigue Stress at $10^5$ cycles (MPa)	% Improvement	Failure Mechanism
Old Quality Plate	110	—	Microporosity
New Quality Plate	125	14%	Microporosity
Low Porosity Plate	125	14%	Constituent Particles
Low Particle Plate	150	36%	Micropores/ Constituent Particles

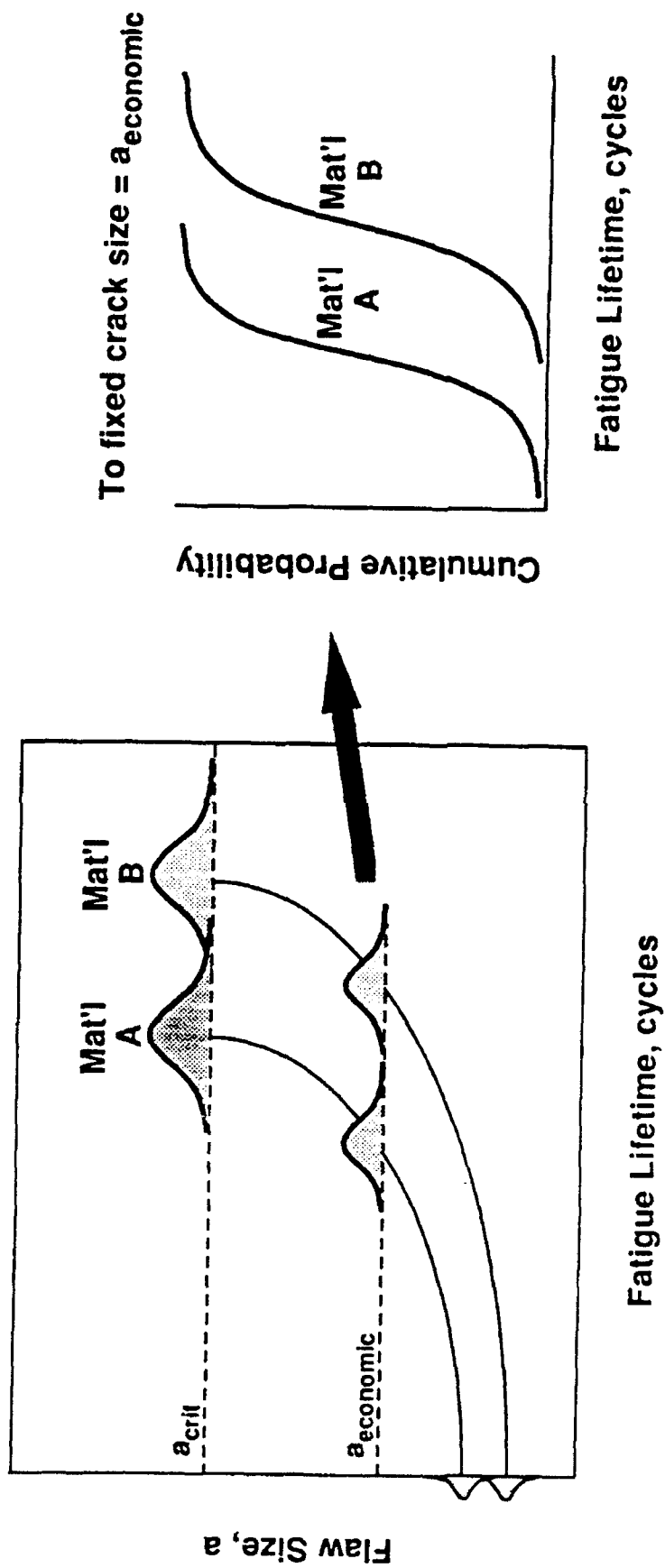


Figure 1a. Schematic representation of the cumulative lifetime distribution to a fixed flaw size for two materials with different intrinsic defect populations.

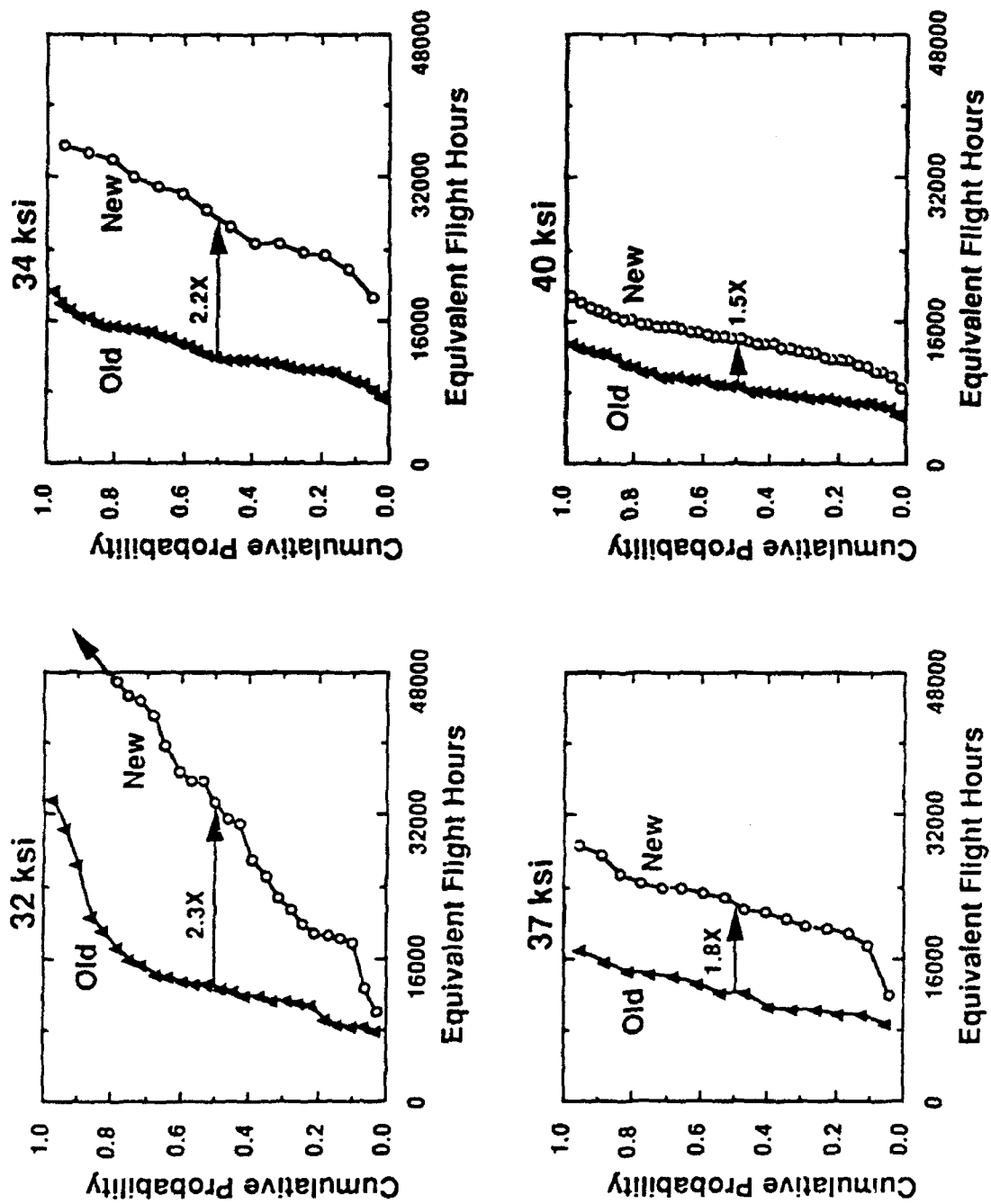


Figure 1b. Effect of 7050-T7451 thick plate quality on cumulative life probability to 0.05 in flaw, T/2 specimen location, LT orientation, F-16 400 hr. lower wing spectrum loading, spectrum peak stresses of 32, 34, 37 and 40 ksi. Test results courtesy of USAF [3].



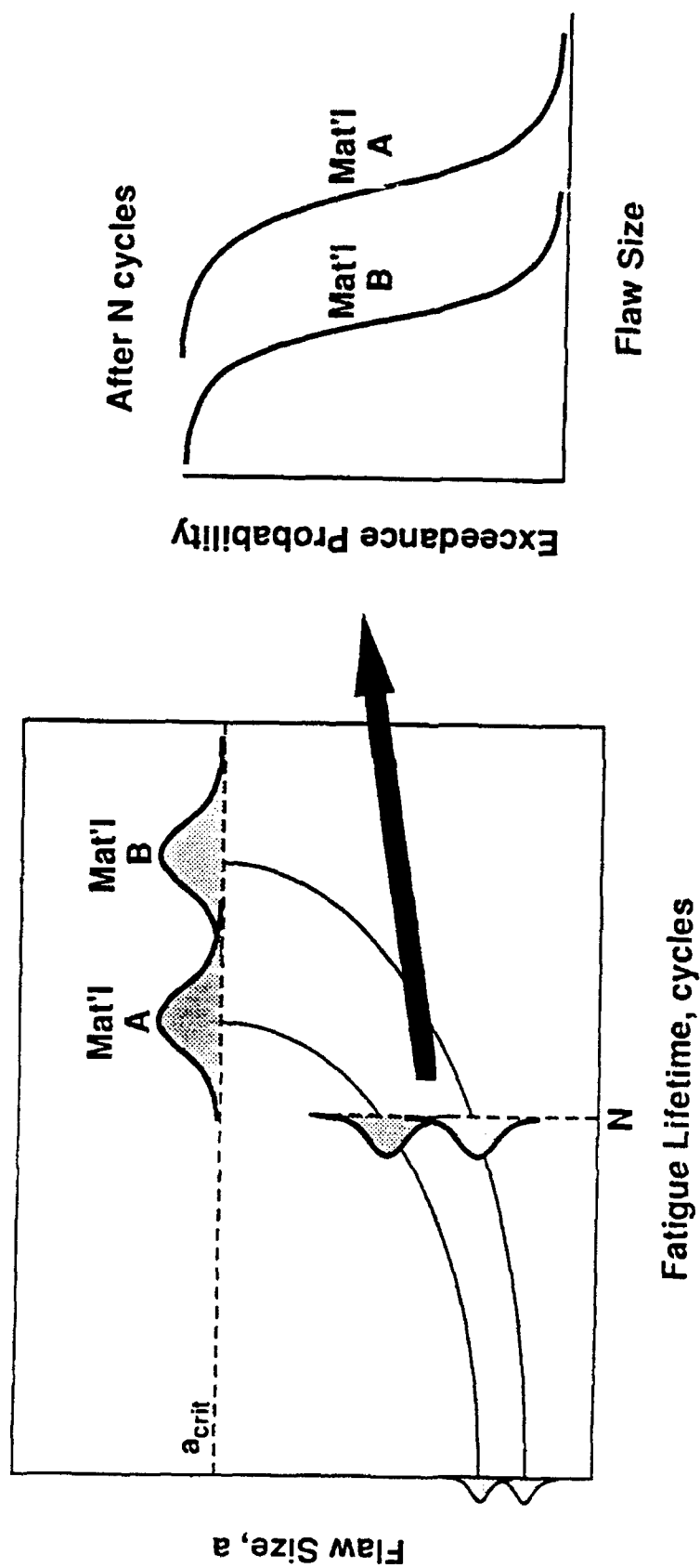


Figure 2a. Schematic representation of the flaw exceedance probabilities after a fixed lifetime for two materials with different intrinsic defect populations.

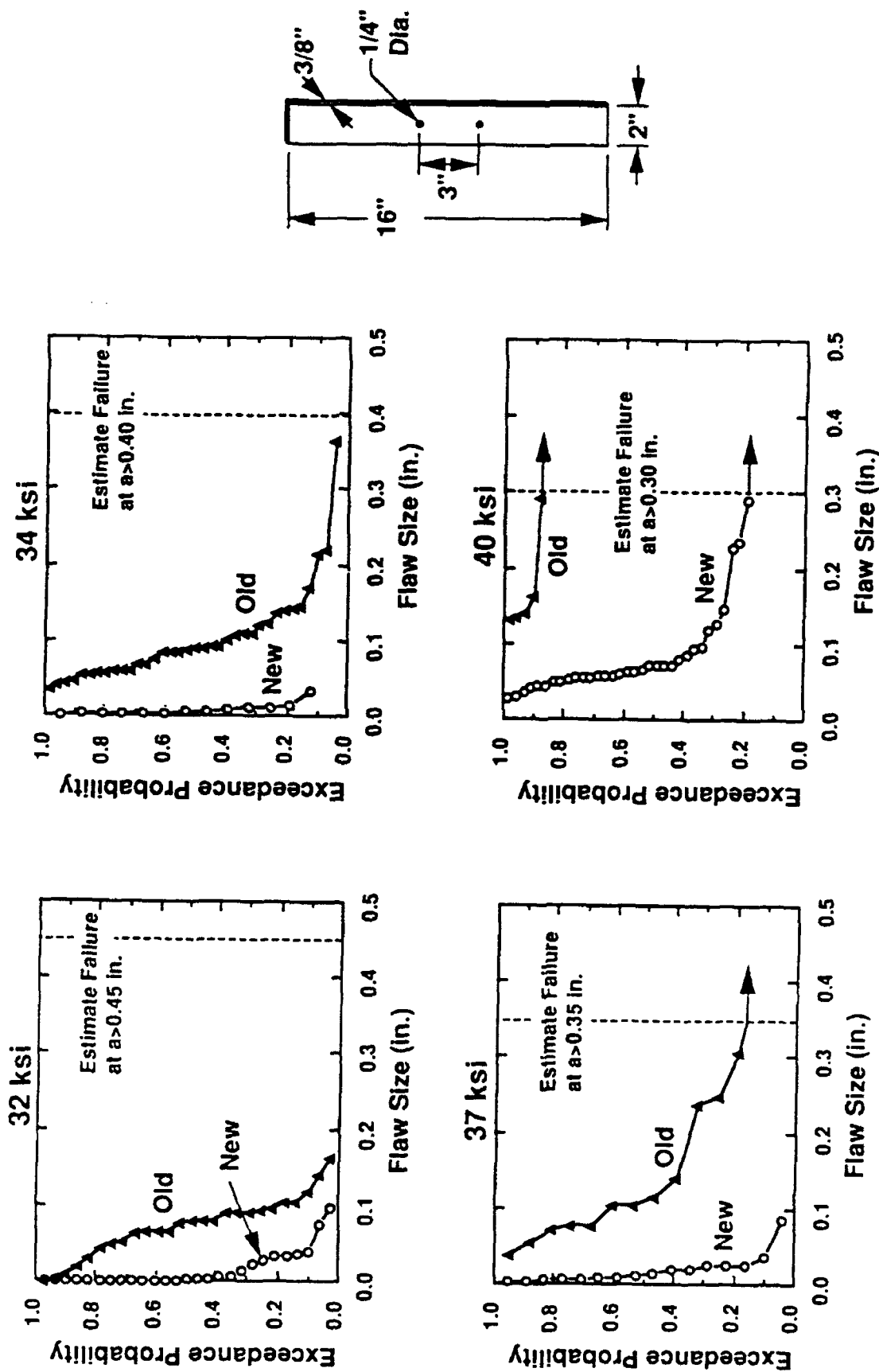


Figure 2b. Effect of 7050-T7451 thick plate quality on flaw size exceedance probabilities, T/2 specimen location, LT orientation, F-16 400 hr. lower wing spectrum loading, 16000 hrs. at spectrum peak stresses of 32, 34, 37, and 40 ksi. Test results courtesy of USAF [3].

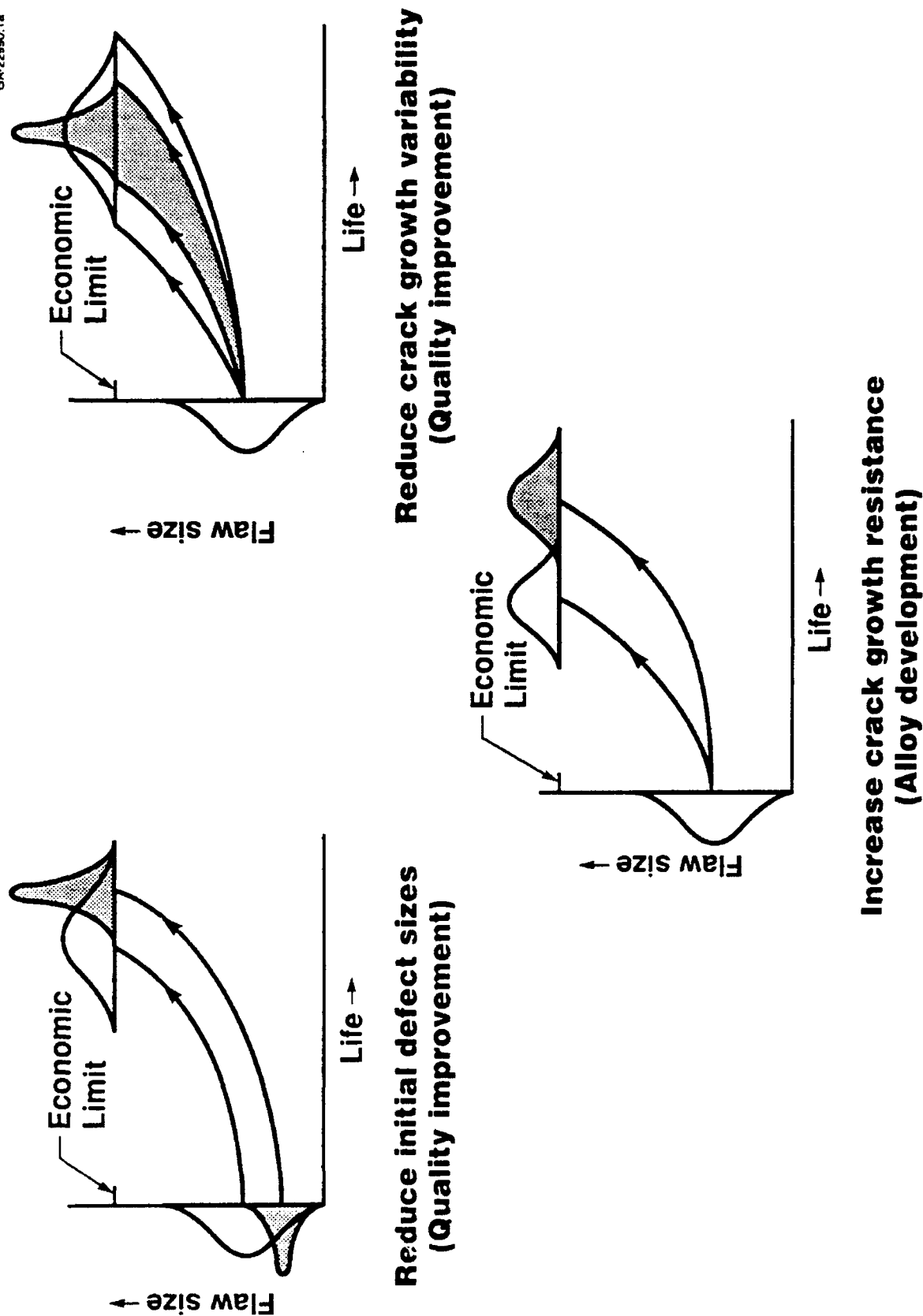


Figure 3. Materials and processing approaches to improving structural durability.

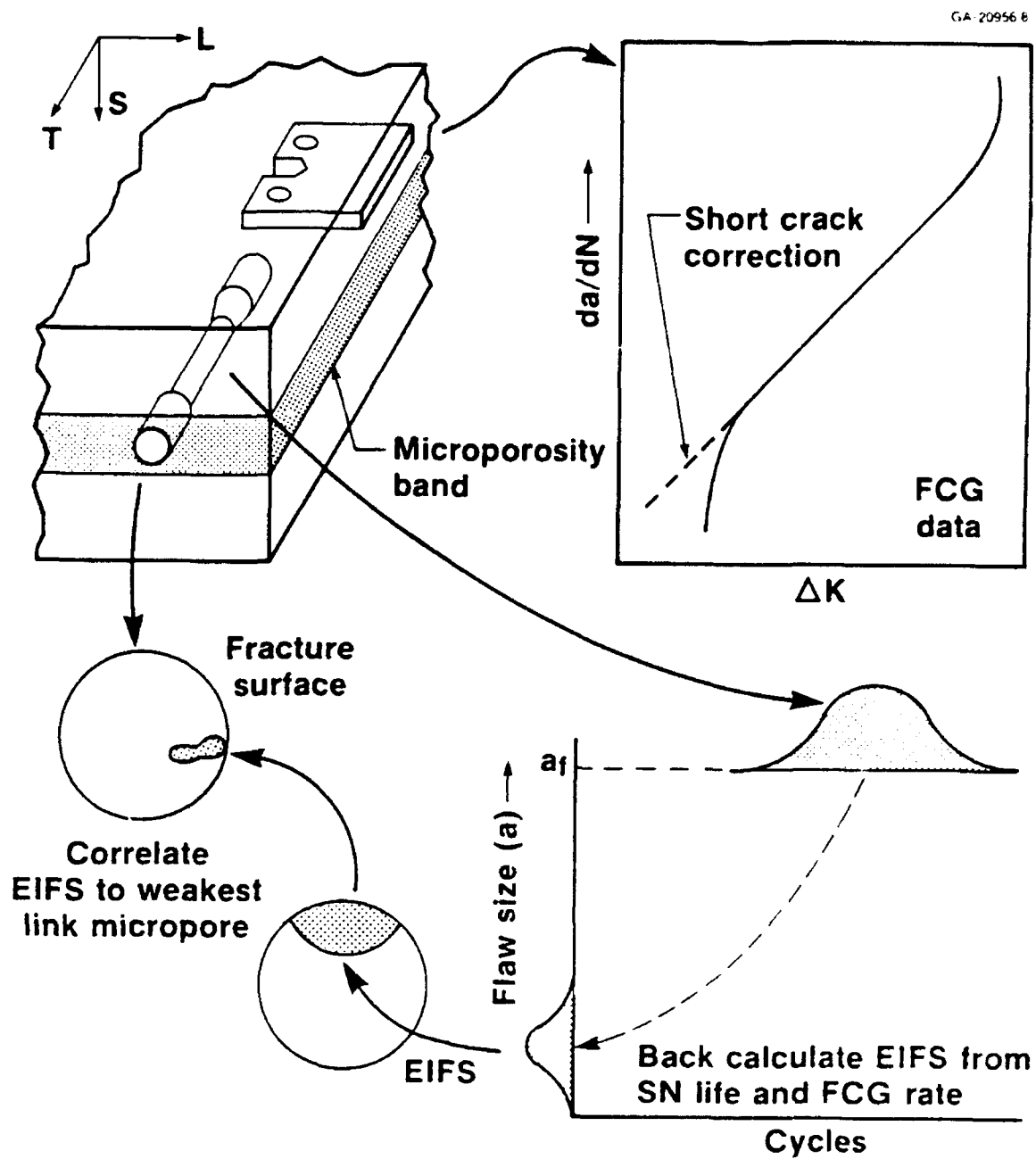


Figure 4. Analytical approach to obtaining material EIFS distribution.

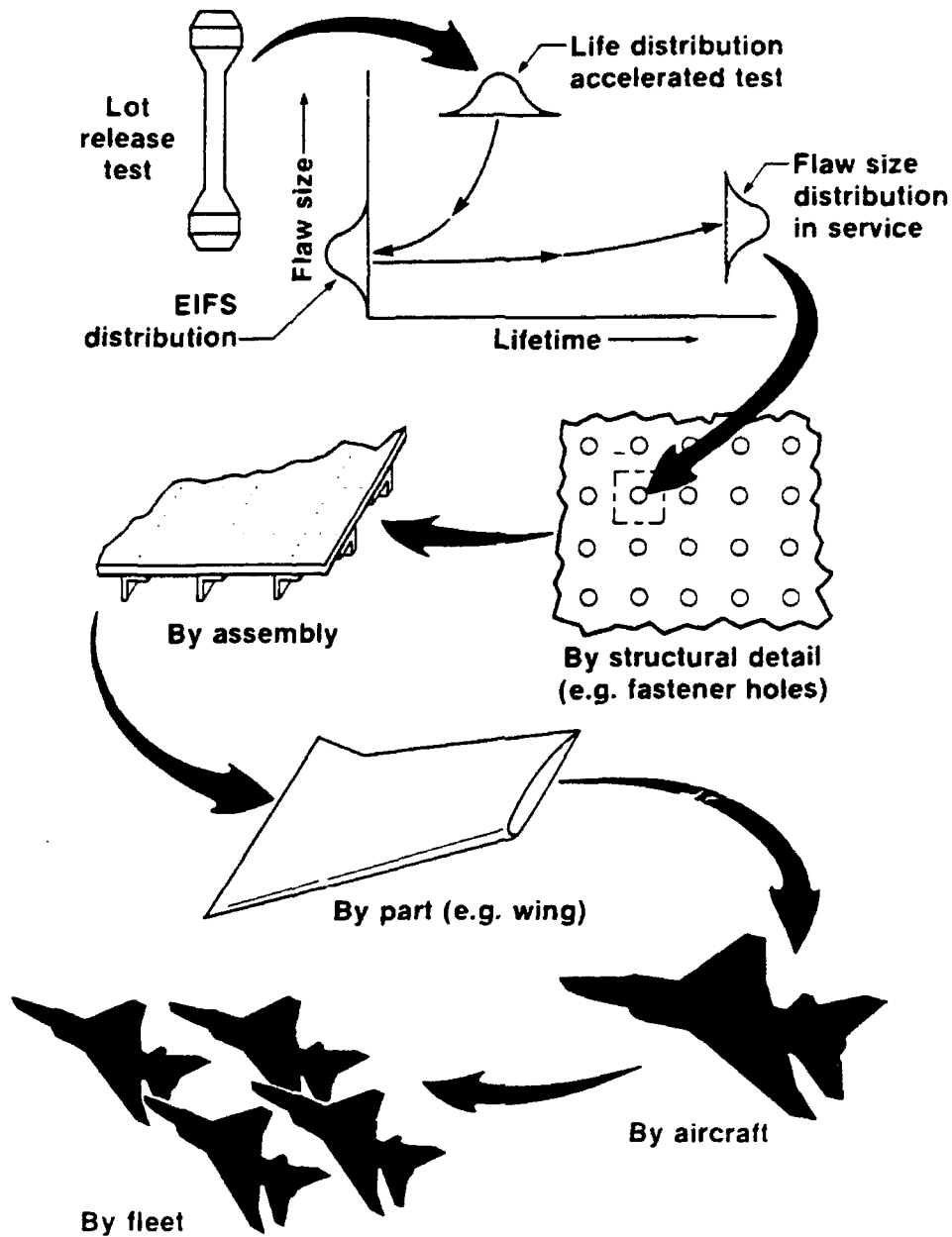
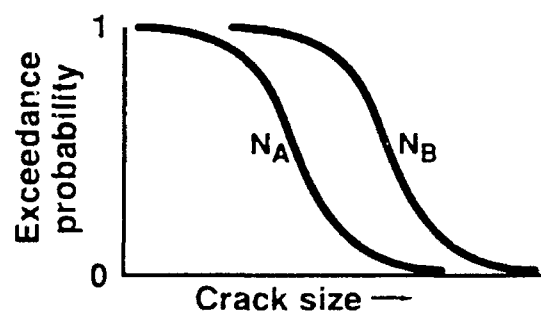
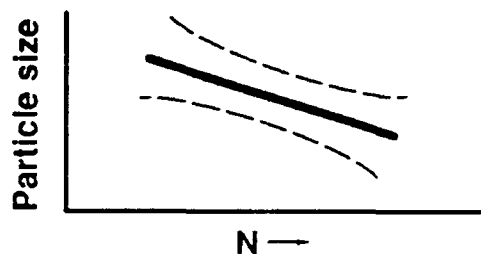
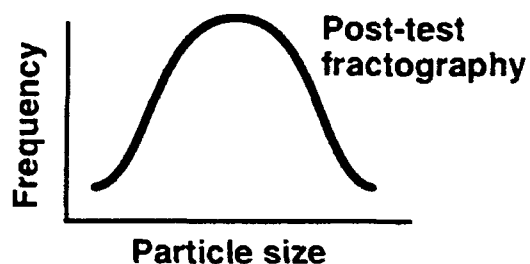
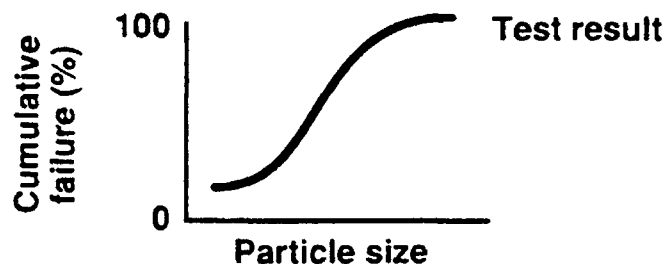
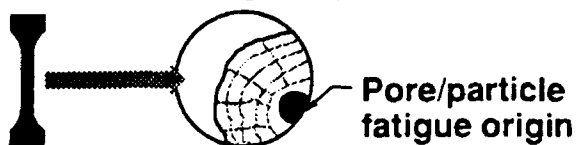


Figure 5. The use of EIFS distribution in life management at various structural levels.

## Coupon Tests

Test coupon + fractography



## Microanalysis

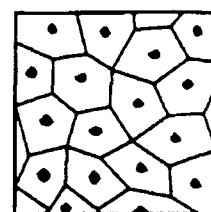
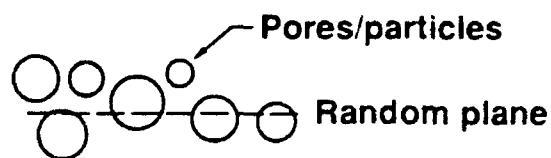
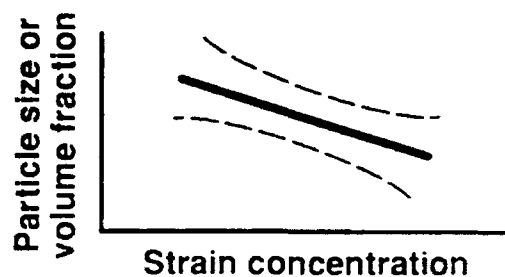
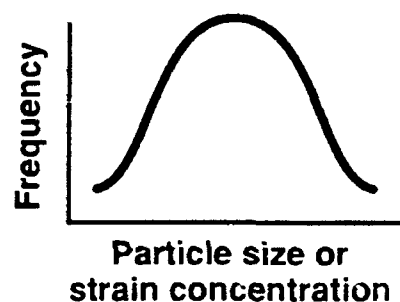


Image analysis  
+  
Tessellation  
+  
Finite element



## Interrupted Tests

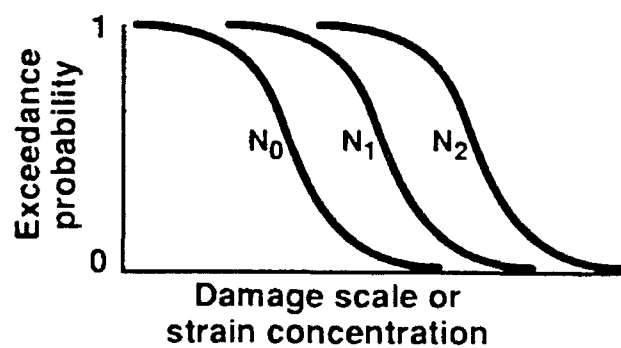


Figure 6. Corresponding linkages between test information and microanalysis.

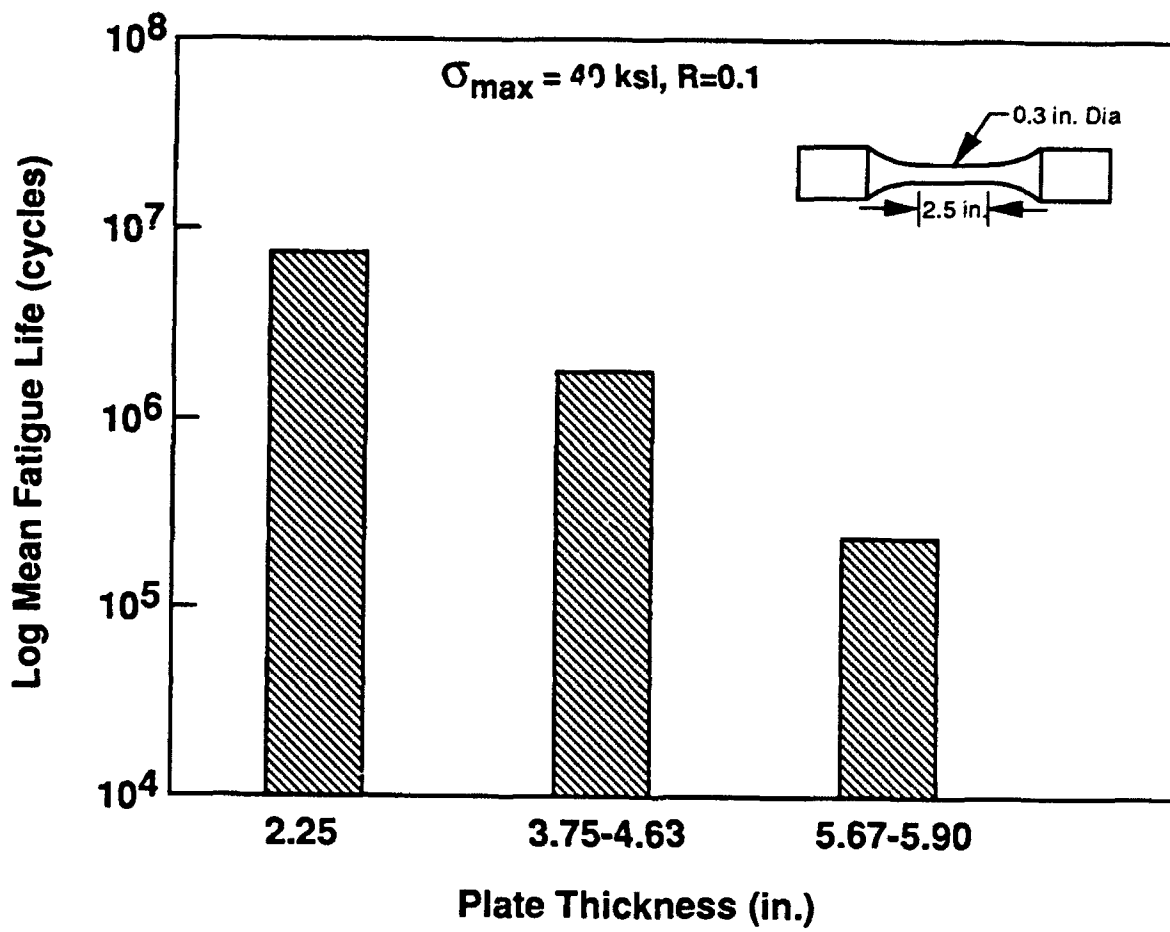


Figure 7. Historical data showing the effect of 7050 alloy plate thickness on smooth axial specimen fatigue lifetime.

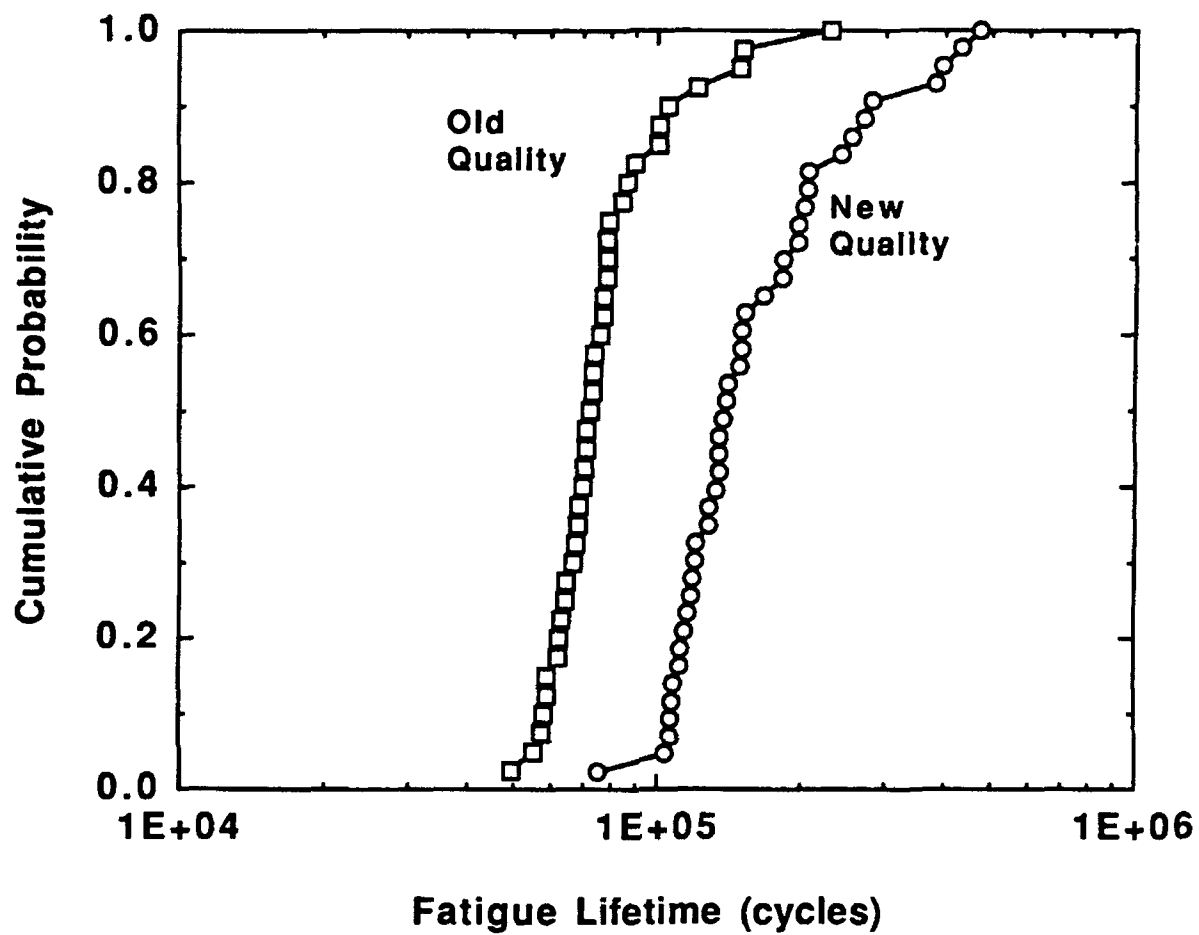


Figure 8. Cumulative smooth fatigue lifetime distributions for old and new quality plate. Tests conducted at 35 ksi max. stress,  $R=0.1$ , 10 Hz, LT orientation, lab air.



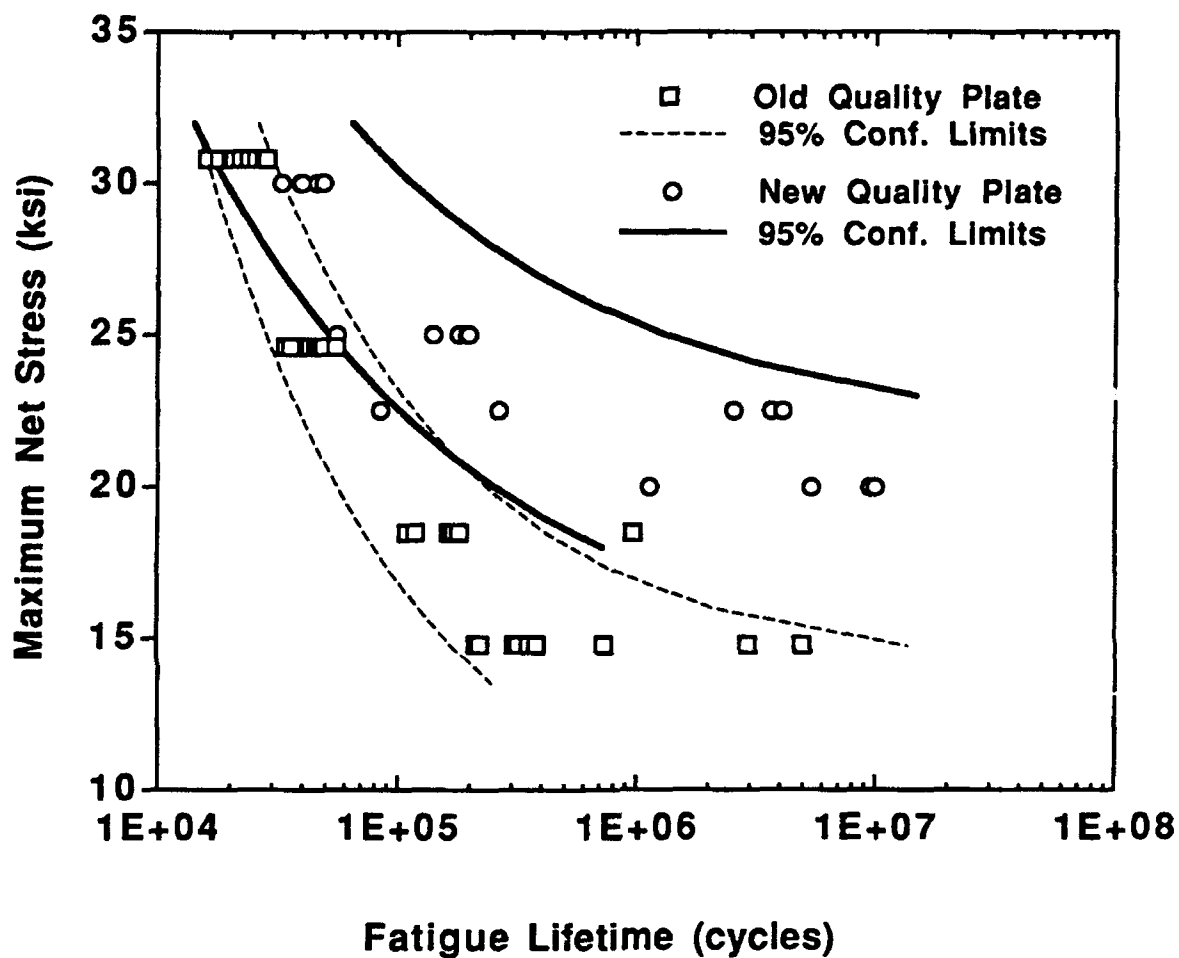


Figure 9. Open hole fatigue lifetimes for new and old quality plate. Tests conducted at  $R=0.1$ , 30 Hz, LT orientation, lab air.

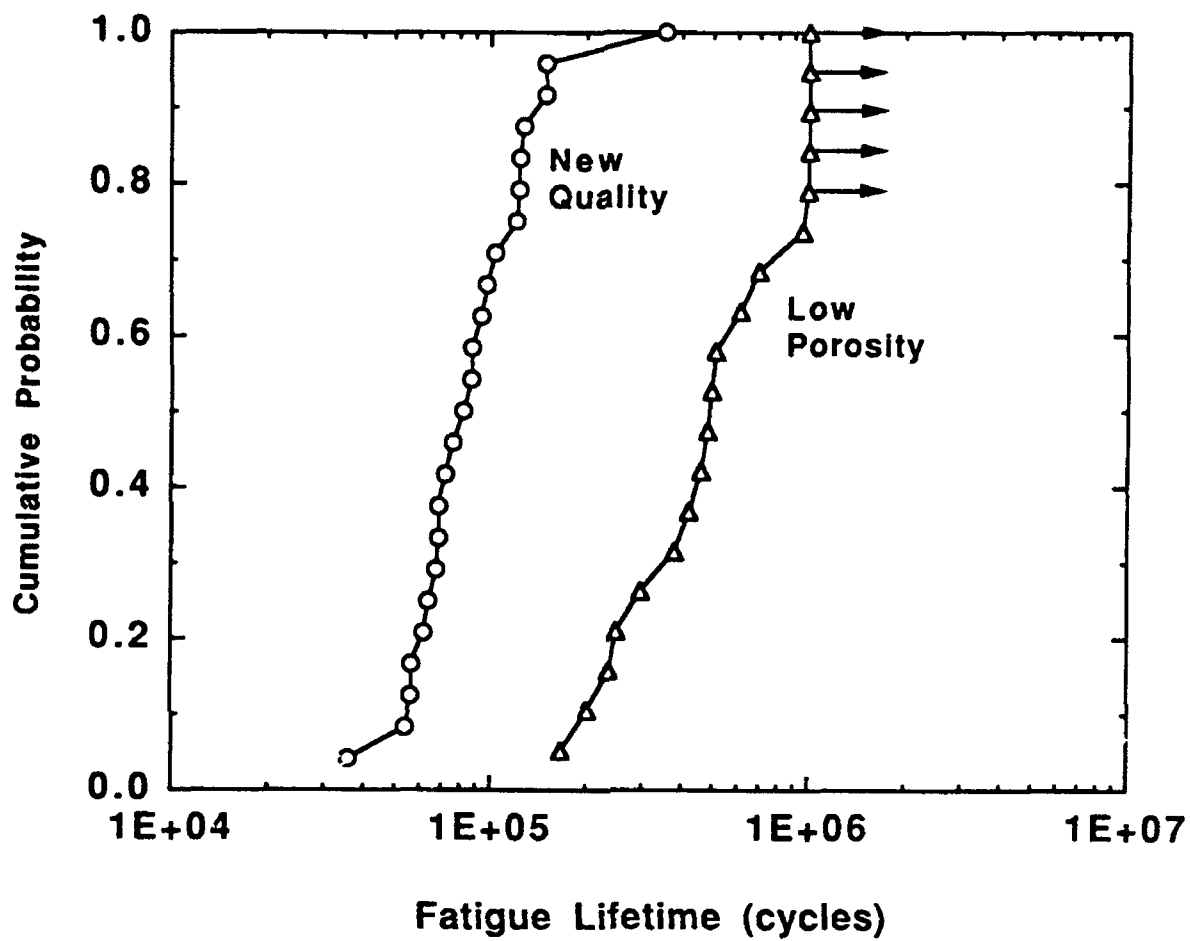


Figure 10. Cumulative smooth fatigue life distributions for new quality and low porosity thick plate. Tests performed at 40 ksi max. stress,  $R=0.1$ , 10 Hz, LT orientation, laboratory air.

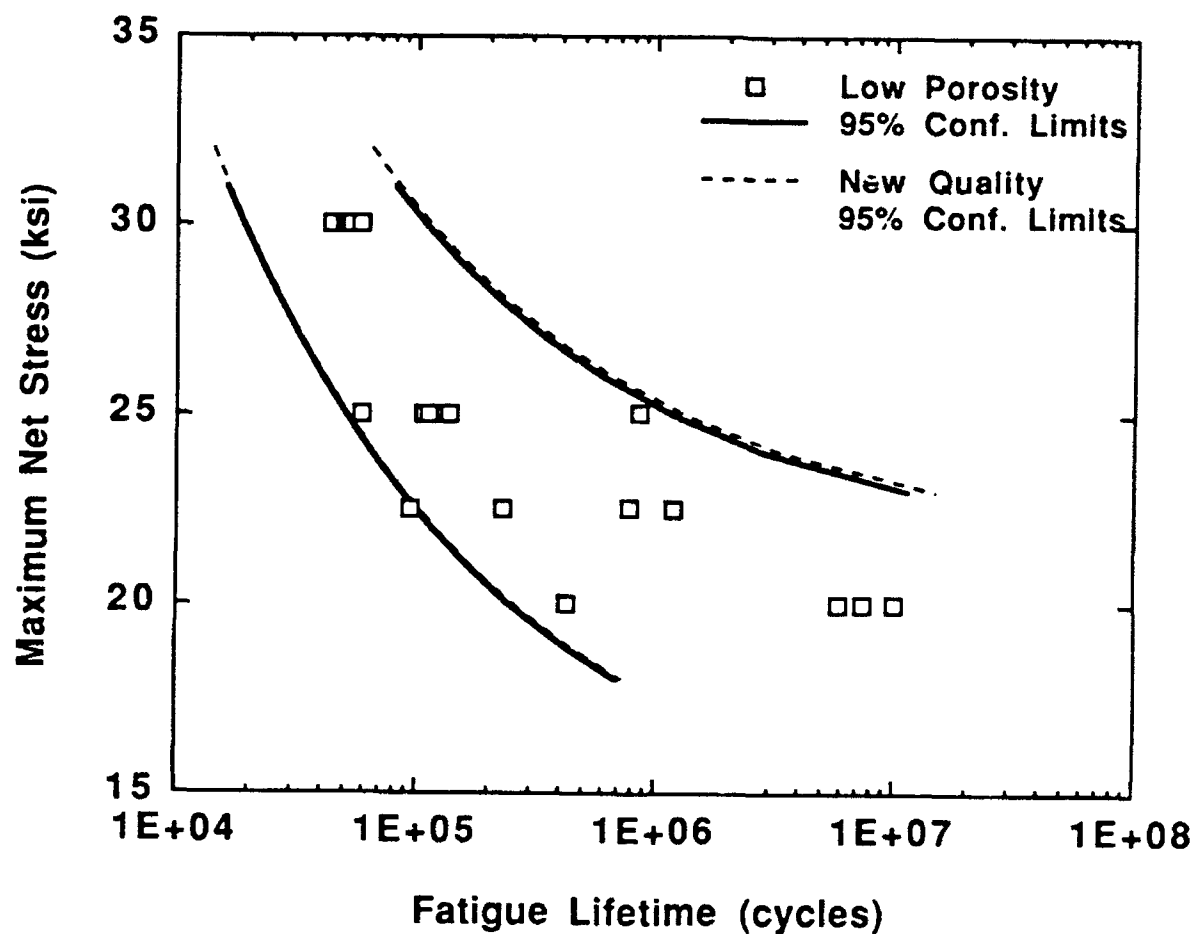


Figure 11. Open hole fatigue lifetimes for low porosity plate along with 95% confidence limits for new quality plate. Tests conducted at  $R=0.1$ , 30 Hz, LT orientation, lab air.

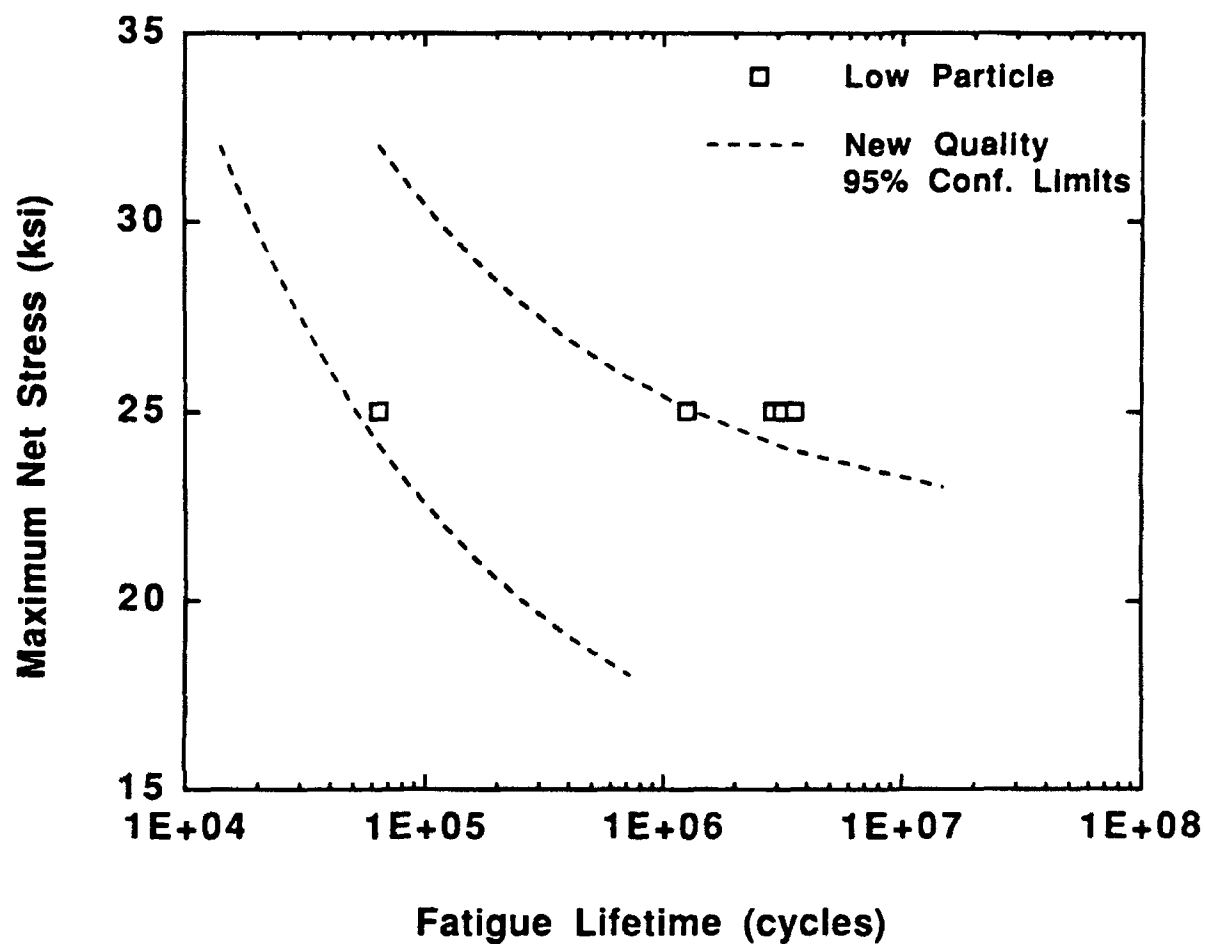


Figure 12. Open hole fatigue lifetimes for low particle plate and the 95% confidence limits for new quality plate. Tests conducted at  $R=0.1$ , 30 Hz, LT orientation, lab air.

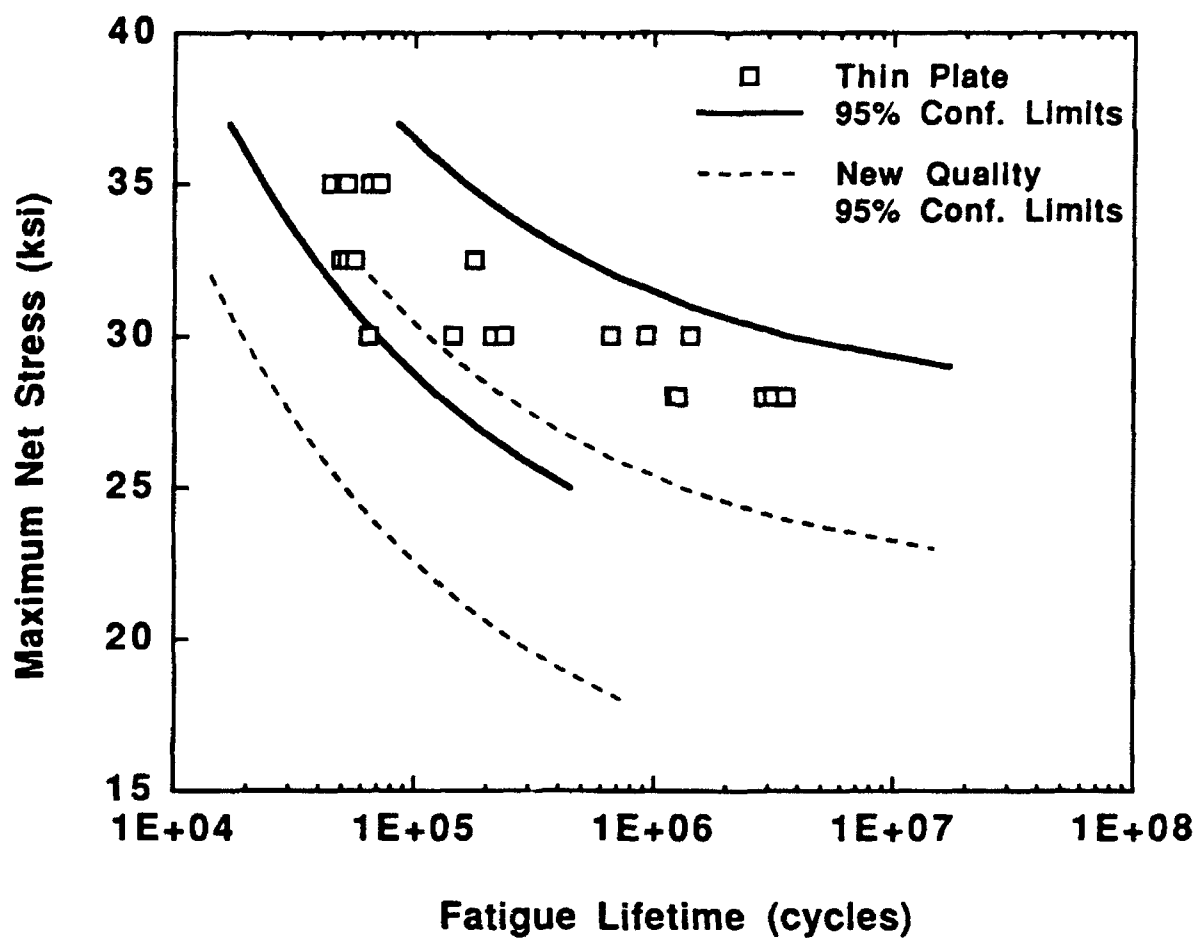


Figure 13. Open hole fatigue lifetimes for thin plate and 95% confidence limits for new quality plate. Tests conducted at  $R=0.1$ , 30 Hz, LT orientation, lab air.

(a)



(b)

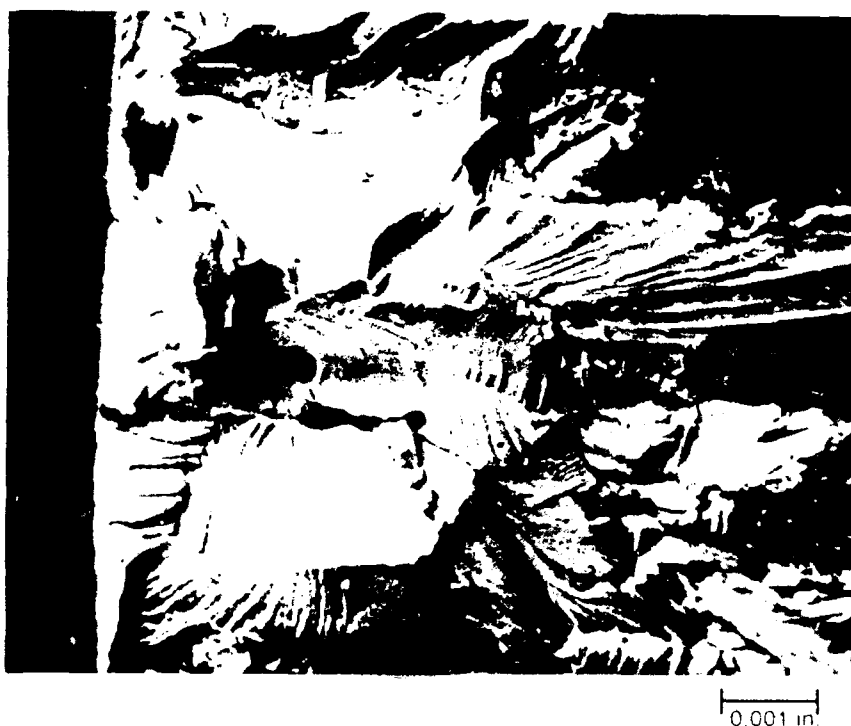


Figure 14. Typical smooth fatigue crack initiation from micropores in 7050 plate. (a) Old quality plate, micropore length = 0.0069 in. (b) New quality plate, micropore length = 0.0027 in.

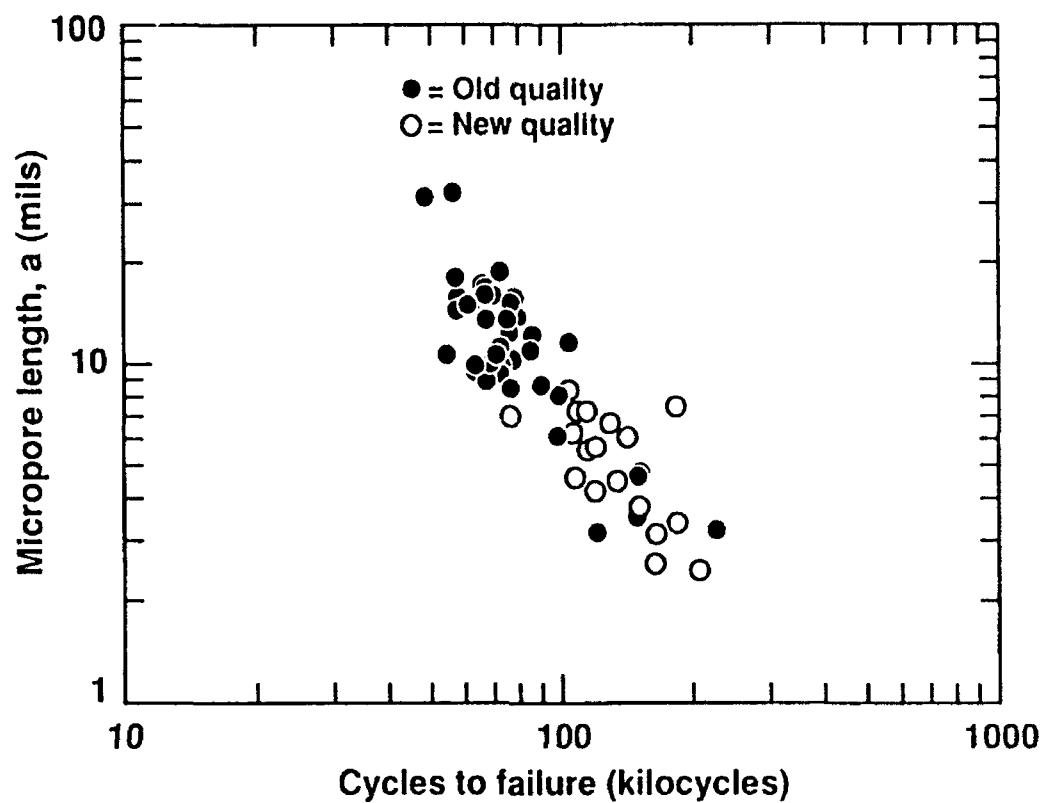


Figure 15. Crack initiating micropore length versus cycles to failure in smooth fatigue specimens of old and new quality 7050 plate tested at 35 ksi maximum stress,  $R=0.1$ , 10 Hz, in laboratory air.



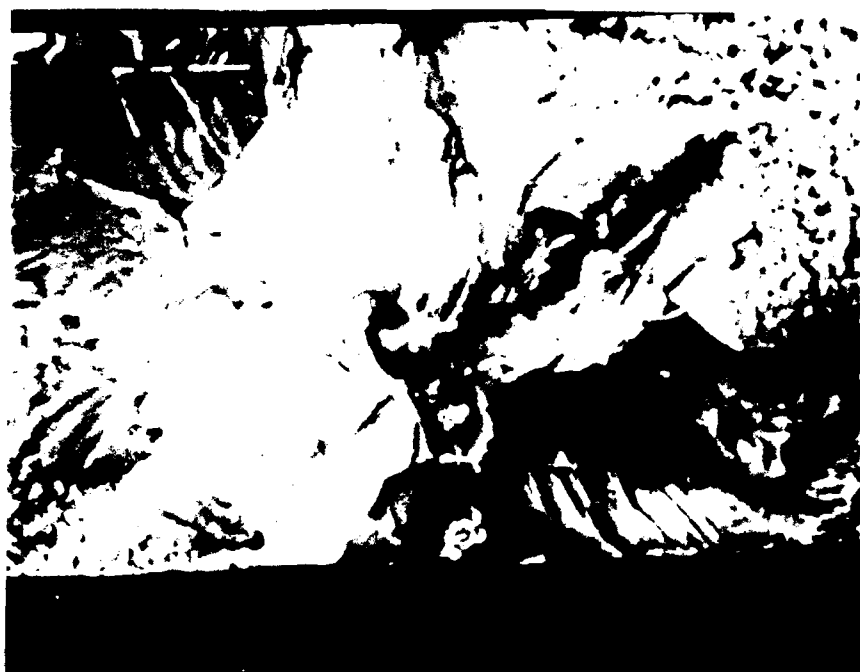
Figure 16. Fatigue initiation in open hole specimen from micropore in old quality 7050 plate, micropore size = 0.011 in.





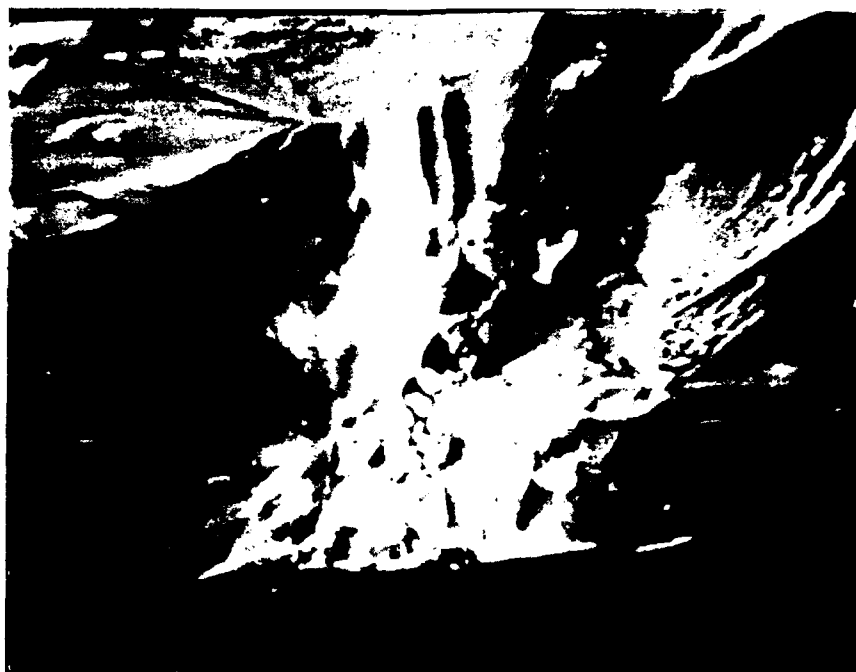
Figure 17. Fatigue initiation in open hole specimen from micropore in new quality 7050 plate, micropore size = 0.0044 in.

(a)



0.001 in.

(b)



0.001 in.

Figure 18. Typical smooth fatigue crack initiation sites in low porosity 7050 plate (a) from a microvoid and (b) from constituent particles.



Figure 19. Fatigue initiation in open hole specimen from constituent particle located at the hole corner in low porosity 7050 plate, constituent particle size = 0.0019 in.

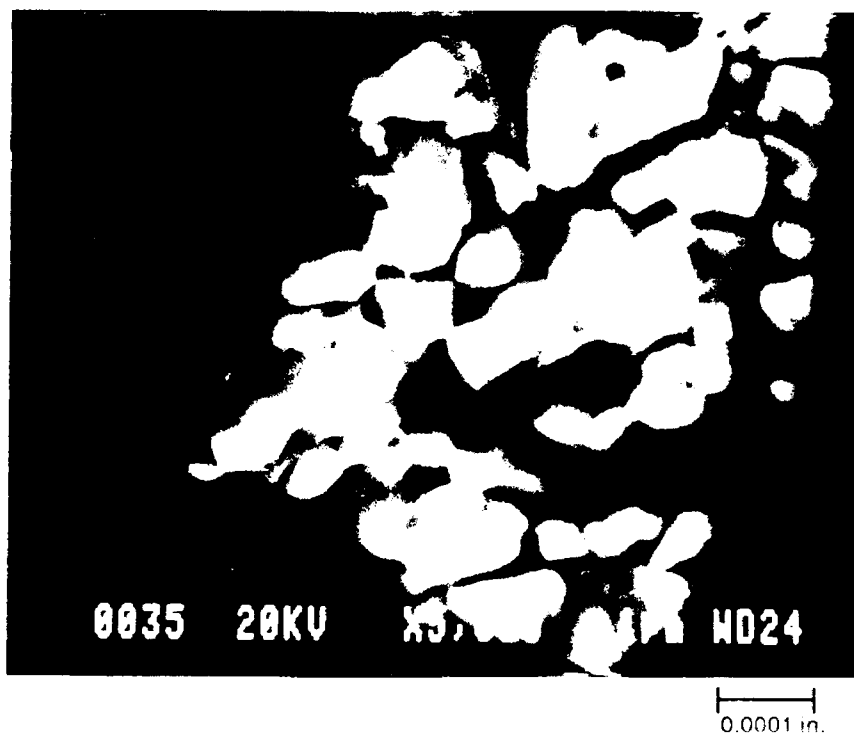
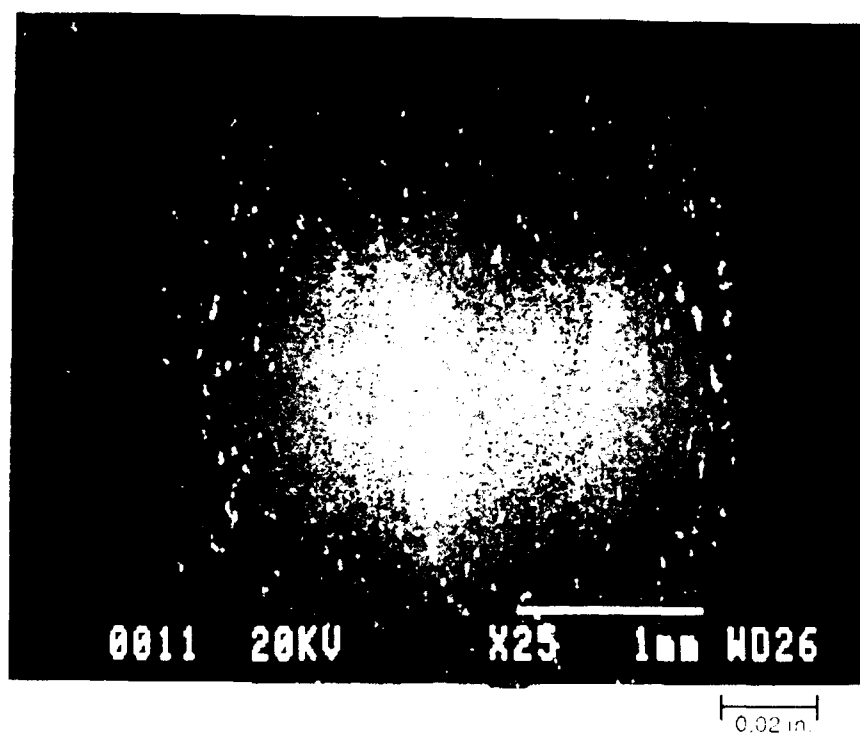


Figure 20. Opposite halves of open hole fatigue failure showing constituent particle at fatigue initiation site in low porosity 7050 thick plate.

(a)



(b)

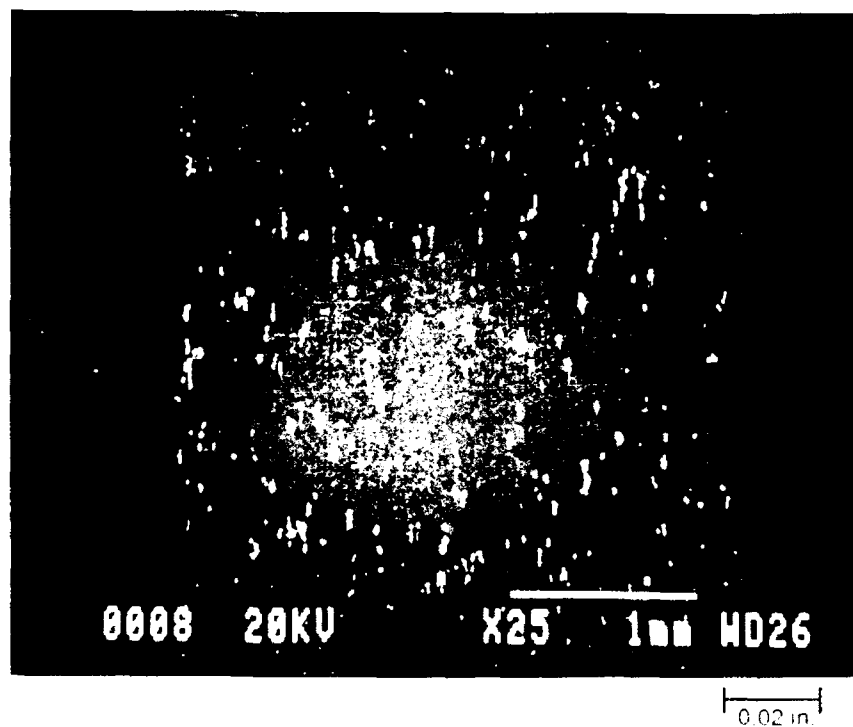


Figure 21. Low magnification SEM images showing constituent particles located in the hole bore in open hole specimens in (a) new quality plate and (b) low porosity plate.



0.0005 in



0.0001 in

Figure 22. Constituent particles located in the hole bore of open hole specimens of low porosity plate.

(a)



(b)



Figure 23. Fatigue crack initiation in open hole specimens from constituent particles in thin plate. (a) Constituent particle size = 0.00097 in. and (b) constituent particle size = 0.0009 in

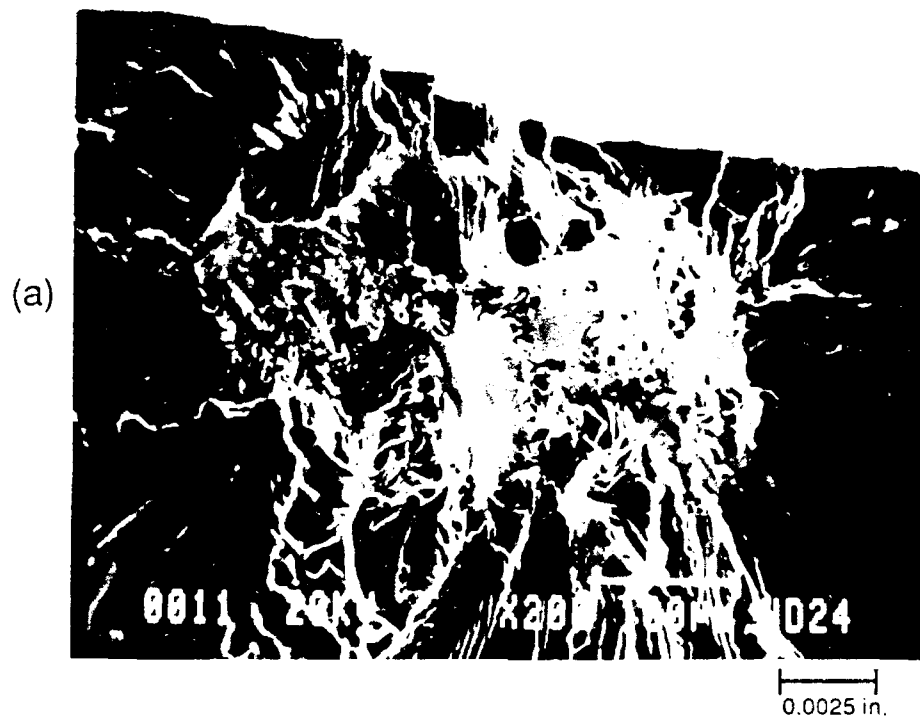


Figure 24. Fatigue crack initiation in open hole specimens Showing stage I type initiation in (a) low particle plate and (b) thin plate.



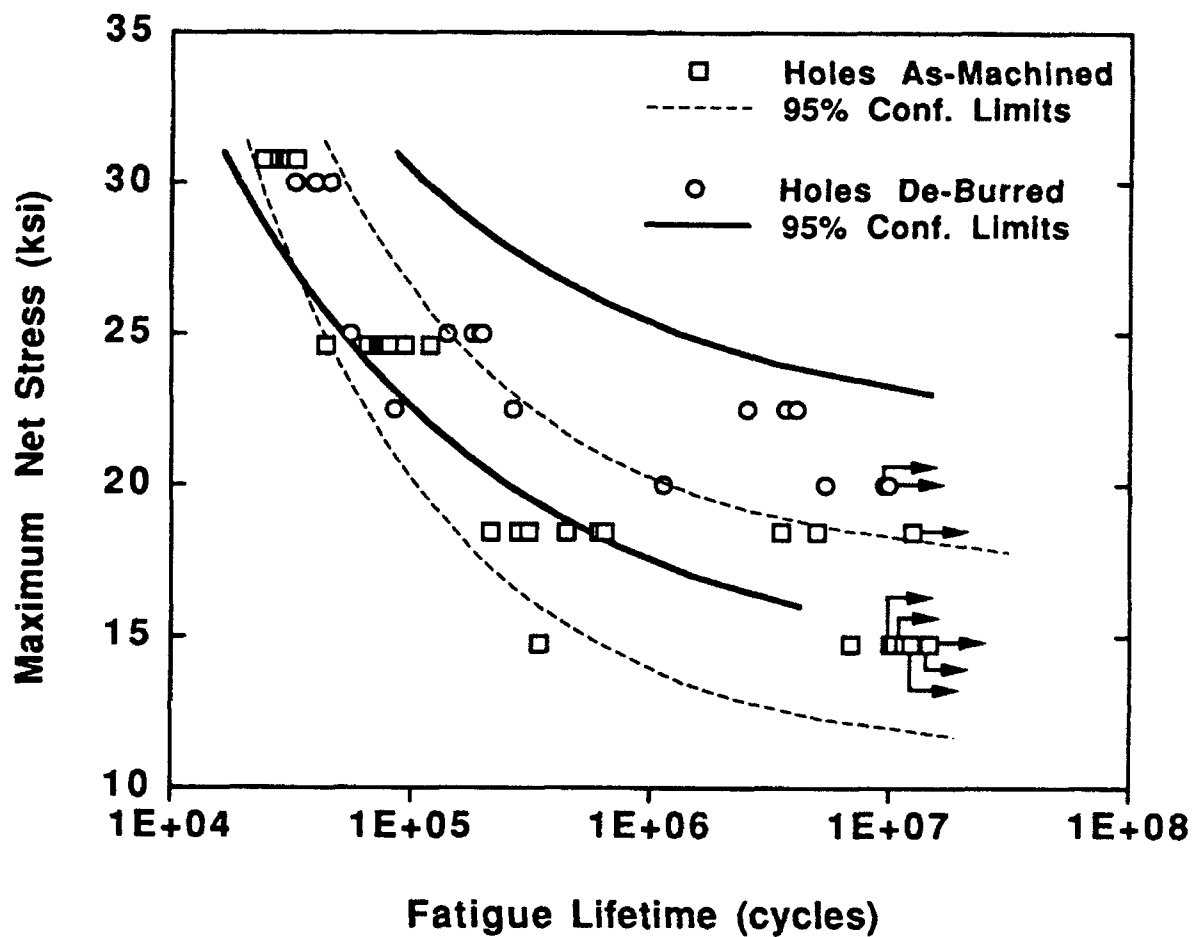


Figure 25. Comparison of the new quality plate open hole fatigue lifetimes for specimens with holes as-machined and holes de-burred. Tests conducted at  $R=0.1$ , 30 Hz, LT orientation, Lab Air.



Figure 26. Fatigue initiation in open hole specimen from hole edge burr in new quality 7050 plate for specimen which was not de-burred.

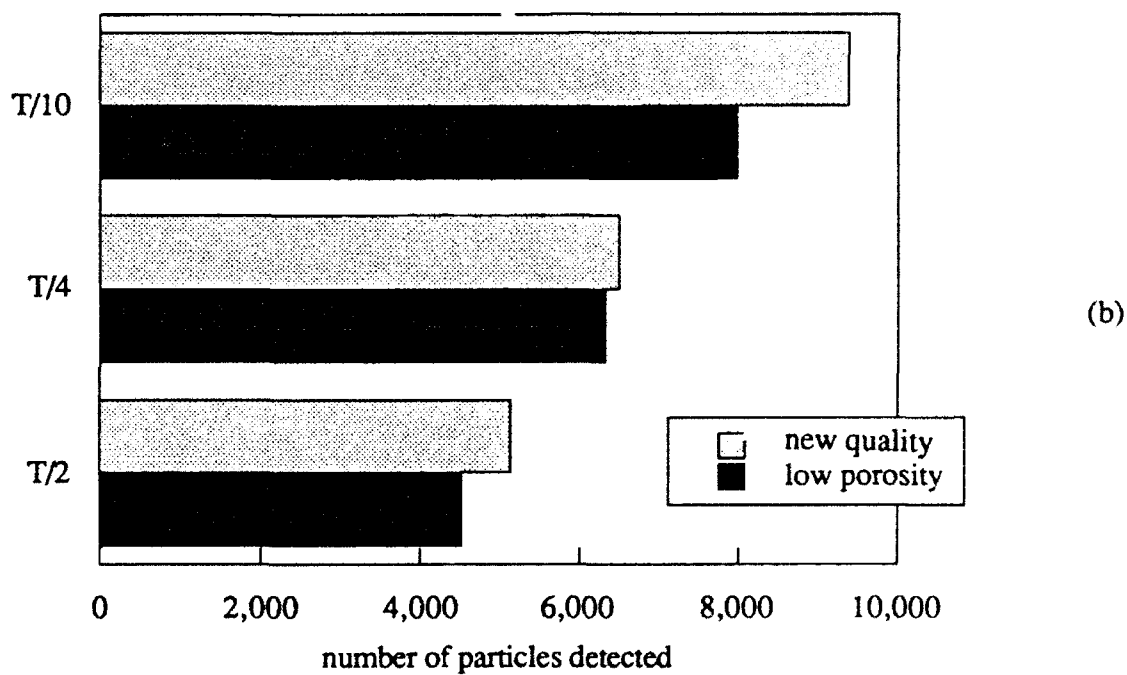
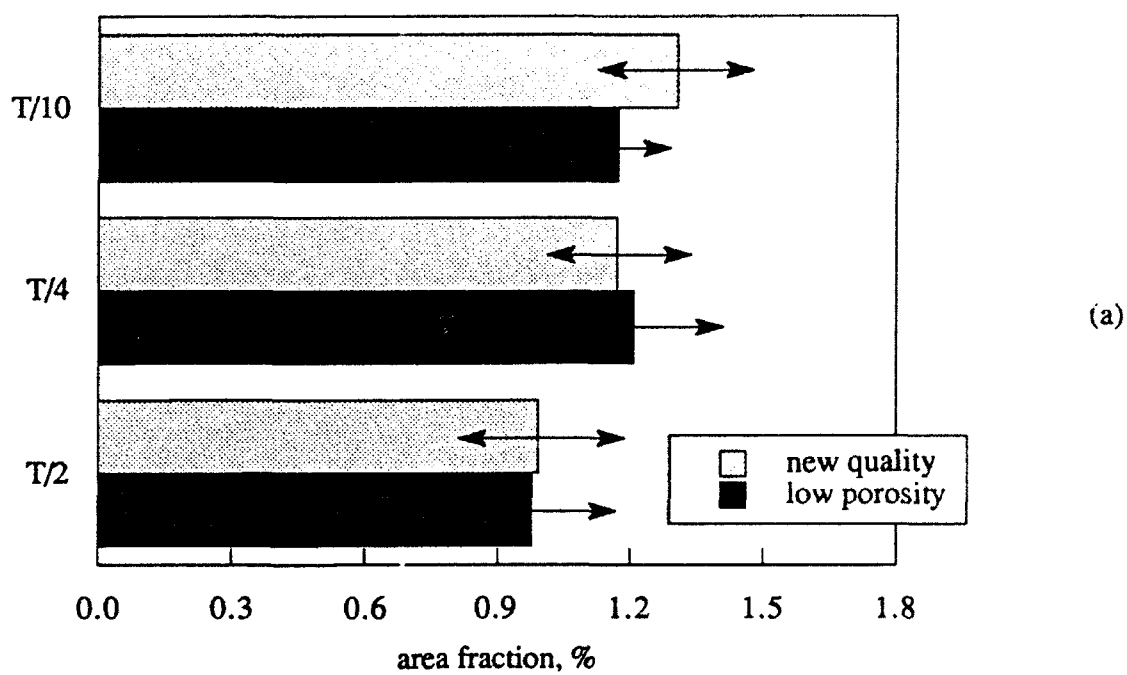


Figure 27. Graphs showing the effect of processing path on (a) particle area fraction, and (b) particle number density at different plate locations.

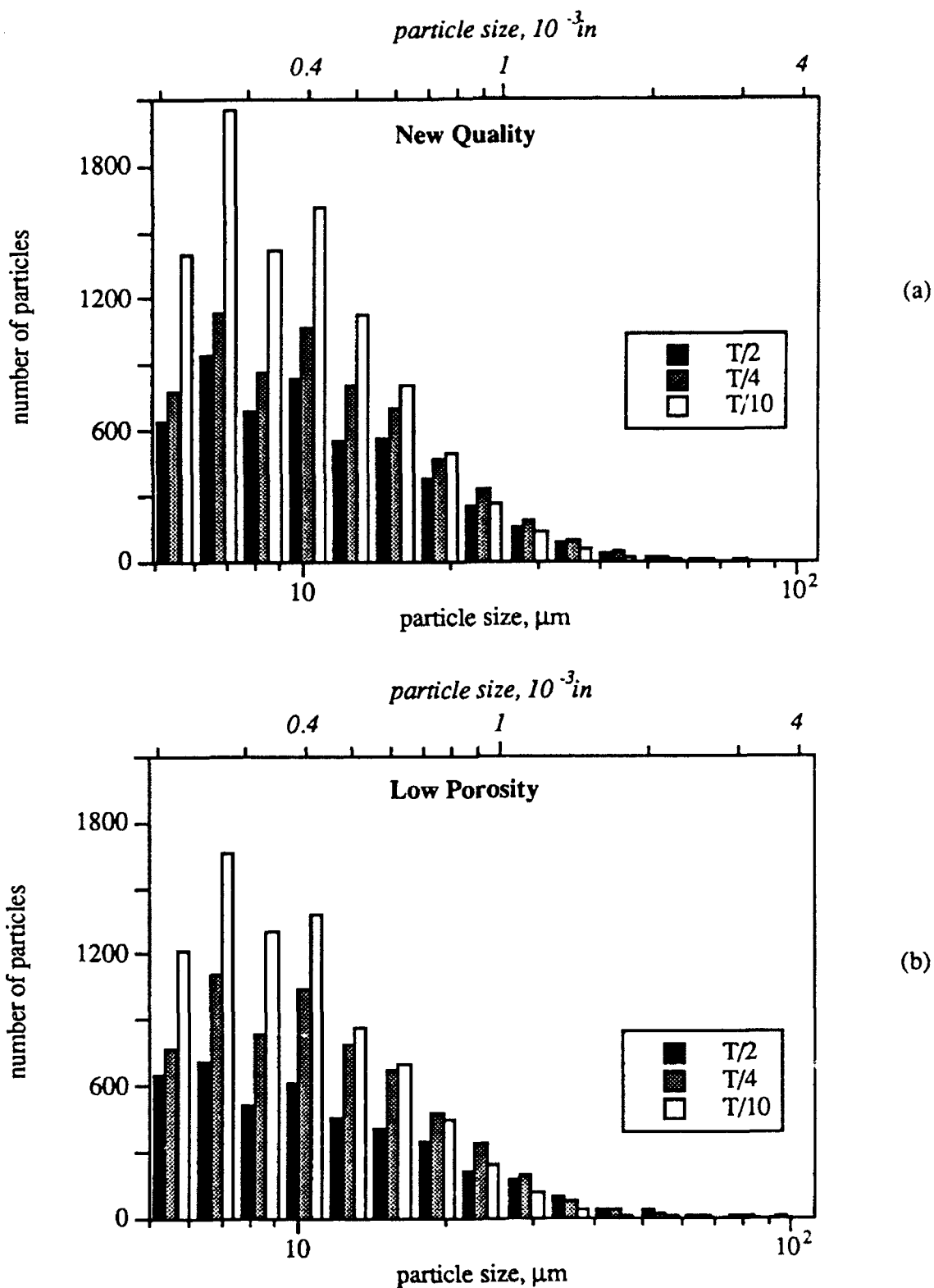


Figure 28. Histograms of particle size on a logarithmic scale for (a) new quality and (b) low porosity materials at different plate locations.

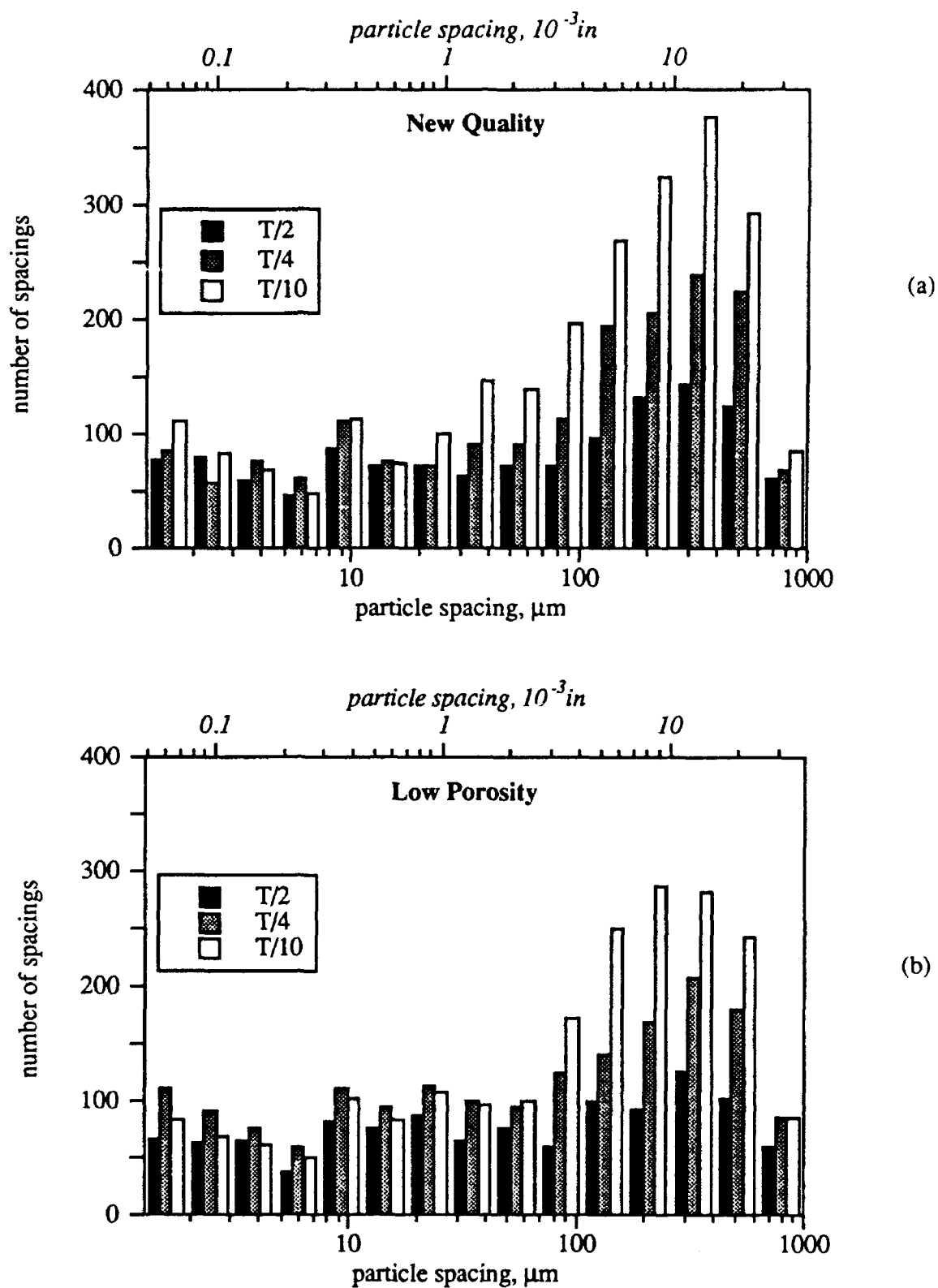
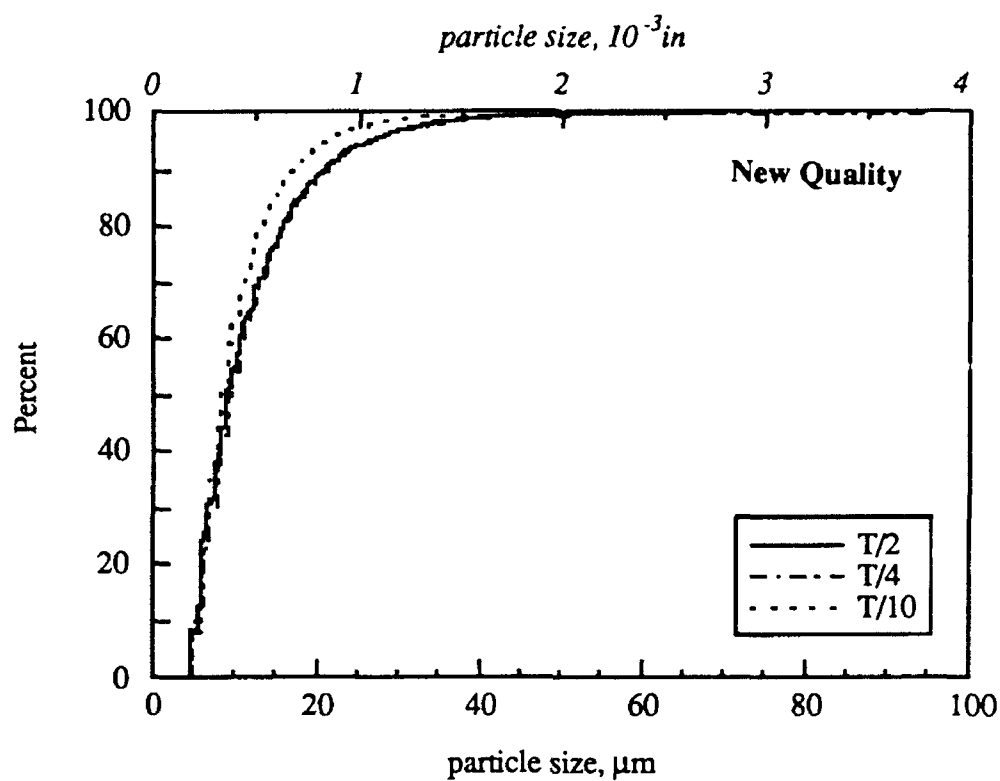
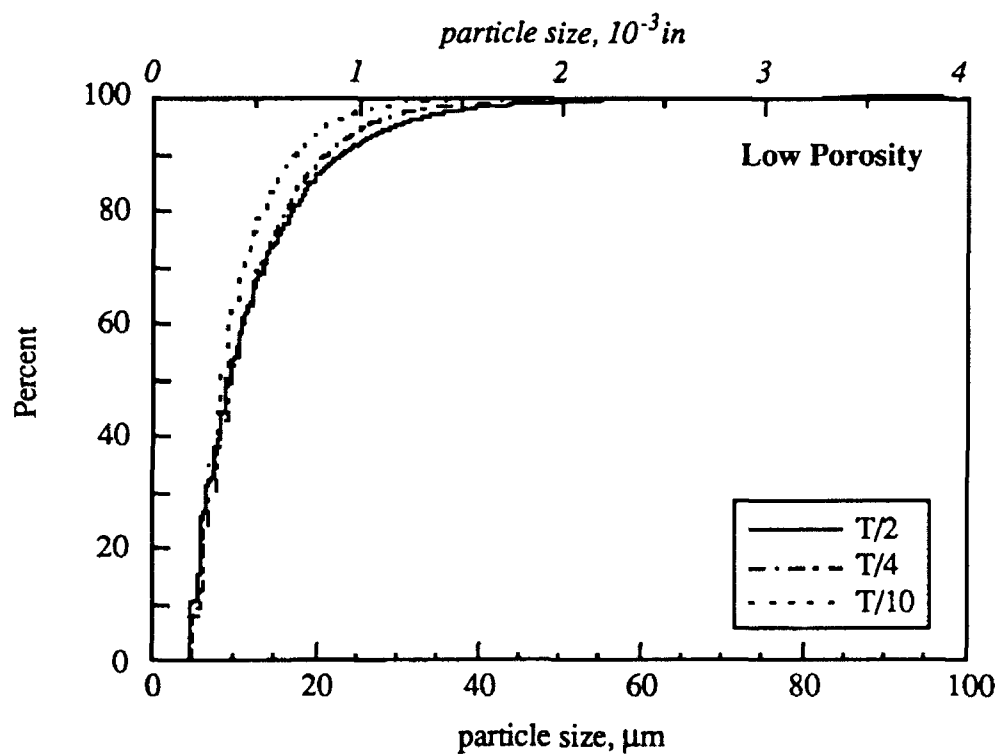


Figure 29. Histograms of inter-particle spacing and inter-stringer spacings on a logarithmic scale for (a) new quality and (b) low porosity materials at different plate locations.

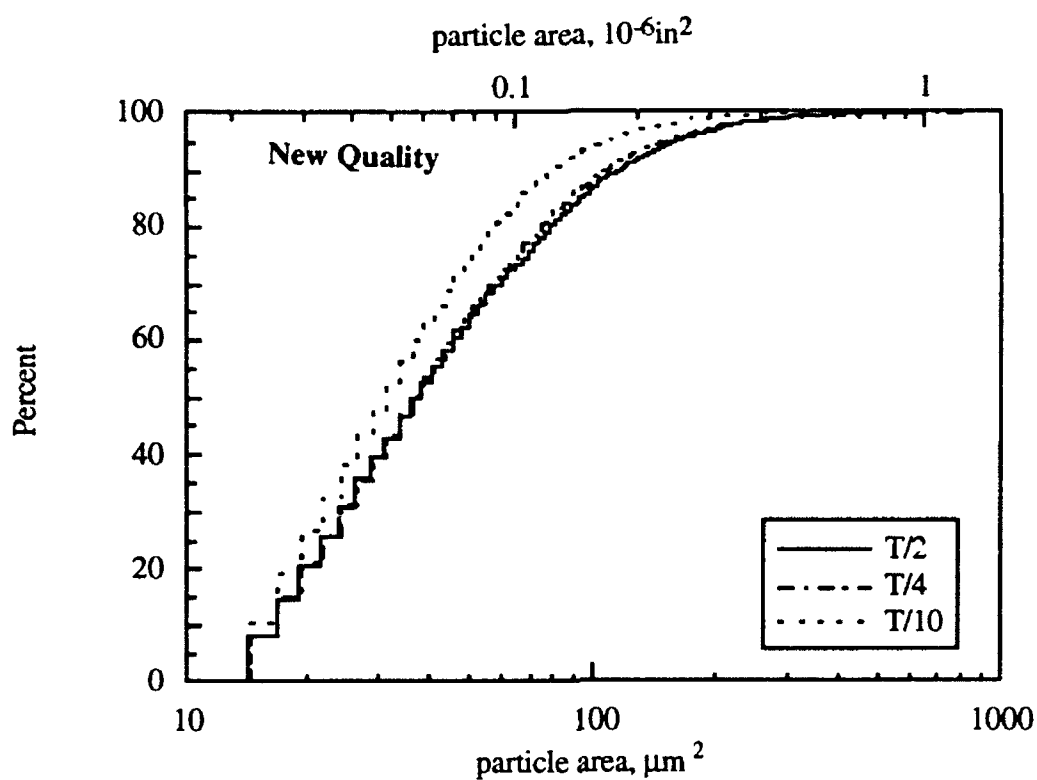


(a)

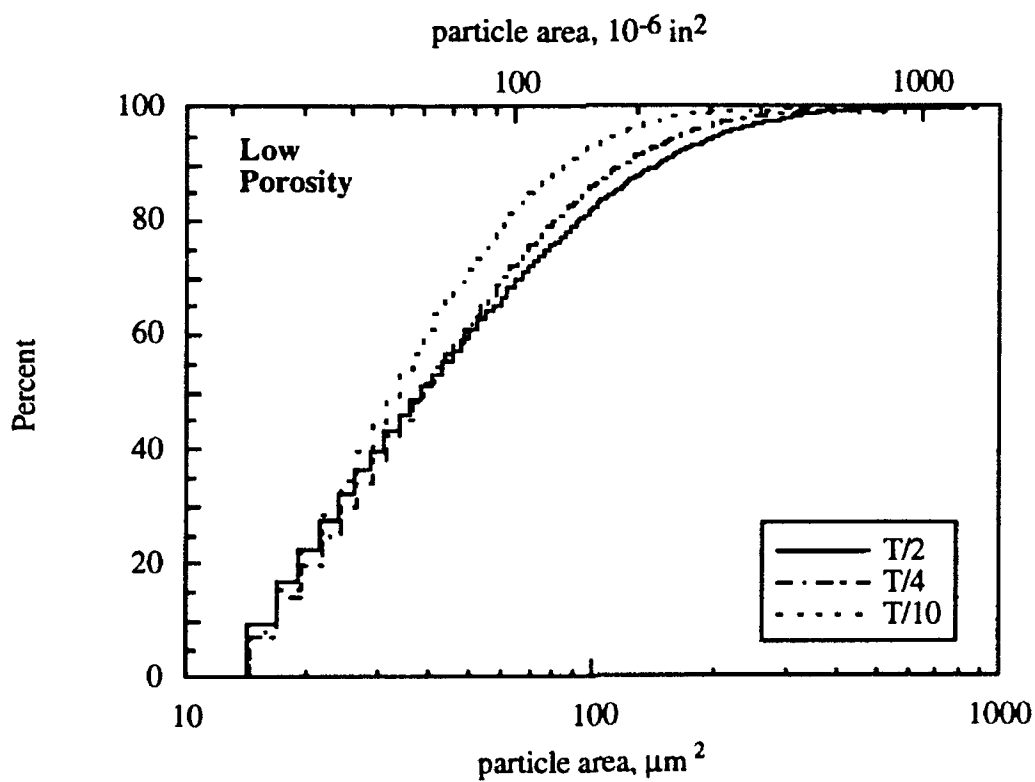


(b)

Figure 30. Graphs of particle size for (a) new quality and (b) low porosity materials at different plate locations.

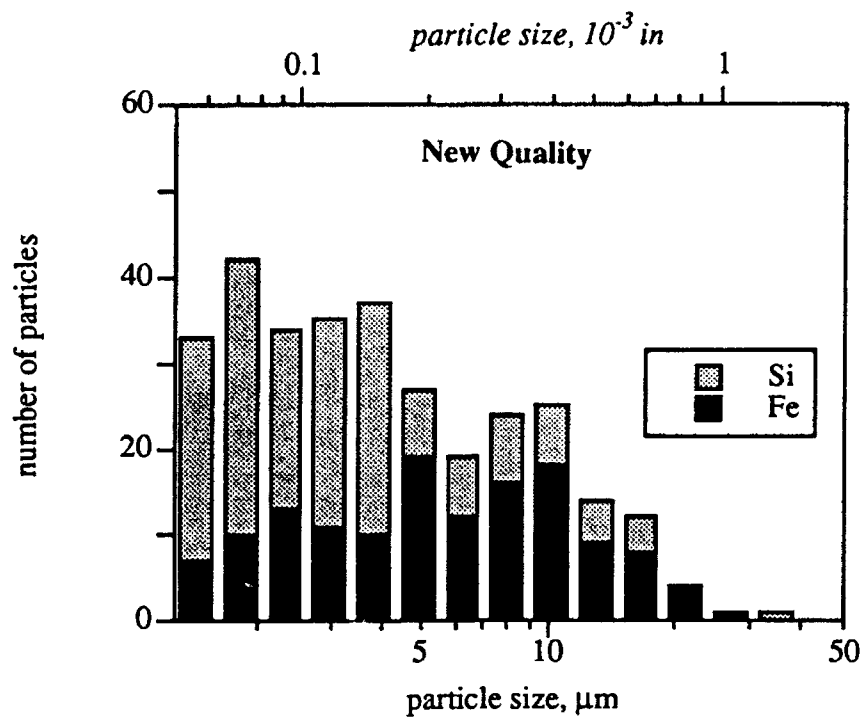


(a)

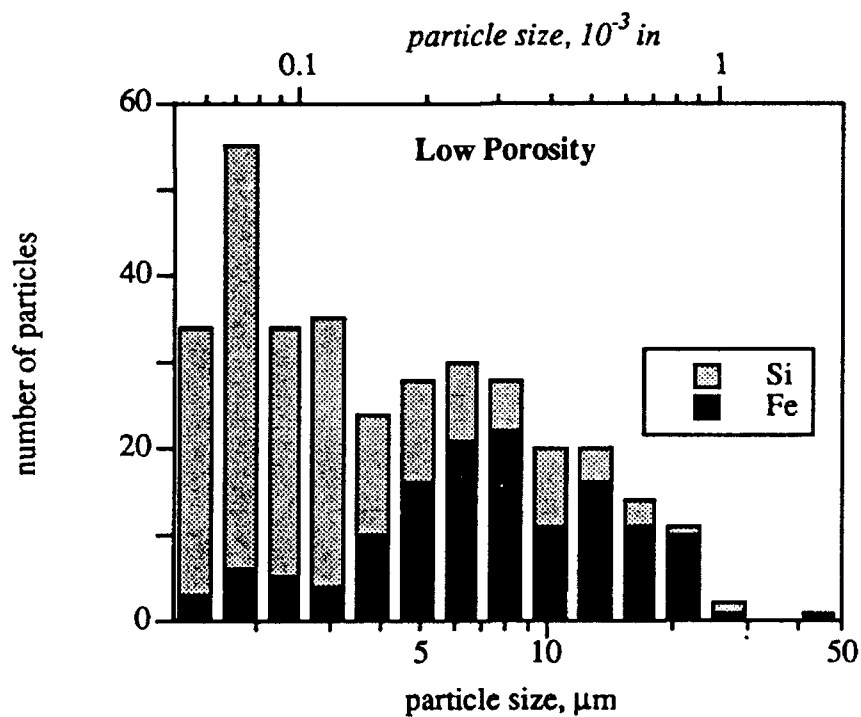


(b)

Figure 31. Graphs of measured particle area for (a) new quality and (b) low porosity materials at different plate locations.



(a)



(b)

Figure 32. Histograms of total, Fe- and Si-containing particle size on a logarithmic scale for (a) new quality and (b) low porosity materials.



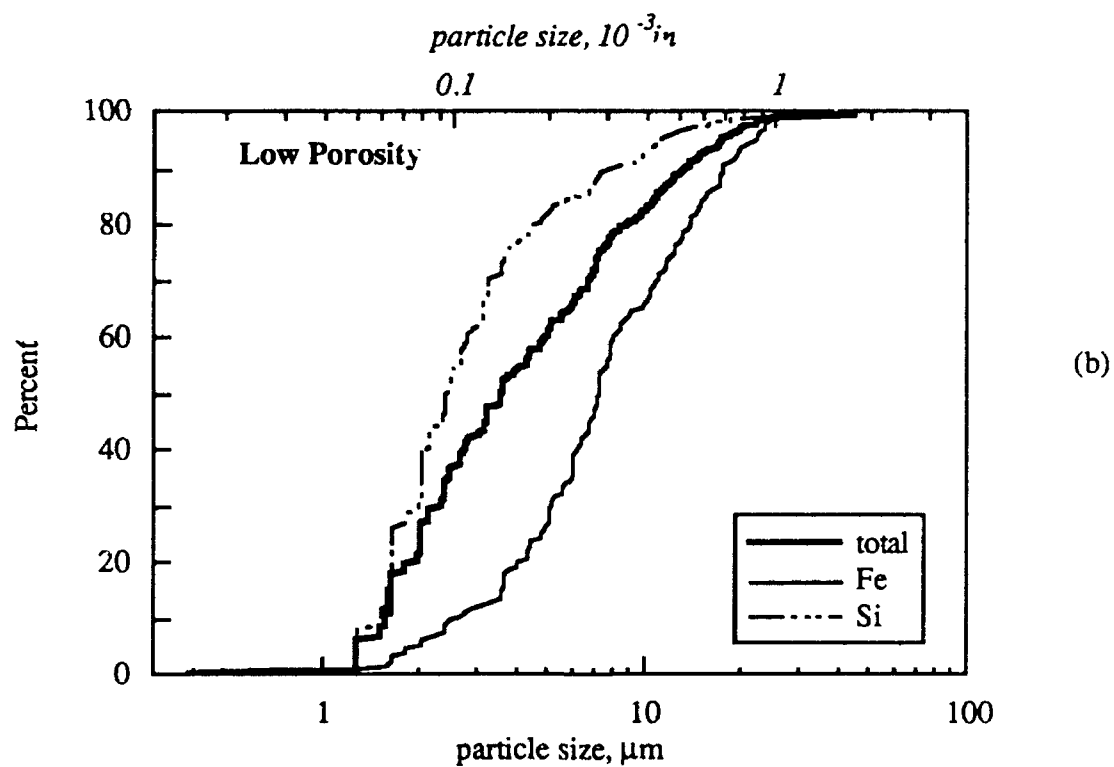
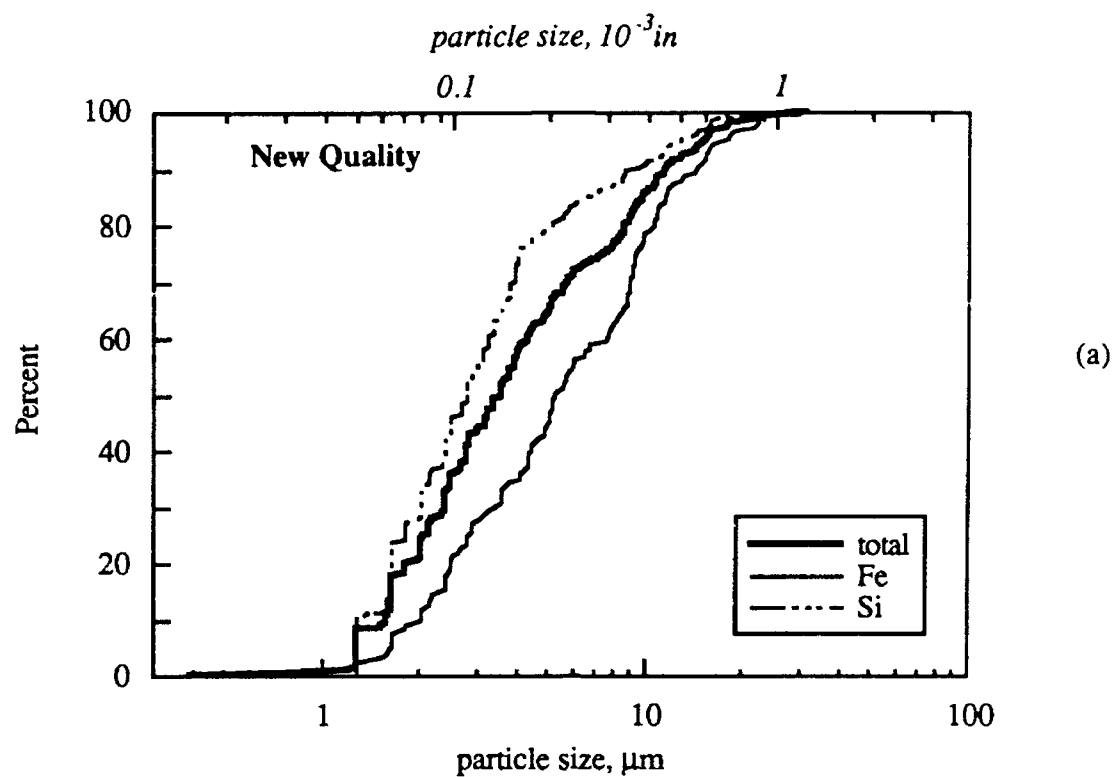
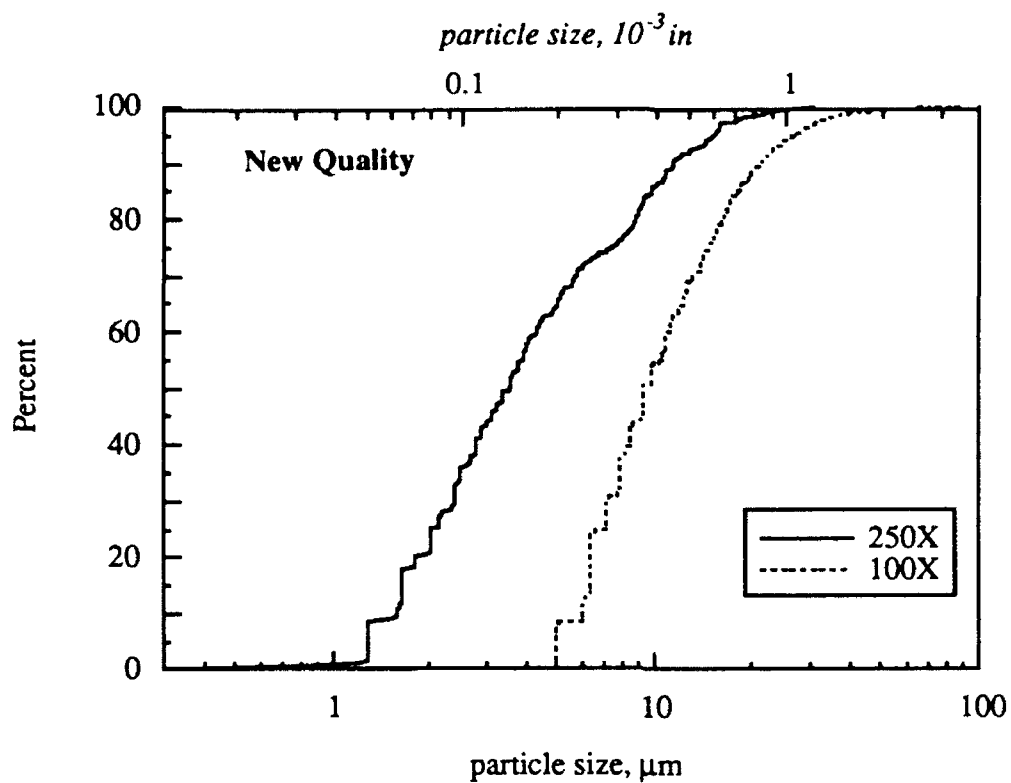
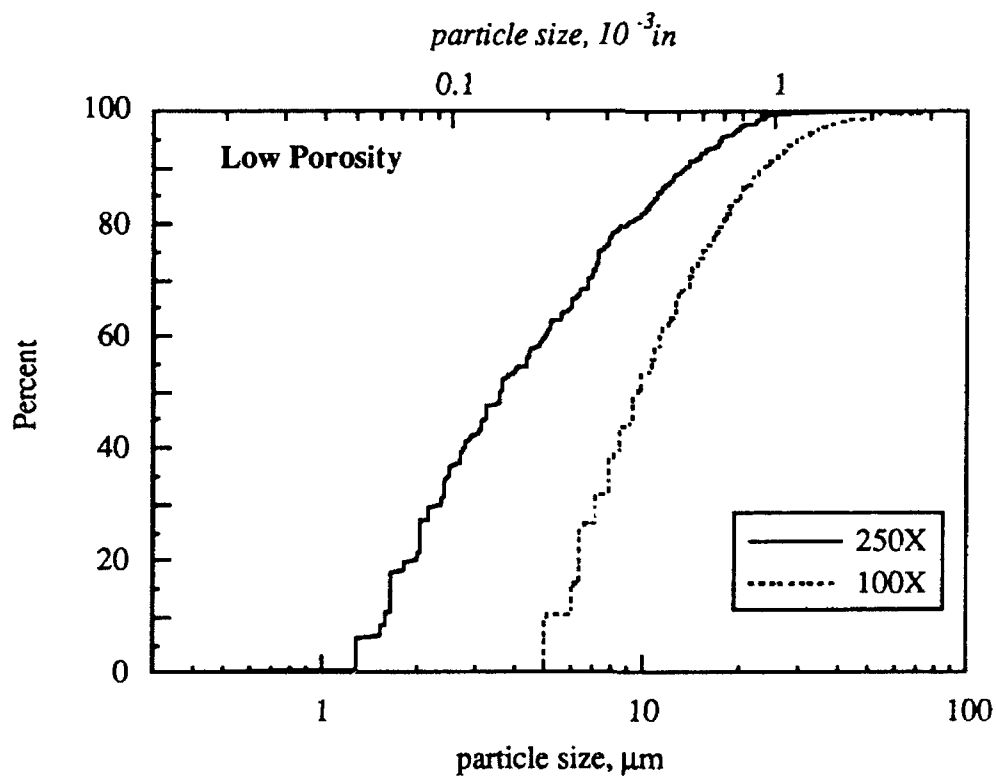


Figure 33. Plots of total, Fe- and Si-containing particle size on a logarithmic scale for (a) new quality and (b) low porosity materials.

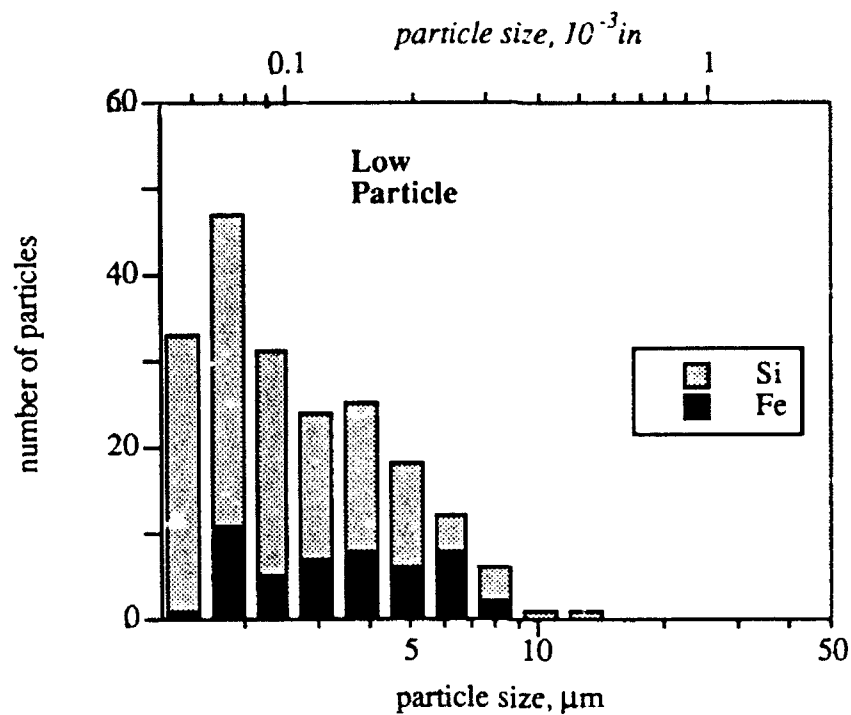


(a)

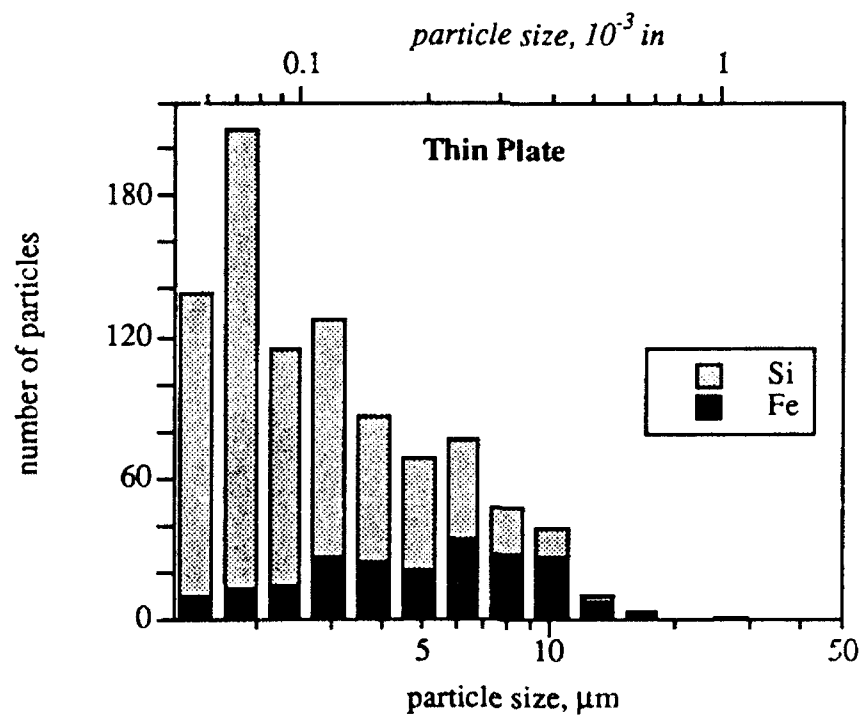


(b)

Figure 34. Plots of particle size at the T/2 location in (a) new quality and (b) low porosity material measured at two different magnifications. Specimen area was  $1.2 \text{ mm}^2$  at 250X and  $31 \text{ mm}^2$  at 100X.

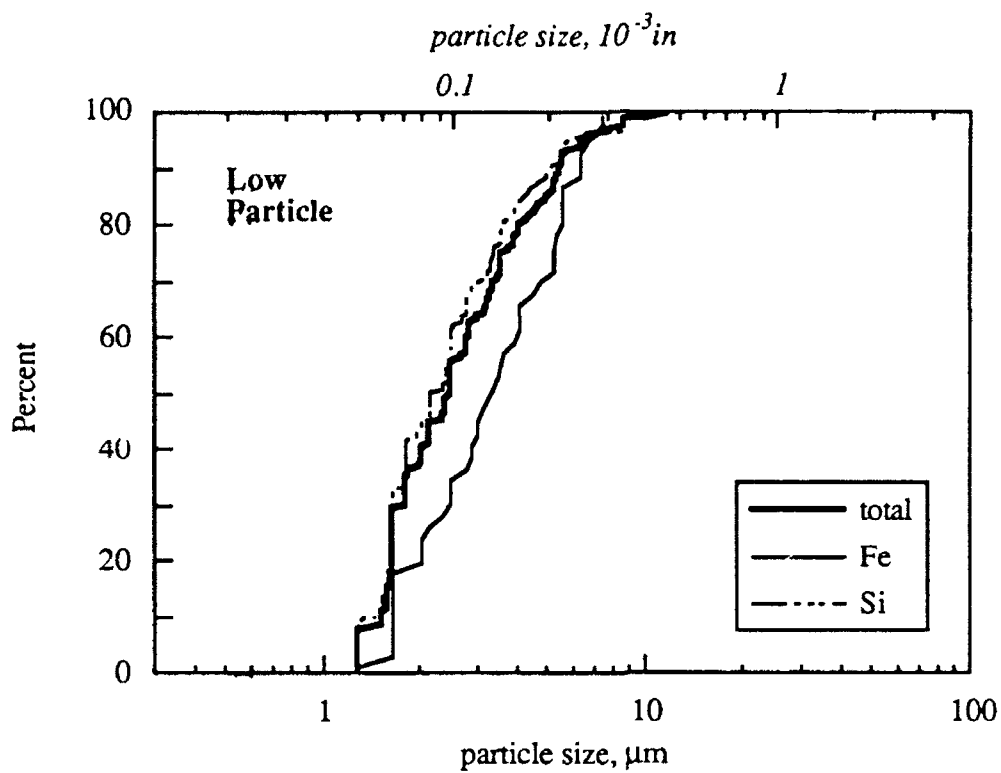


(a)

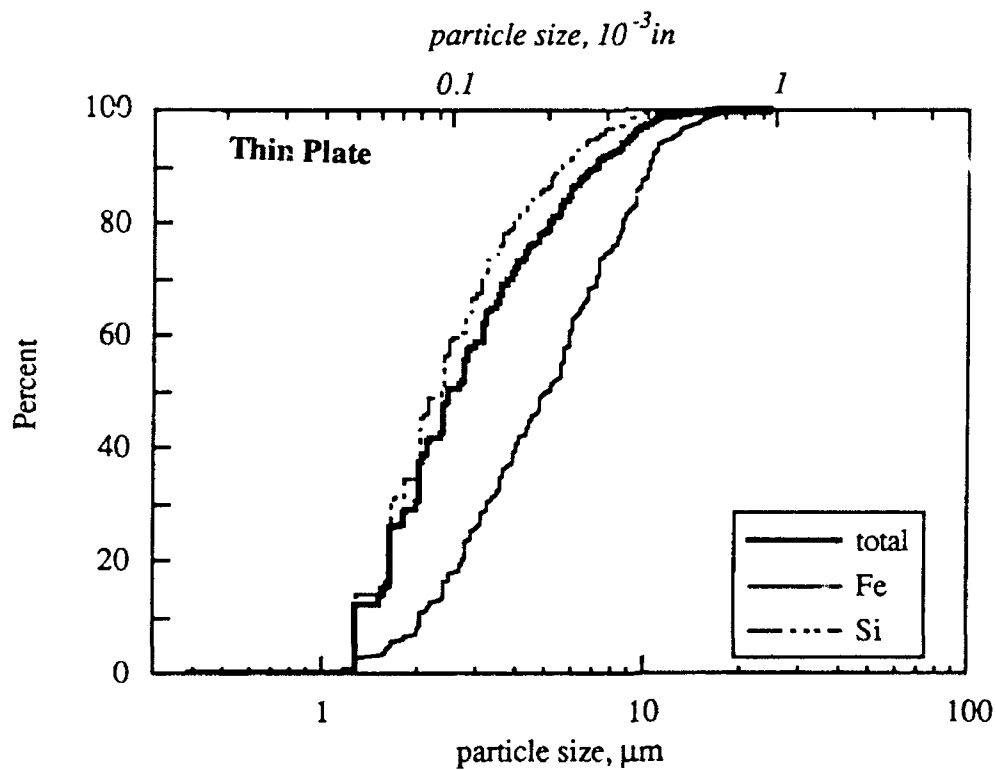


(b)

Figure 35. Histograms of total, Fe- and Si-containing particle size on a logarithmic scale for (a) low particle and (b) thin plate.



(a)



(b)

Figure 36. Plots of total, Fe- and Si-containing particle sizes for (a) low particle and (b) thin plate.

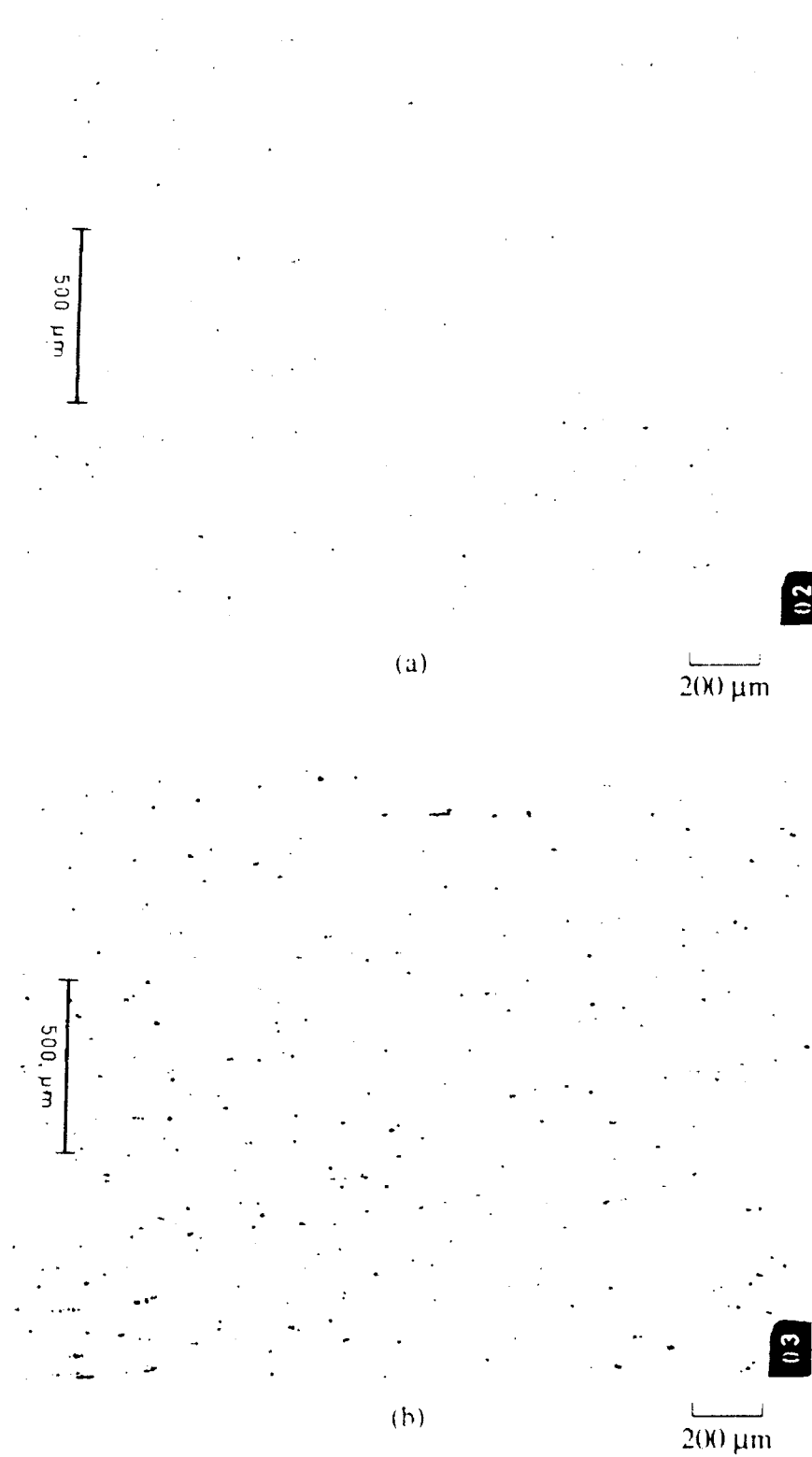


Figure 37. Optical micrographs of constituent particles at the T/4 plate location on the (a) transverse and (b) longitudinal sections.



(a)

200 μm



(b)

200 μm

Figure 38. Optical micrographs of grain structure at the T/4 plate location on the (a) transverse and (b) longitudinal sections.

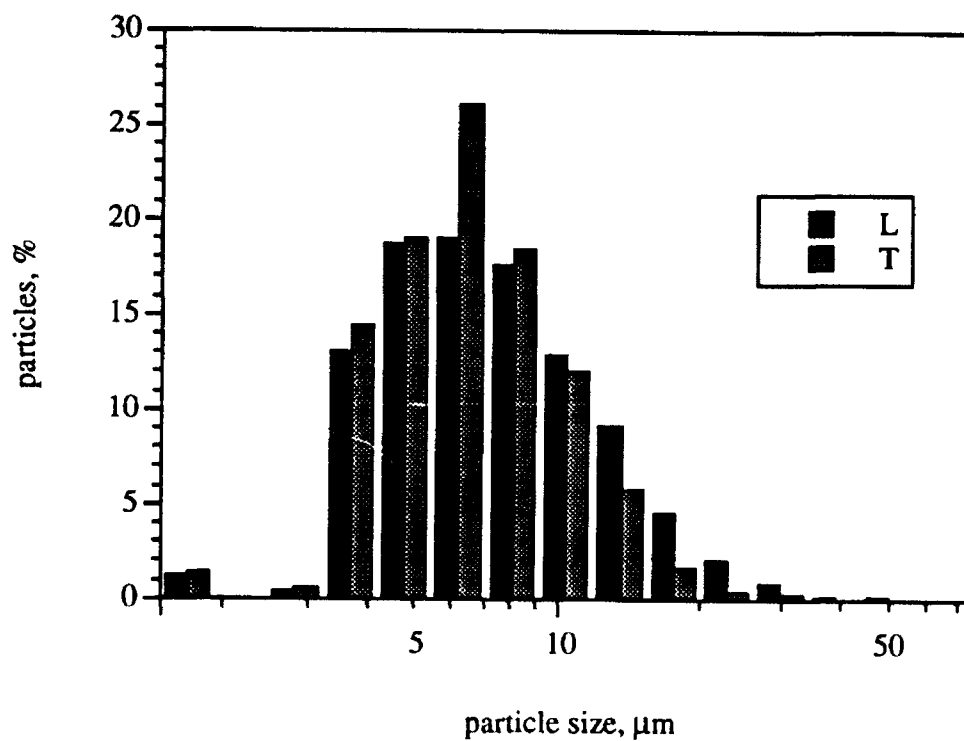
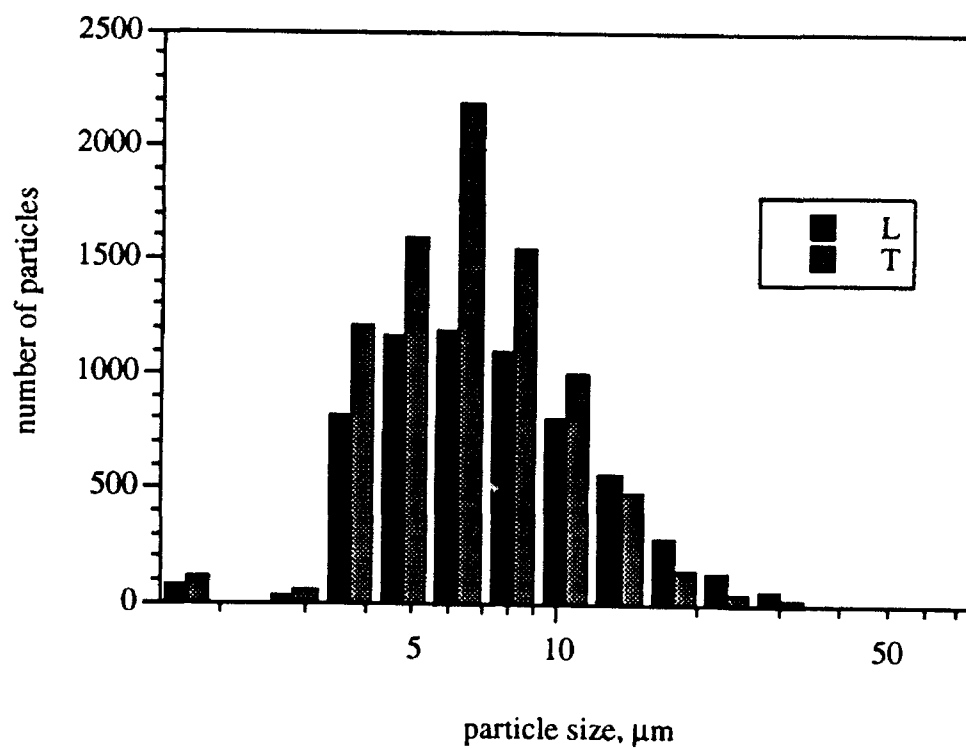


Figure 39. Histograms of particle size on a logarithmic scale for both transverse and longitudinal sections

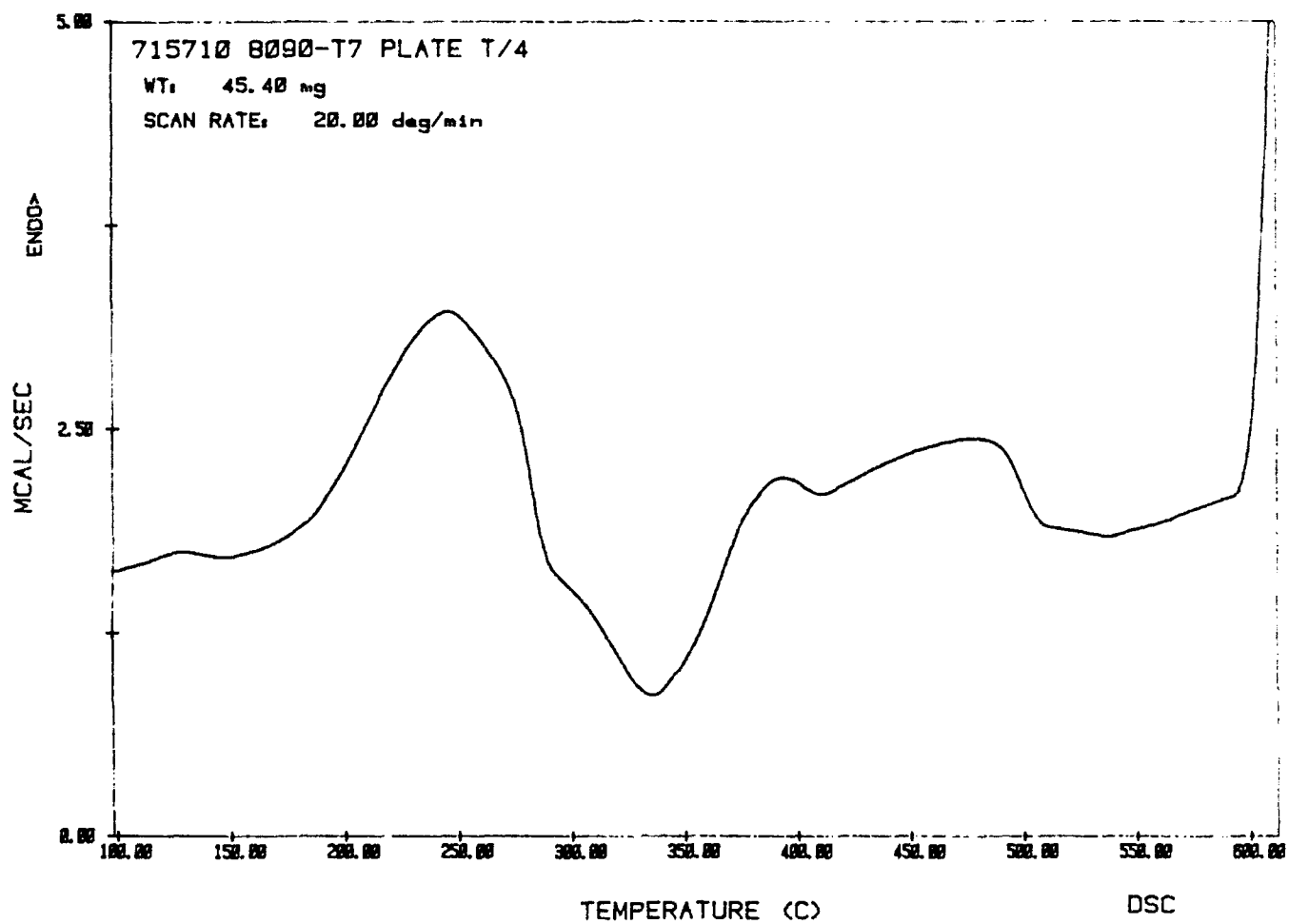
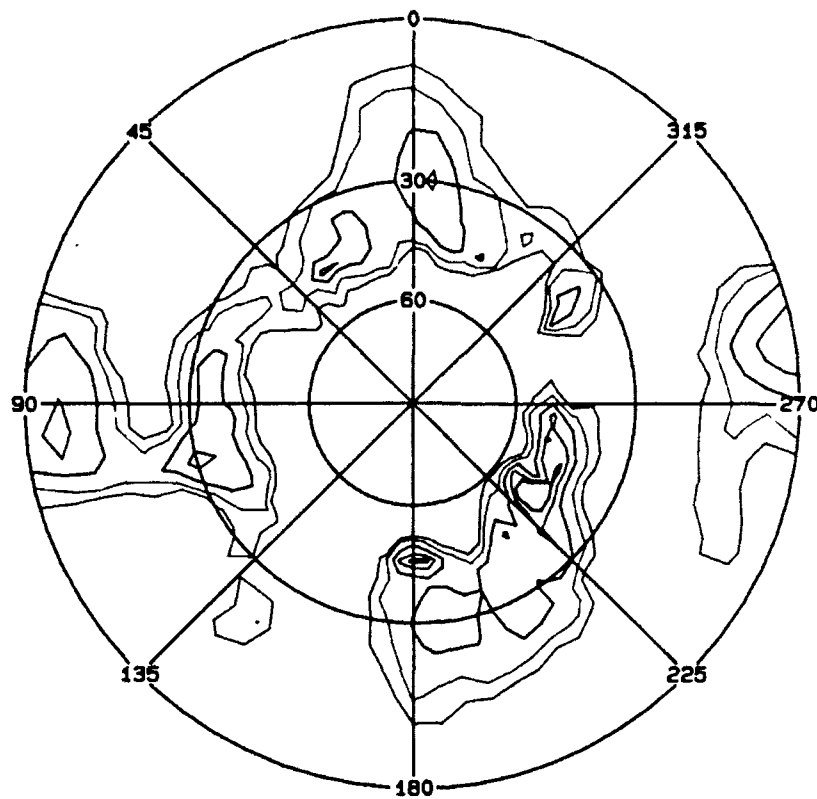


Figure 40. DSC scan on sample taken from the T/4 plate location. Scan rate of 20°C/minute.

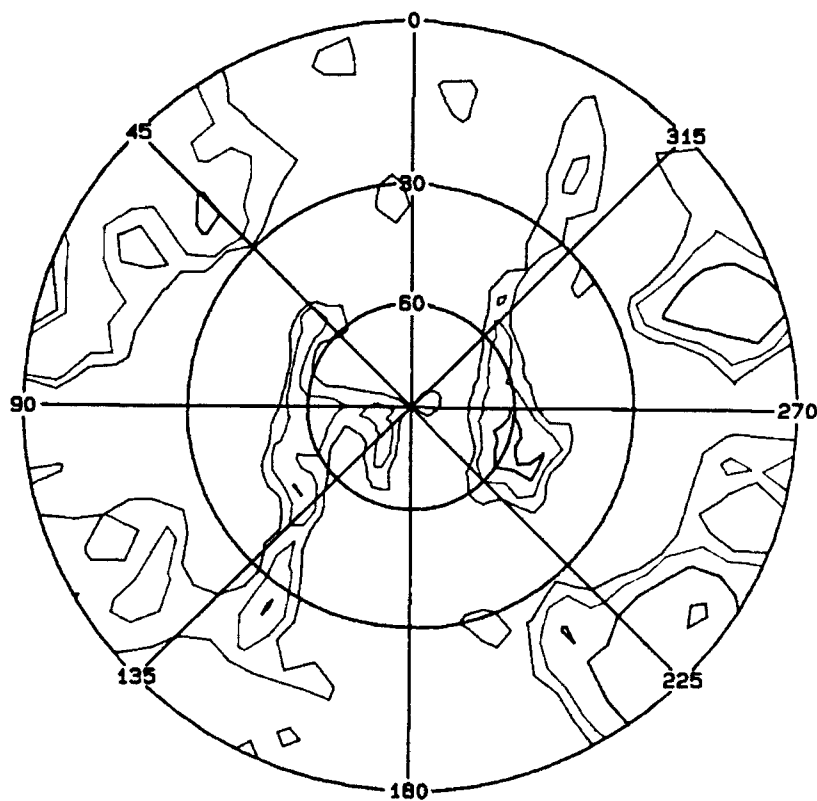




File: SY0: Z06542.PFG  
 Sample: 715710 8090 T  
 1-JUN-92 14: 20: 11  
 H= 2 K= 0 L= 0

Plot Levels:

3.0  
 4.0  
 5.0  
 10.0



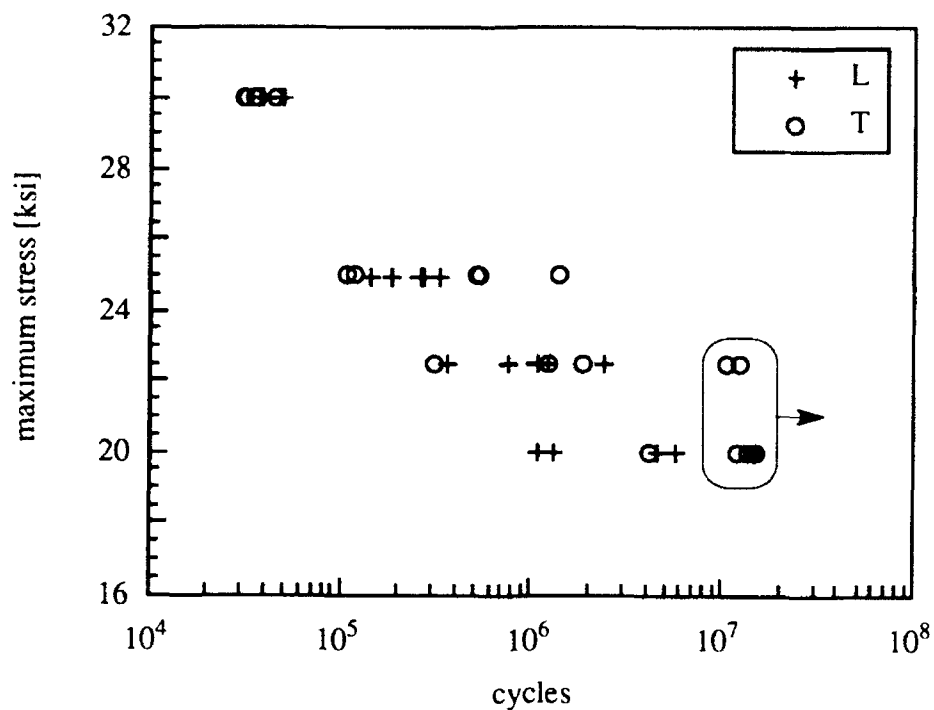
File: SY0: Z06541.PFG  
 Sample: 715710 8090 1  
 1-JUN-92 12: 48: 09  
 H= 1 K= 1 L= 1

Plot Levels:

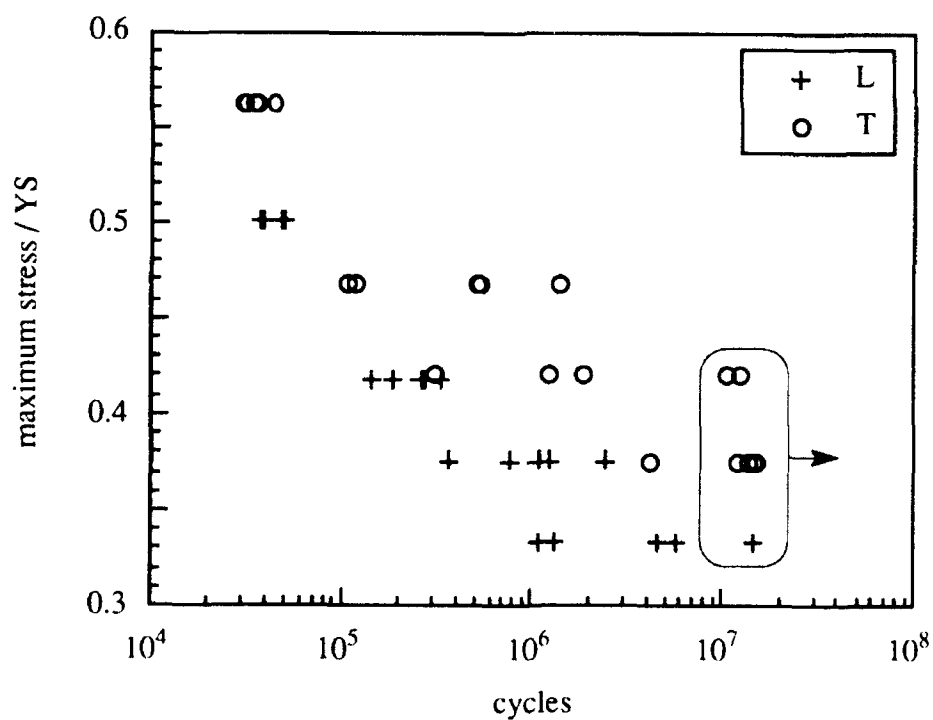
3.0  
 4.0  
 5.0  
 10.0

Figure 41. X-ray pole figures obtained from samples taken from the T/4 plate location.



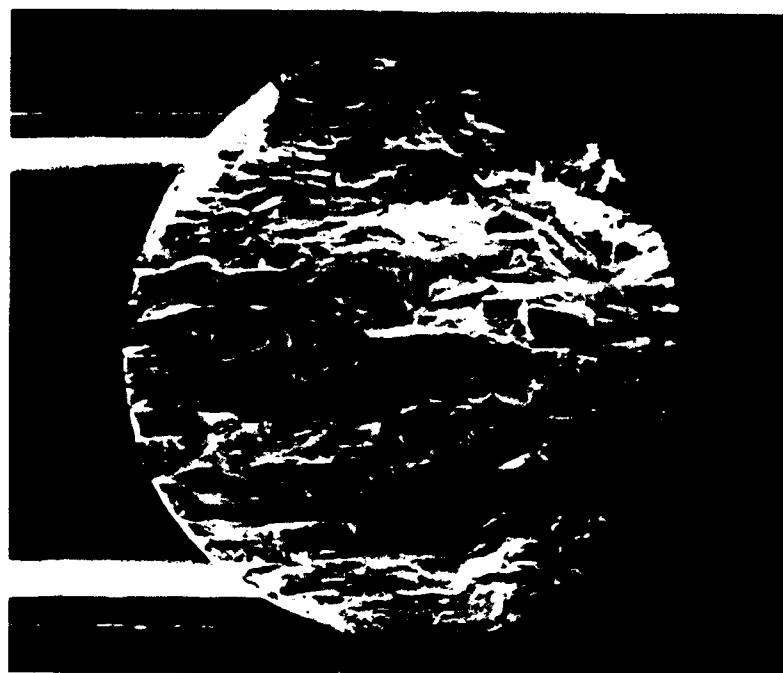


(a)



(b)

Figure 43. Open hole fatigue lifetime data for 8090 alloy plate variant 1 tested at  $R=0.1$ , 30 Hz, in lab air. (a) S/N curves and (b) data normalized by the yield strength.



(a)

1 mm



(b)

1 mm

Figure 44. SEM fractographs of the overall failure surface for (a) L orientation and (b) LT orientation smooth specimens tested at a maximum stress of 35 ksi.



(a)

1 mm



(b)

500 μm



(c)

200 μm



(d)

50 μm

Figure 45. SEM fractographs of L orientation (maximum stress=30 ksi, N=2,273,812 cycles).



(a) 1 mm



(b) 500 μm

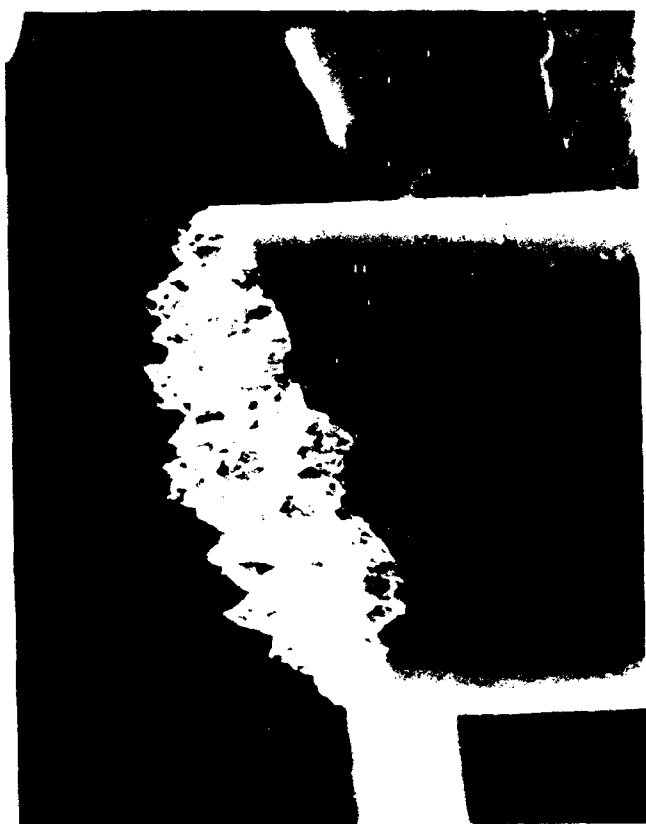


(c) 200 μm



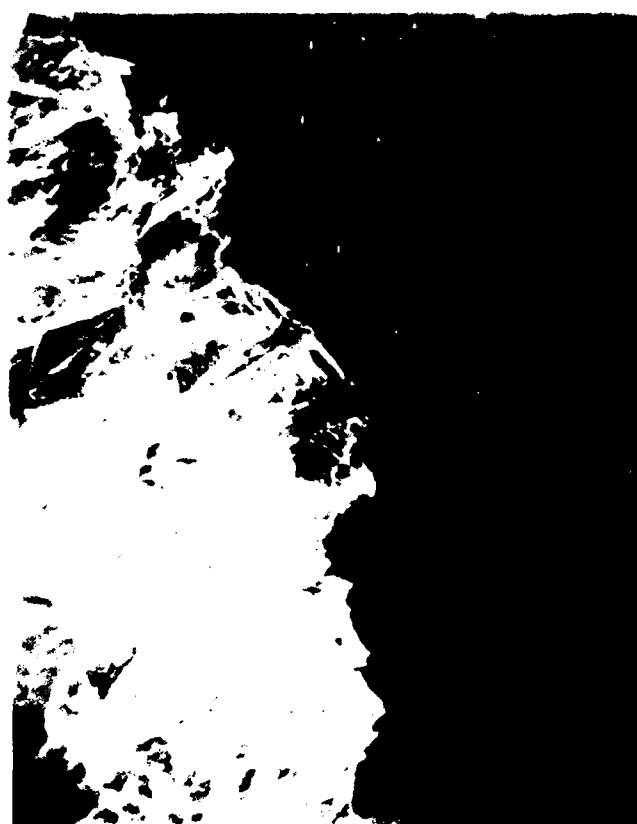
(d) 50 μm

Figure 46. SEM fractographs of L orientation (maximum stress=45 ksi, N=87,854 cycles).



(a)

1 mm



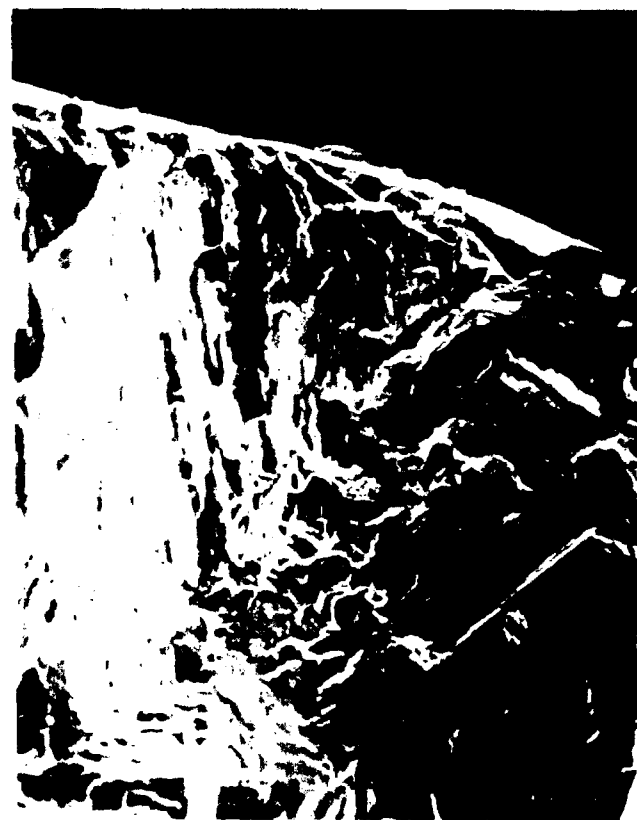
(b)

500  $\mu\text{m}$



(c)

200  $\mu\text{m}$



(d)

50  $\mu\text{m}$

Figure 47 SEM fractographs of T1 orientation (to maximum stress = 50 ksi,  $N_f = 36,300$  cycles).



(a)

1 mm



(b)

500  $\mu\text{m}$



(c)

200  $\mu\text{m}$

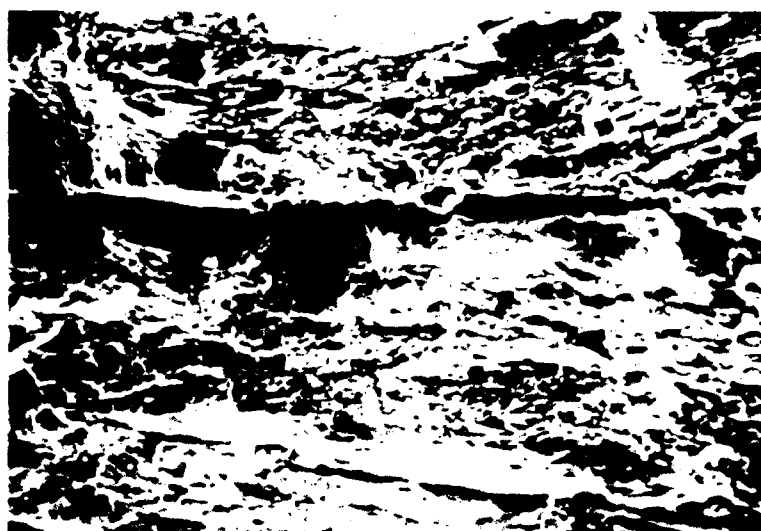


(d)

50  $\mu\text{m}$

Figure 48. SEM fractographs of LT orientation (maximum stress=45 ksi, N=44,539 cycles).





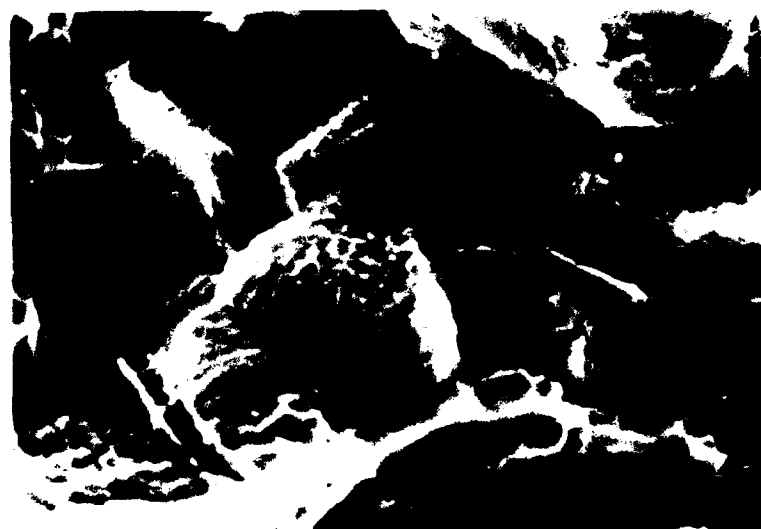
(a)

50 μm



(b)

10 μm



(c)

2 μm

Figure 49. SEM fractographs of tensile overload regime in an L-orientation smooth specimen.

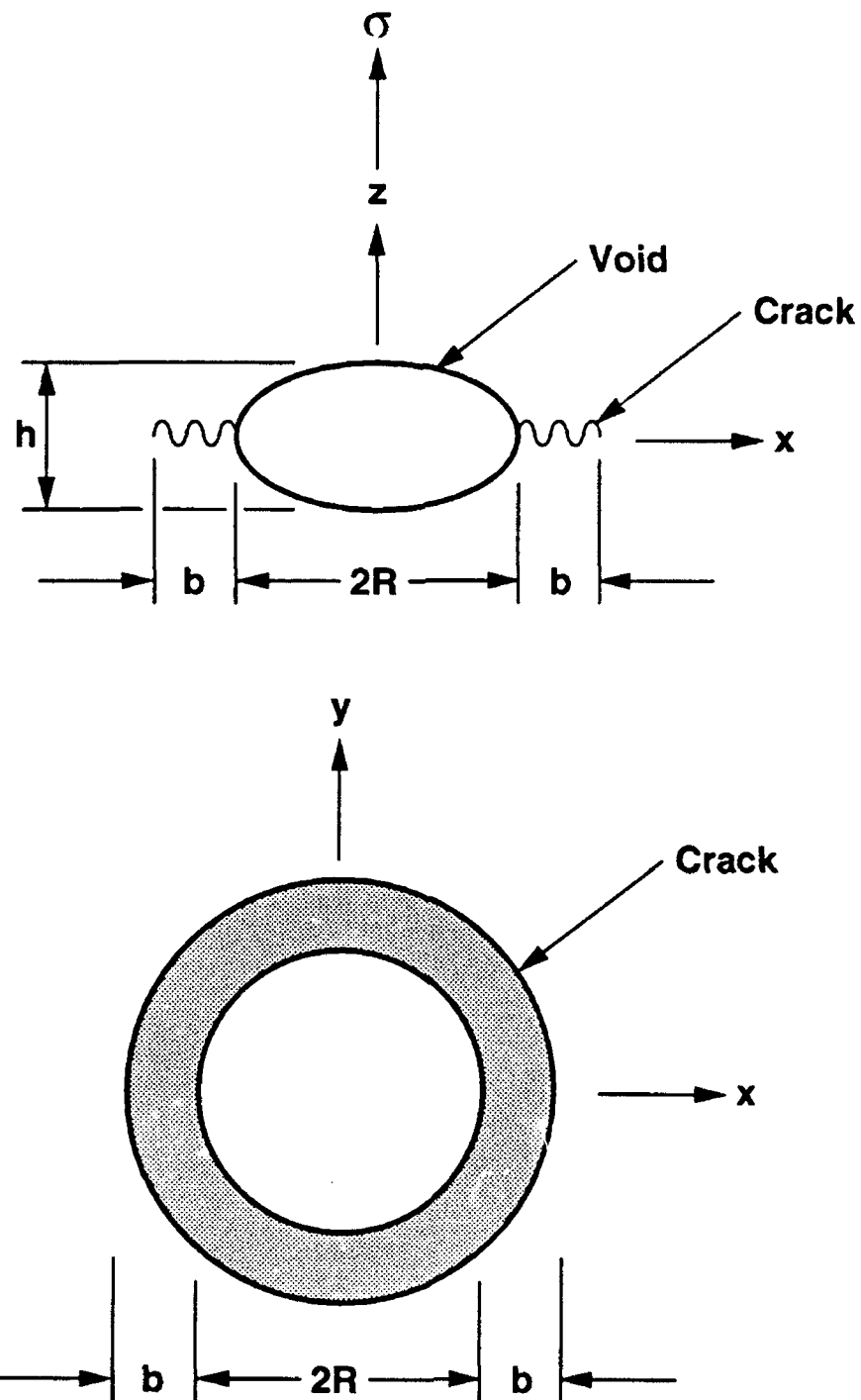
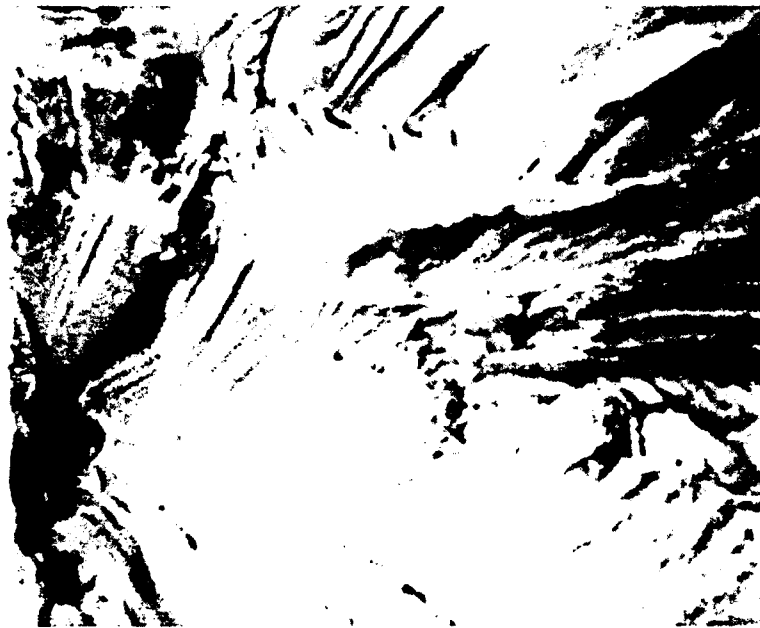
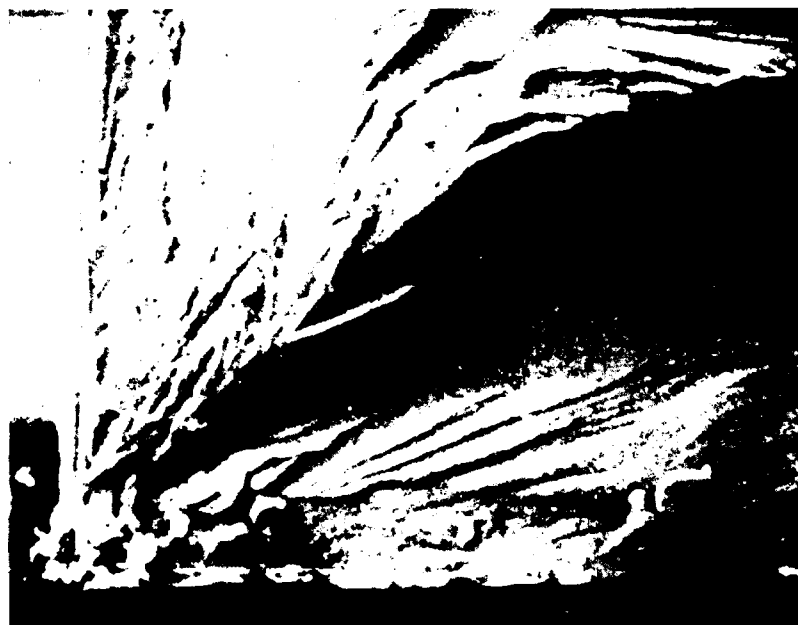


Figure 50. Schematic representation of cracked, ellipsoidal void analyzed by Trantina and Barishpolsky [27].



**a) Interior porosity of 710  $\mu\text{m}^2$ .  
Actual life: 80,700 cycles,  
Predicted life: 80,000 cycles.**



**b) Corner particle of 324  $\mu\text{m}^2$ .  
Actual life: 79,500 cycles.  
Predicted life: 74,500 cycles.**

Figure 51 Comparison of the calculated and actual lifetimes for open hole fatigue failures in 7050 plate for initiation from (a) microporosity in the bore of the hole and (b) constituent particle at the corner of the hole

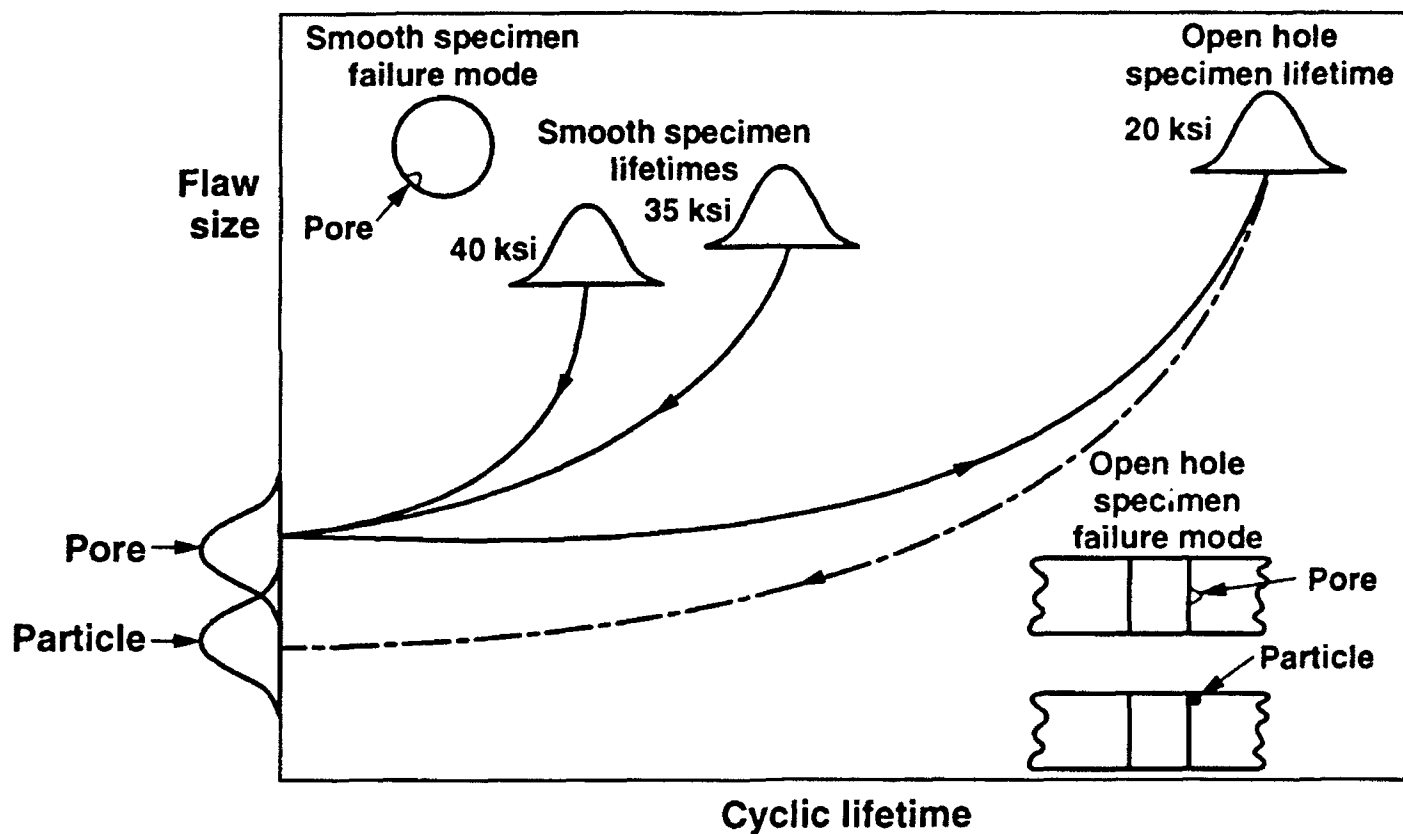


Figure 52. Schematic representation of the calculation of open hole specimen fatigue lifetime in 7050 plate from initial distributions of micropores located in the hole bore and particles located at the hole corner.

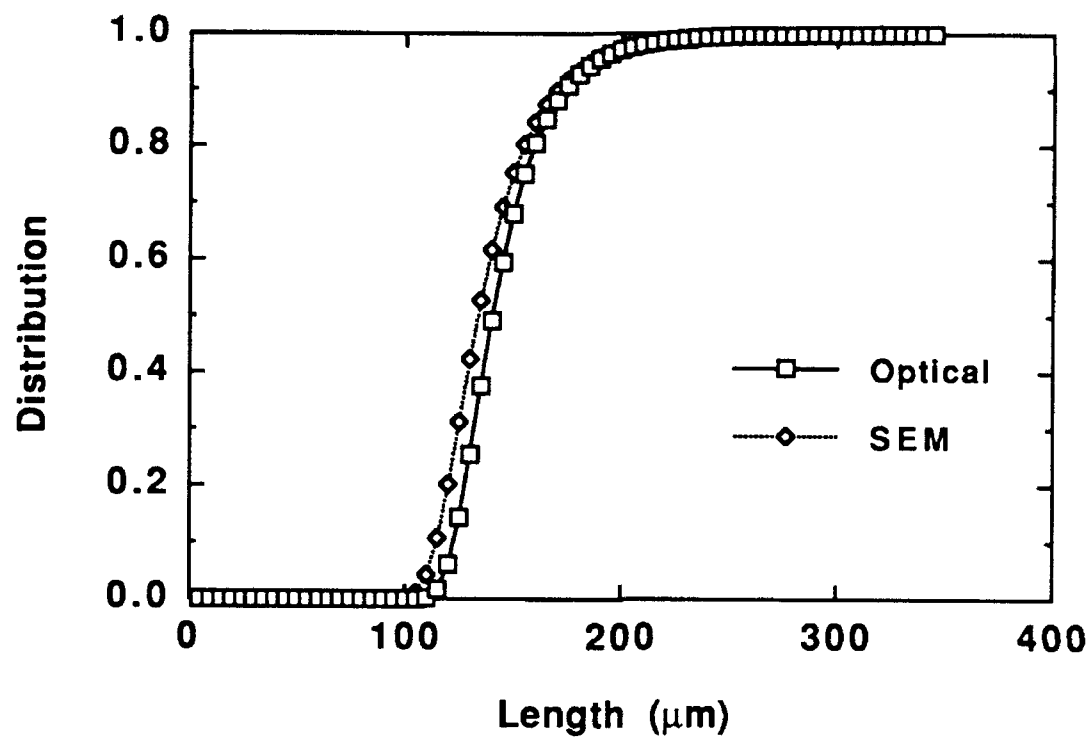


Figure 53. Calculated extreme value distributions of constituent particles based on random plane measurements of particle distributions made using optical and scanning electron microscopes.

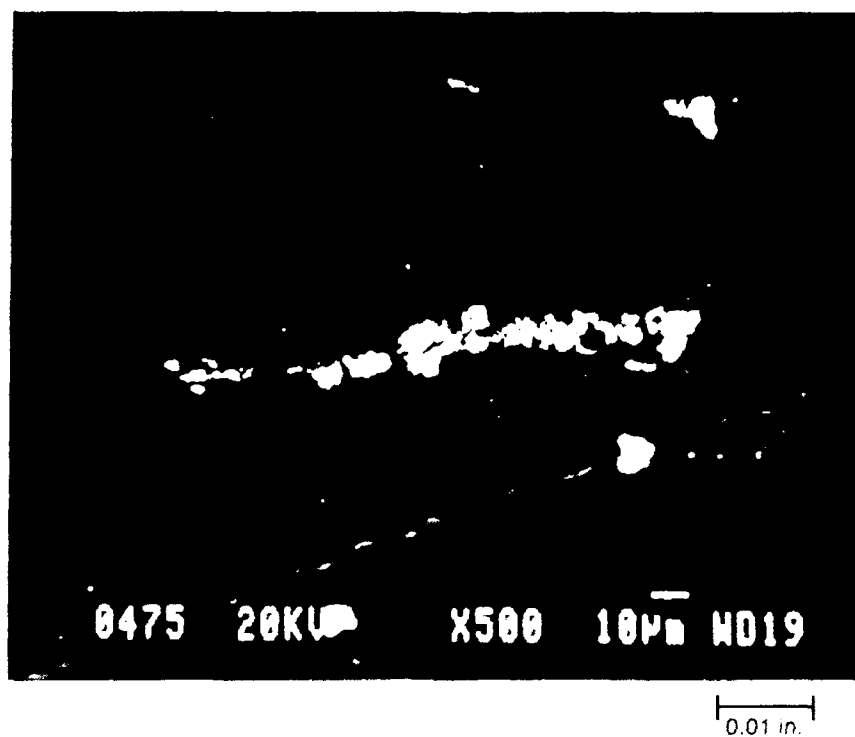


Figure 54. Cluster of constituent particles in alloy 7050 thick plate.

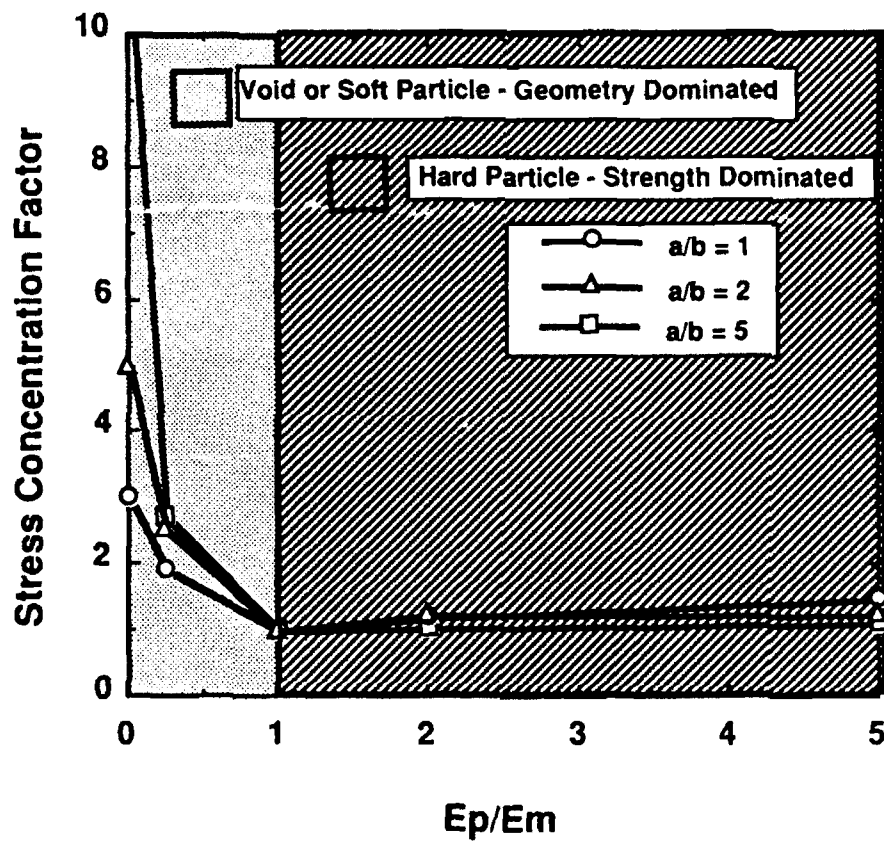


Figure 55. Calculated stress concentration factor for ellipsoid region of high particle volume fraction versus the ratio of the modulus of the ellipsoid to the modulus of the matrix.

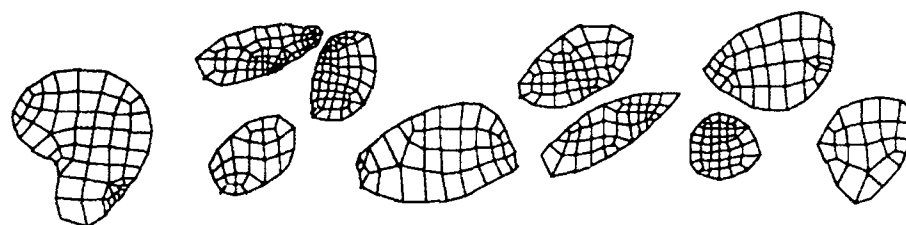
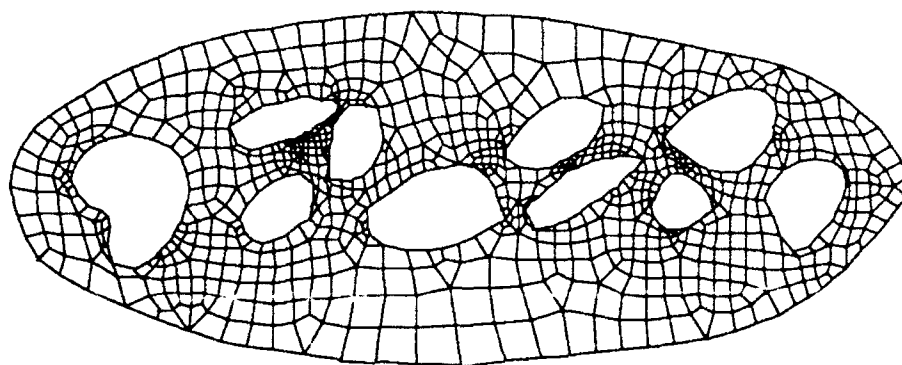


Figure 56. Finite element mesh of matrix material and particles within an ellipsoid region of high particle volume fraction.



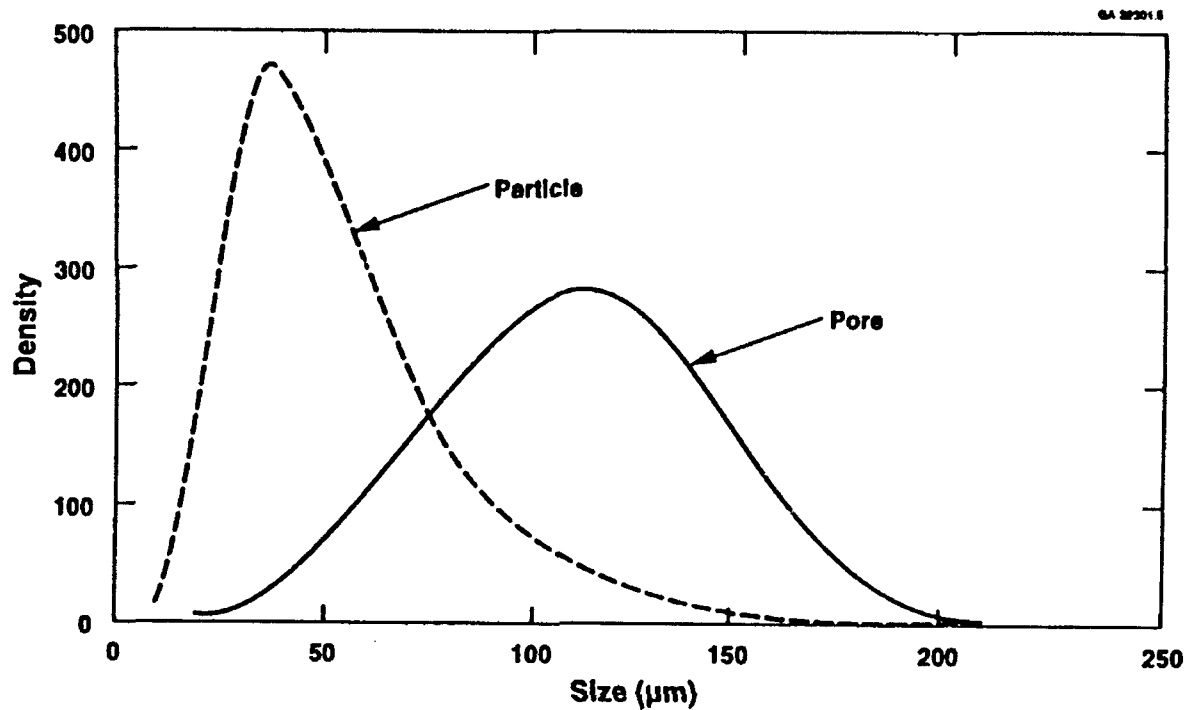


Figure 57. Calculated size distribution of particles located at hole corner and size distribution of micropores located within the hole bore of open hole specimens which result in equivalent fatigue life distributions.

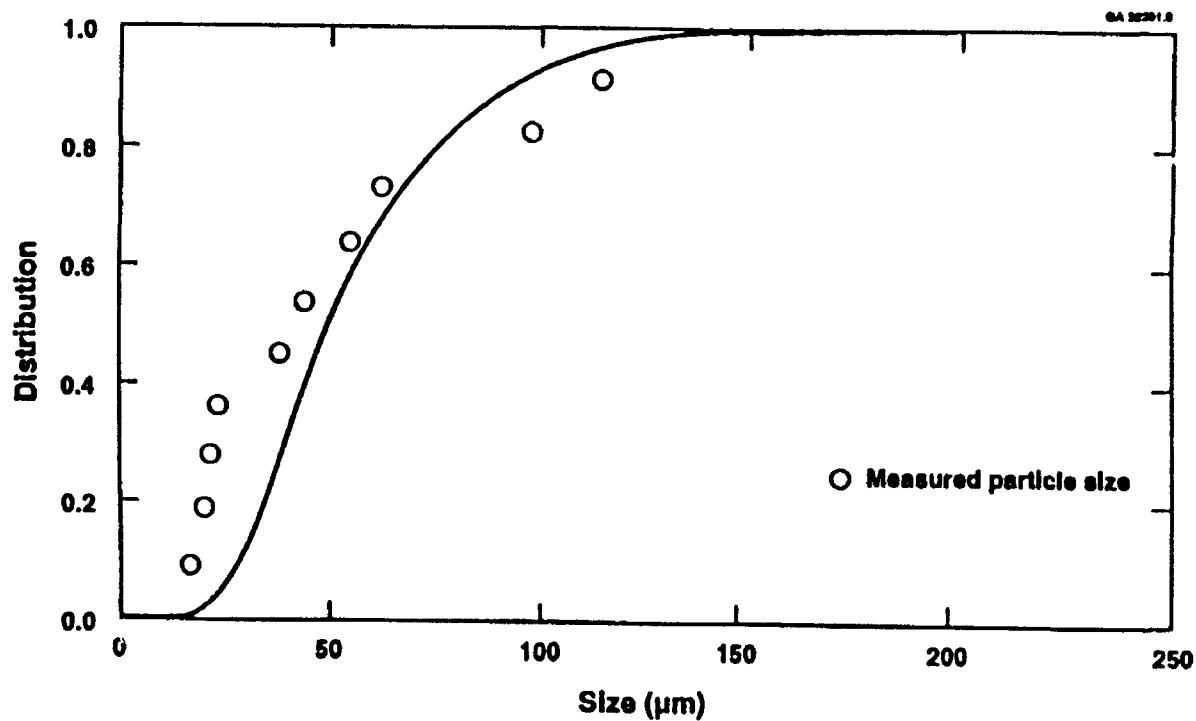


Figure 58. Comparison of the calculated size distribution of particles and the actual size distribution of particles located at hole corner in low porosity 7050 plate open hole fatigue tests.

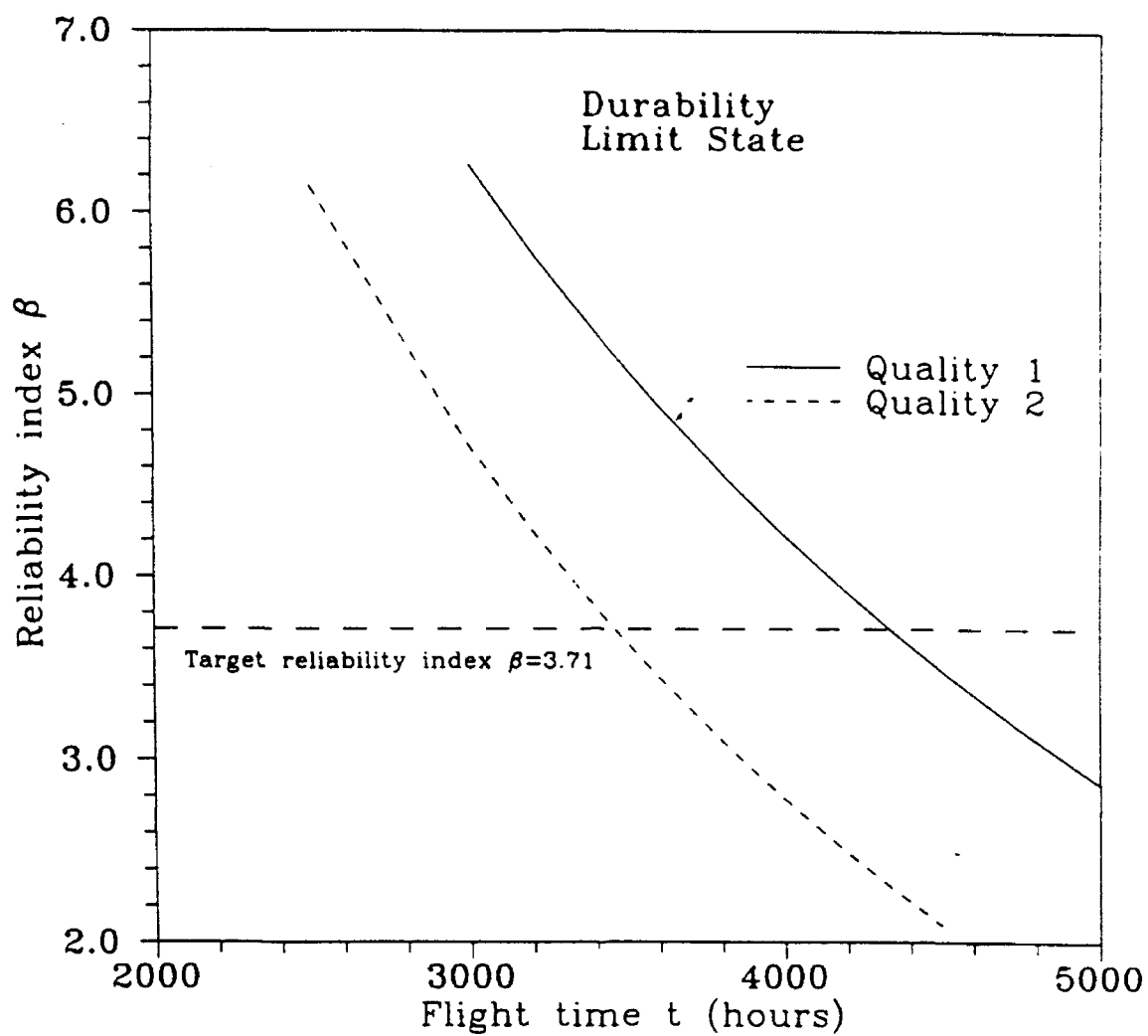


Figure 59. Calculated inspection intervals for old and new quality 7050 plate based on initial micropore distributions and probabilistic evaluation of reliability.